Diss. ETH Nr. 12629

Direct Gluon Density Determination in Tagged Charm-Photoproduction at HERA

A dissertation submitted to the

Swiss Federal Institute of Technology Zurich

for the degree of

Doctor of Natural Sciences

presented by

Hubert Niggli

dipl. phys. ETH

born June 30th, 1968

citizen of Horw/LU

accepted on the recommendation of

Prof. Dr. Ralph A. Eichler, examiner and

Prof. Dr. Zoltan Kunszt, co-examiner

March 1998

Abstract

Charm production at HERA is dominated by events with a very small virtuality of the exchanged photon (photoproduction). In lowest order it proceeds via photon-gluon fusion and is therefore directly sensitive to the gluon density in the proton.

In this thesis single inclusive $D^{*\pm}$ spectra (in η and p_t) are measured in photoproduction at $\overline{W_{\gamma p}} = 88\ GeV$ and $\overline{W_{\gamma p}} = 194\ GeV$ and the energy flow in these charm events is analysed. The single inclusive spectra are found to be well described by next to leading order calculations in perturbative quantum chromodynamics. Good agreement is also found comparing the energy flow in data with monte carlo simulations. Both measurements show that the charm photoproduction mechanism in the investigated kinematical range is theoretically well understood and suited to probe the gluon density in the proton. A direct determination of the gluon density in the proton $f_g^{(p)}(x_g, \mu_F^2)$ in NLO QCD in the accessible range $0.001 \leq x_g \leq 0.04$ and $\mu_F^2 = 50\ GeV^2$ is therefore performed. The result confirms previous determinations from scaling violations of the proton structure function F_2 and from (2+1)–jet production rates in deep inelastic scattering at HERA.

$D^{*\pm}$-mesons are tagged via explicit reconstruction of the decay channel $D^* \to D^0\pi_s$, $D^0 \to K\pi$. Data recorded with the H1 detector in the years 1994, 1995 and 1996 is analysed, corresponding to an integrated luminosity of $10.7\ pb^{-1}$.

Zusammenfassung

Die Produktion von Teilchen mit Charm am Elektron-Proton Speicherring HERA ist dominiert durch Ereignisse mit kleinster Virtualität des ausgetauschten Photons (Photoproduktion). Der Produktionsprozess in tiefster Ordnung Störungsrechnung ist die Fusion des Photons mit einem Gluon aus dem Proton weshalb die Rate direkt sensitiv auf den Gluongehalt des Protons ist.

Eine Messung von einfach differentiellen D^*-Spektren in p_t und η bei einer Photon-Proton Schwerpunktsenergie von $\overline{W_{\gamma p}} = 88\ GeV$ und $\overline{W_{\gamma p}} = 194\ GeV$ wird zunächst mit Quantenchromodynamik-Rechnungen in zweiter Ordnung Störungstheorie verglichen. Es zeigt sich eine gute Übereinstimmung der Theorie mit dem Experiment. Des weiteren wird eine Messung des Energieflusses in solchen Charm-Ereignissen präsentiert und mit Monte Carlo Simulationen verglichen. Auch hier werden die Daten gut vom Modell beschrieben. Insgesamt ergibt sich, dass die Photoproduktion von Mesonen mit Charm im untersuchten kinematischen Bereich theoretisch gut verstanden und somit bestens geeignet ist, die Gluondichte im Proton zu bestimmen. Eine solche direkte Messung von $f_g^{(p)}(x_g, \mu_F^2)$ in zweiter Ordnung Störungsrechnung (NLO) wurde durchgeführt und ergab im zugänglichen kinematischen Bereich $0.001 \leq x_g \leq 0.04$ und $\mu_F^2 = 50\ GeV^2$ ein Resultat das bisherige Messungen aus Skalenverletzung der Strukturfunktion F_2 und (2+1)–Jet Raten in tief-inelastischer Elektron-Proton Streuung bei HERA bestätigt. Die vorgestellte Methode ist gleichzeitig direkt und benutzt in NLO berechnete partonische Wirkungsquerschnitte, was neu ist. $D^{*\pm}$ Mesonen werden durch explizite Rekonstruktion des Zerfallskanals $D^* \rightarrow D^0\pi_s$, $D^0 \rightarrow K\pi$ nachgewiesen. Die analysierten Daten entsprechen einer integrierten Luminosität von $10.7\ pb^{-1}$ und wurden mit dem H1 Detektor in den Jahren 1994 bis 1996 gesammelt.

Contents

Chapter 1

Charm Photoproduction at HERA and the Gluon Density

1.1 Introduction

Both the total and the charm production cross sections at the positron-proton collider HERA (chapter 2) are dominated by events where the positron scattering angle is small and the exchanged photon is nearly on the light cone (*photoproduction*). The small virtuality allows the photon to oscillate in quark-pairs or even in quasi-bound meson states and therefore to behave as a hadron in the interaction with the proton. Such processes are called *resolved* photon processes in contrast to the case where the photon behaves *pointlike*. In this thesis, charm photoproduction is studied at $\overline{W_{\gamma p}} = 88\ GeV$ and $\overline{W_{\gamma p}} = 194\ GeV$. In contrary to light quark jet production where the resolved part is large, heavy quark production in the visible phase space region (where a charmed meson is produced in the detector acceptance) is expected to stem mostly from pointlike photon-proton collisions, the leading order process being $\gamma + g \rightarrow c + \bar{c}$. The measurement of the single inclusive D^*-spectra in p_t and η (presented in chapter three) will provide a crucial test of this production mechanism. The colour flow in charm events is expected to be such that the colours carried by the heavy quarks find their counterpart in the remainder of the proton, a situation which is different from e^+e^--colliders. The region between the proton remnant and the outgoing heavy quarks is therefore expected to be strongly populated. A measurement of the energy flow in D^*-events (chapter three) will test this assumption. As the results will show, charm photoproduction in the visible kinematical range is well described by theory and can therefore be used to directly determine the gluon density in the proton (chapter four). In this chapter, I first describe the connection between electroproduction and photoproduction in the Weizsäcker-Williams approximation. An introduction into the theory of charm photoproduction follows and I will explain how the gluon density in the proton can be determined (including QCD radiative corrections).

1.2 Photoproduction

In photoproduction, the positron can be considered to be equivalent to a broad-band beam of real photons. The calculation of the flux was carried out for the first time in 1934 by C.F. von Weizsäcker and E.J. Williams [1]. A short description of the calculation which follows closely [2] can be found in appendix A. The appropriate form of the WW-approximation is in our case[1]:

$$d\sigma_{ep\to eX}(y) = f_\gamma^{(e)}(y)\sigma_{\gamma p\to X}(y)dy \tag{1.1}$$

$$f_\gamma^{(e)}(y) = \frac{\alpha_{em}}{2\pi}\left\{\frac{1+(1-y)^2}{y}\ln\frac{Q^2_{max}}{Q^2_{min}} - 2\,\frac{1-y}{y}\right\}. \tag{1.2}$$

H1 has two dedicated calorimeters to tag the scattered positrons in photoproduction which are called “e-taggers”. As an illustration I give the numbers for the e-tagger at -33 m which has a wide acceptance in y, ranging from 0.18 up to 0.8. In this analysis, only events within $0.29 \leq y \leq 0.62$ are used, which corresponds to a photon flux of

$$\int_{0.29}^{0.62} dy\ f_\gamma^{(e)}(y) = 1.284\cdot 10^{-2}, \tag{1.3}$$

an average y of

$$\bar{y} = \frac{\int_{0.29}^{0.62} dy\ y\ f_\gamma^{(e)}(y)}{\int_{0.29}^{0.62} dy f_\gamma^{(e)}(y)} = 0.420, \tag{1.4}$$

and an average photon-proton center of momentum energy $W_{\gamma p}$ of

$$\overline{W_{\gamma p}} = \sqrt{4E_pE_e}\cdot\frac{\int_{0.29}^{0.62} dy\sqrt{y}f_\gamma^{(e)}(y)}{\int_{0.29}^{0.62} dy f_\gamma^{(e)}(y)} = 194.01\ GeV. \tag{1.5}$$

The situation for the second e-tagger at -44 m ($0.04 \leq y \leq 0.24$) is different and will be explained in chapter two. It is important to notice that for tagged events the maximum allowed Q^2 (according to equation 6.22) is 0.01 (e-tagger -33 m) and 0.009 (e-tagger -44 m). It has been checked by comparing the leading order charm electroproduction cross section to the corresponding cross section in Weizsäcker-Williams-Approximation, that the neglected non-factorizing terms are smaller than one percent [2]. NLO QED corrections are expected to be roughly of the same size and QCD radiative corrections should not change the quality of the Weizsäcker-Williams-Approximation.

[1] The meaning of the variables and abbreviations is explained in detail in the appendix.

1.3 QCD Calculations

1.3.1 Massive Scheme

For the calculation of a photon-proton cross section, both the point-like and the hadronic photon contribution have to be taken into account [4]:

$$d\sigma^{(\gamma p)}(P_\gamma, P_p) = d\sigma^{(\gamma p)}_{point}(P_\gamma, P_p) + d\sigma^{(\gamma p)}_{hadron}(P_\gamma, P_p). \tag{1.6}$$

Both cross sections can be determined in the pQCD improved parton model if the process is characterized by a hard scale:

$$d\sigma^{(\gamma p)}(s) = \sum_i \int dx_i\, f_i^{(p)}(x_i, \mu_F) d\hat{\sigma}_{\gamma i}(x_i s, \alpha_s(\mu_R), \mu_R, \mu_F, \mu_\gamma) \tag{1.7}$$

$$+ \sum_{i,j} \int dx_i dx_j f_i^{(p)}(x_i, \mu'_F) f_j^{(\gamma)}(x_j, \mu'_F, \mu_\gamma) d\hat{\sigma}_{ij}(x_i x_j s, \alpha_s(\mu'_R), \mu'_R, \mu'_F) \tag{1.8}$$

where the first line corresponds to the direct part and the second line to the resolved photon part. The indices i and j run over all the partons in the proton and the photon respectively and the symbols have the following meaning:

- α_S: Strong coupling constant
- $\hat{\sigma}_{\gamma i}$, $\hat{\sigma}_{ij}$: Partonic cross sections for the collision of a photon with a parton of type i in the proton (direct) and for the collision of two partons of type i and j in the proton and photon respectively (resolved). Sometimes these cross sections are called "subtracted" cross sections because infinities originating from the fact that the partons in the initial state are bound within a hadron are subtracted and absorbed into the parton density functions according to the prescription provided by the factorization theorem.
- μ_R, μ'_R, μ_F, μ'_F: Renormalization scales and factorization scales at the proton side
- μ_γ: Factorization scale at the photon side for the resolved part
- $f_i^{(p)}$, $f_j^{(\gamma)}$: Parton densities in the proton and the photon.

In [6], arguments have been given - based on a detailed examination of low-order heavy quark production diagrams - that the standard perturbative formula of QCD (above) should be reliable for the production cross section of sufficiently *heavy* quarks. The crux is that in the lowest order boson-gluon fusion diagram the internal quark line is off-shell by at least order M^2, where M is the heavy quark mass. In the heavy quark center of mass system, the lifetime of the intermediate state containing the virtual quark is therefore of order 1/M, thus the process is a short-distance one and can be computed in perturbation theory (with the heavy quark mass as the typical scale of the process). The authors leave explicitly open the question whether the charm quark is heavy enough. A measurement of single inclusive D^*-spectra will show that this perturbative framework gives very good agreement with data, at least in the (small) kinematical region explored in this analysis.

The cross section peaks at the threshold at which a typical scale is given by the charm quark mass, as described. For high p_t the transverse momentum itself sets the scale, so that the usual choice for single inclusive distributions is the transverse mass

$$\mu_F = \mu'_F = 2 \cdot \mu_R = 2 \cdot \mu'_R = 2 \cdot \sqrt{m_c^2 + p_t^2}, \tag{1.9}$$

where a factor of two has been introduced for the factorization scales because

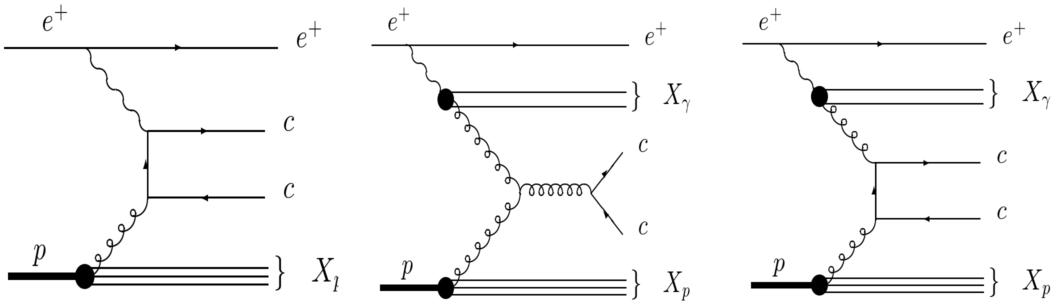

(a) Direct photon (photon gluon fusion graph)

(b) "Resolved photon" process (graph 1)

(c) "Resolved photon" process (graph 2)

Figure 1.1: Leading order charm photoproduction processes. Crossed graphs are not shown.

most parametrizations of the parton densities in the proton are not evolved to such low values like the charm quark mass. The subtracted partonic cross sections $d\hat{\sigma}_{\gamma i}$ and $d\hat{\sigma}_{ij}$ have been fully calculated in NLO QCD [2] (the leading order diagrams are shown in fig 1.1) by several groups [7, 8, 9, 10] and are known since a long time, thus making the photoproduction cross section up to order $O(\alpha_{em}\alpha_S^2)$ a well-established result. Unfortunately the parton densities in the proton $f_i^{(p)}(x_i, \mu_F)$ and the photon $f_i^{(\gamma)}(x_i, \mu_\gamma, \mu'_F)$ can not be calculated yet from the QCD Lagrangian and need to be determined experimentally. They satisfy renormalization group equations. In the case of the proton it is the Dokshitzer-Gribov-Lipatov-Altarelli-Parisi (DGLAP) equation [11]-[13] and for the photon it reads

$$\frac{\partial f_i^{(\gamma)}}{\partial log \mu^2} = \frac{\alpha_e m}{2\pi} P_{i\gamma} + \frac{\alpha_s}{2\pi} \sum_j P_{ij} \otimes f_j^{(\gamma)}, \tag{1.10}$$

[2] In the $\overline{MS}$-scheme.

where the first term, which is not present in the usual DGLAP-equation, results from the direct coupling of the photon to the quarks and is in LO given by

$$P_{i\gamma} = e_i^2(x^2 + (1-x)^2), \tag{1.11}$$

x being the momentum fraction of the parton in the proton and e_i it's charge. The symbol $\otimes$ indicates convolution $(f \otimes g)(x) = \int_x^1 dz/z \cdot f(z)g(x/z)$ and P_{ij} represents the Altarelli-Parisi splitting kernels. While in LO the separation of the direct and the resolved part is unambiguous, in NLO it turns out that they mix and only the sum of both is physically meaningful. The reason is that there are infrared divergences due to the collinear emission of quarks from the incoming photon in the point-like component which are not subject to the KLN cancellation theorem and have to be absorbed into the photon structure function [4]. The scale at which this is done (μ_γ) is arbitrary [3] and a variation of it corresponds to shifting a finite part from the resolved to the direct component or vice versa. But I will keep on talking about direct and resolved part, since in LO they are well defined and the part which can be exchanged is numerically small. The photon parton densities are quite soft and consequently the resolved component can only be important at large center of mass energies and for small masses of the produced system. At HERA with the very asymmetric beam energies, one also expects the resolved part to be mostly forward [4]. This kinematics will be explored with a simple model in chapter three to understand the single inclusive D^*-distributions and it will become obvious that the resolved contribution in the visible range is small.

The above scheme where the mass of the charm quark is fully taken into account in the calculation of the partonic cross sections, and which is therefore reliable also at the threshold, is usually referred to as *massive scheme*. The charm quark is not assumed to be an active flavour in the parton density functions of the proton and the photon. The perturbative calculation stops with massive charm quarks and massless partons (light quarks and gluons) in the final state. The fragmentation of the charm quarks into D^*-mesons is then commonly parametrized by the Peterson-Schlatter-Schmitt-Zerwas (PSSZ) fragmentation function [15]

$$D(x) = \frac{1}{x(1 - 1/x - \epsilon/(1-x))^2} \tag{1.12}$$

where the parameter ϵ needs to be determined from a fit to data from e^+e^--experiments. Such a fit (using a NLO massive scheme calculation) has recently been performed [16] using data from the ARGUS ($E = \mu = 10.6\ GeV$) *and* the OPAL experiment ($E = \mu = 91.2\ GeV$) and yielded $\epsilon = 0.035$.

It is important to notice, that for the extraction of the parameter of the fragmentation function the same type of calculation as for the final application (here: charm photoproduction at HERA) must be used. A leading order extraction results for example in a too high ϵ value of 0.06 [17], because in this case NLO effects are

[3] A consistent choice is $\mu_\gamma = \mu'_F$ [14]

[4] "Forward" denotes the direction of flight of the incoming protons.

compensated by a higher ϵ-value. For previous publications on this subject [18, 19] the NLO calculations have been used together with $\epsilon = 0.06$ (for lack of a NLO fit) which is strictly speaking not correct and leads to a too small cross section for the massive scheme calculation. A quantitative analysis of the effect is given in chapter three.

1.3.2 Perturbative Fragmentation Function Approach

Although the massive calculation is assumed to yield the most reliable results in the small transverse momentum regime $p_T \approx m_c$, for higher values of p_T (where the charm quark mass becomes negligible) large logarithms appear due to gluon emission and gluon splitting [20]. These logarithms can be resummed with the technique of the perturbative fragmentation functions. Two groups have been working independently on this issue (J. Binnewies, B.A. Kniehl, M. Krämer, G. Kramer, M. Spira [21, 22] and ref. therein and M. Cacciari, M. Greco [23, 24, 20] and ref. therein) with slightly different approaches of which the perturbative part has been shown to be equivalent [23]. I therefore restrict the discussion on the calculation described in detail in [23].

In the perturbative fragmentation function scheme, the charm quark mass is neglected for the calculation of the hard scattering matrix elements. This should be a reasonable approximation for $p_t \gg m_c$. Charm is considered as an active flavour of the proton and the photon like the lighter quarks u,d and s and therefore appears in the parton density functions of the colliding beams. The partonic cross sections for the scattering of massless partons into massless quarks and gluons are used, both for the direct and the resolved part (in the $\overline{MS}$-scheme). The following Ansatz for the fragmentation function (FF) of a parton i into a D-meson was made:

$$D_i^D(x,\mu) = D_i^c(x,\mu) \otimes D_{np}^D(x). \tag{1.13}$$

The first term, $D_i^c(x,\mu)$, is the perturbative fragmentation function for a massless parton to fragment via perturbative QCD cascade into a massive charm quark and the second expression $D_{np}^D(x)$ stands for the non-perturbative fragmentation function which describes the transition of the heavy quark into the D-meson. While the dependence of the perturbative FF's on the scale is given by the Dokshitzer-Gribov-Lipatov-Altarelli-Parisi (DGLAP) equation, the calculation of the pFF at a starting scale μ_0 within perturbative QCD needs a special formalism, developed in [26]. The nonperturbative contribution has to be parametrized as in the case of the massive scheme calculation, and the PSSZ-fragmentation function is also the typical choice here. The parameter ϵ has been extracted using the pFF-calculation and was found to be 0.02 in this case.

Massless calculations are designed to be reliable and more accurate than the massive calculations in the high p_T regime since the large logarithms appearing there can be resummed in the evolution of the pFF [20]. The scale dependence is therefore smaller in this region than for the massive calculation. In the low and intermediate p_T region, on the other hand, this massless resummation misses finite mass terms and it is expected to be less reliable and accurate. A total cross section can not be calculated within the massless scheme. Due to unresummed large terms, these calculations are also unreliable when the other limits of the phase space which are related to the charm quark mass are probed. The differential cross section in the rapidity (η) of the reconstructed D^* (chapter three) is such an example where the D^*-mass together with the applied p_T-cut of 2 GeV (2.5 GeV) sets a production threshold.

Clearly at very low and intermediate p_T and close to phase space boundaries, as for example in this analysis, *the massive scheme calculation is the reference.* It is nevertheless interesting to see how well the massless calculations perform.

The parton density functions used in massive and massless calculations are not the same. While the massive scheme starts without a charm contribution in the proton and the photon, and - as we will see - is able to explain the measured cross sections in this analysis, in the massless scheme one needs a content of massless charm in the proton and may be also in the photon.

The relative size of the direct and the resolved contributions is also very different in the two approaches. While in the massive scheme, the visible resolved contribution is very small as already mentioned, it is of the same order as the direct part in the massless scheme, a fact which is not surprising since the same holds for light quark production as is well known.

1.4 Alternative Production Mechanisms

Another source of charm could be that the (non-perturbative) wavefunction of the proton or the hadronic photon contains a non-negligible amount of charm ("intrinsic charm"). Indeed in some fixed-target experiments, hints of such intrinsic charm in the proton have been found (ref. [27]-[31]). But a thorough analysis by the H1 collaboration [32] came to the conclusion that the contribution of intrinsic charm to the visible cross section at HERA is negligible. Intrinsic charm in the photon is expected to have a striking experimental signature in the form of a prominent photon remnant since there is a spectator charm quark in this process. As will be seen in chapter three, there is no indication of such a signature.

1.5 D-Mesons

About 90% of the charm quarks fragment into D-mesons (the rest into charmed baryons). 45% pick up a $\overline{u}$, another 45% a $\overline{d}$ and 10% a $\overline{s}$. The QCD ground- ($^1S_0$-) state of a charm quark and a $\overline{u}$ quark is called a D^0-meson, the ground state with a $\overline{d}$ or a $\overline{s}$ is a D^+ or a D_s respectively.

A fraction of 0.45 of the $c\overline{d}$-pairs fragment into the $^1S_0$-state D^+ while a fraction of 0.5 goes to the $^3S_1$ states (the remaining 5% are higher states).

A decay of these particles is only possible via weak decay of the charm quark and that's why they have macroscopical lifetimes of $c\tau \approx 100 - 300\ \mu m$. The biggest contribution to the mass ($\approx 1.865\ GeV$) comes from the charm quark mass [5] ($1.0 - 1.6\ GeV$) [34]. Higher order $^3S_1$-states (D^{*+}, D^{*0} and D_s^*) decay strongly or electromagnetically into the ground states.

The most accurate measurement for the branching ratio $c \rightarrow D^{*+} \rightarrow D^0\pi^+ \rightarrow K^-\pi^+\pi^+$ which will be needed for the comparison of the measured $D^{*\pm}$ cross sections to QCD calculations and the extraction of the gluon density comes from a combined analysis of data from all four LEP experiments [33] and is $(7.1 \pm 0.5) \cdot 10^{-3}$.

1.6 Determination of the Gluon Density

1.6.1 Methods to Measure the Gluon Density

The gluon density in the proton is usually determined from a QCD-analysis of the scaling violations of the proton structure function F_2 [35, 36]. For small x and in leading order the connection between F_2 and the gluon density is given by

$$\frac{dF_2(x,Q^2)}{d\log Q^2} \approx \frac{10\ \alpha_s}{9\pi} \int_0^{1-x} dz P_{qg}(z) x f_{g/p}(x/(1-z), Q^2), \tag{1.14}$$

where P_{qg} stands for one of the LO Altarelli-Parisi splitting kernels, which can be computed in perturbative QCD. Such a determination involves the heavy use of the Altarelli-Parisi equations and is therefore indirect and (to some extent) it is also dependent on the specific parametrization chosen for the fits of F_2. Direct photon [37, 38, 39] and jet [40, 41] production in hadronic collisions are processes which are directly sensitive to the gluon content of the proton and have been used to extract $f_{g/p}(x_g, \mu^2)$. While the prompt photon process gives valuable information in the range $0.01 \leq x_g \leq 0.6$, the dijet rates provide constraints in a lower range in x_g from to 0.005 to 0.05 but do not reach the same level of precision. Additionally they probe at scales $\mu^2 \approx 10^3 - 10^4\ GeV^2$ where the the different parametrizations of the gluon density tend to become very similar.

HERA offers several opportunities to measure the gluon density directly at low x and at lower scales. The probably most promising is based upon the measurement of the longitudinal structure function [42], which is proportional to the gluon density. In LO holds

$$F_L(x,Q^2) \approx \frac{2\ \alpha_s}{3\pi} \frac{1}{1.77} \frac{x}{a}\ x\ f_{g/p}(x/a, Q^2) \tag{1.15}$$

$$a = 0.4 \tag{1.16}$$

The measurement of F_L is clearly one of the physics goals of HERA and will be done in the future. Another method which has been proposed [43] and is experimentally very convenient is the study of inelastic J/ψ production. Unfortunately it suffers (until now) from severe theoretical ambiguities due to difficulties in the computation of the needed cross section. In contrast to these two methods, a direct determination

[5] $\overline{MS}$ mass

of $f_{g/p}(x_g, \mu^2)$ from the (2+1)-jet rate in deep inelastic scattering has been performed and published by the H1 collaboration [44]. A range of $2 \cdot 10^{-3}$ up to 10^{-1} in the momentum fraction x_g has been explored at an average scale of $< Q^2 >= 30\ GeV^2$. Two graphs contribute in leading order (at which the analysis was done) to the (2+1)-jet rate: The photon gluon fusion (PGF) graph and the QCD compton graph. While PGF is sensitive to the gluon density, the compton graph probes the quark content of the proton and has to be considered as background. Both contributions are of similar size and that is the main disadvantage of the method.

1.6.2 The Open Charm Method

The open charm method can be viewed as a derivative of the mentioned (2+1)-jet rate measurement. The basic idea is that charm quarks are always produced in pairs so that in LO only the photon-gluon fusion process $\gamma + g \to c + \overline{c}$ (fig. 1.1a) contributes. An analysis can be carried out both using a sample of photoproduction or deep inelastic scattering events. I will discuss in the following the photoproduction case and comment on the specific advantages and disadvantages later on.

The Principle In a small range of x_g, the following relation holds in LO and for a fixed $W_{\gamma p}$:

$$\frac{\Delta\sigma}{\Delta x_g} \approx \hat{\sigma}_{\gamma g \to c\bar{c}}(\hat{s}, < \mu_F^2 >_{\Delta x_g})\ f_{g/p}(x_g, < \mu_F^2 >_{\Delta x_g}) \tag{1.17}$$

where $< \mu_F^2 >_{\Delta x_g}$ stand for the average of μ_F^2 over all events in the given small interval Δx_g. The same approximation holds if y is allowed to vary in a narrow range instead of being fixed.

Assuming that $\Delta\sigma/\Delta x_g$ can be measured, the gluon density is now easily extracted by dividing the measured differential cross section in bins of x_g by the partonic cross section $\hat{\sigma}$:

$$f_{g/p}(x_g, < \mu_F^2 >_{\Delta x_g}) \approx \frac{\Delta\sigma}{\Delta x_g \cdot \hat{\sigma}_{\gamma g \to c\bar{c}}(\hat{s}, < \mu_F^2 >_{\Delta x_g})}. \tag{1.18}$$

It is important to notice that every bin probes at another factorization scale which can be obtained from a QCD calculation or, given enough statistics, also from data using an appropriate variable.

Determination of x_g The next step is to find an observable which is strongly correlated with x_g. Many methods have been proposed [45]:

- Reconstruction of the invariant mass $\hat{s}$: The approximation for $\hat{s}$ by the transverse mass can also be applied for the particles after the fragmentation process: $\hat{s} \approx \sum_i m_{T,i} \approx \sum_i p_{T,i}$ where the sum runs over all particles in the final state. This method might work for high p_T events but not for the sample which will be analysed here. While for the scale the approximation is good, it is not for x_g since the gluon density is much stronger dependent on x_g than on μ_F^2.

- Using jets ($E_T \geq 7\ GeV$): A reconstruction of both charm jets determines also the kinematics of the event, e.g. x_g. This is probably the most promising method for the future when enough statistics will be available. The H1 silicon vertex detector will be very helpful in tagging the charm events and increase the statistics considerably.

- Using conservation of energy and longitudinal momentum, the following relation holds precisely in LO [6]:

$$x_g = \frac{\sum_{c\bar{c}-system}(E + p_L)}{2\ E_p}, \tag{1.19}$$

  where the sum runs over all the particles in the final state originating from the fragmentation of the charm quarks. The specific problem in this method is to disentangle the $c\bar{c}$-system from the proton remnant. Monte Carlo studies show, that for $W_{\gamma p}$ of about 190 GeV (or higher), it is feasible to distinguish the charm system from the remainders of the proton. But at 88 GeV, at which a large fraction of the collected data is found, it happens often that one charm quark mixes into the proton remnant and the separation is arbitrary. Therefore this method can not be applied to the full data sample but a fraction of it will be analysed in this way to cross check the results obtained by the following method.

- Reconstruction of the four momentum of one meson containing a charm quark and calculating back to the charm quark level. Given the momentum of one charm quark the calculation of x_g is unambiguous in LO. This is the best method for the present data sample and statistics.

It is easy to verify that in LO holds

$$x_g = \frac{\hat{s}}{y \cdot s} \tag{1.20}$$

$$\hat{s} = \frac{p_t^2 + m_c^2}{z(1-z)} \tag{1.21}$$

$$z = \frac{E - p_L}{2 \cdot y \cdot E_e}. \tag{1.22}$$

where E, p_L and p_T refer to one charm quark. The variable z is sometimes called "inelasticity" [7]. The momentum of the charm quark can be approximated by

$$p_t = 1.2 \cdot p_t(D^*) \tag{1.23}$$

$$p_L = p_L(D^*). \tag{1.24}$$

[6] The corresponding relation for y is usually called Jacquet-Blondel equation.

[7] If z denotes the inelasticity calculated from the charm quark c, then (1-z) is the corresponding inelasticity of the anticharm $\bar{c}$, so that for the calculation of x_g it doesn't matter which charm is used to calculate z since the expression for $\hat{s}$ contains z and (1-z) symmetrically.

The factor 1.2 has been optimised to minimize migrations. The best choice of this scaling factor depends on the value of $\epsilon_{Peterson}$ used for the calculation and the systematic error from a variation of the factor 1.2 will be contained in the systematic error obtained by a variation of the parameter $\epsilon_{Peterson}$.

Background As mentioned before, not only the photon-gluon fusion process (direct) but also the hadronic component of the photon contributes in leading order. The resolved photon part (which is already small in the visible range) will be further reduced by appropriate cuts and become negligibly small. It's contribution (of about 0.5-5 percent in the massive scheme, strongly depending on the photon structure function) will be a systematic error in the measurement.

Fig. 1.2 shows the correlation between generated x and the reconstructed values x_g^{rec} (calculated in the massive scheme) for the direct photon process only. In LO (left), a nice correlation with a short tail on one side can be observed. This tail is due to the fragmentation function. The picture on the right shows the same difference in NLO where a long tail shows up which is due to initial state gluon radiation and quark induced processes $\gamma q \rightarrow q c\bar{c}$.

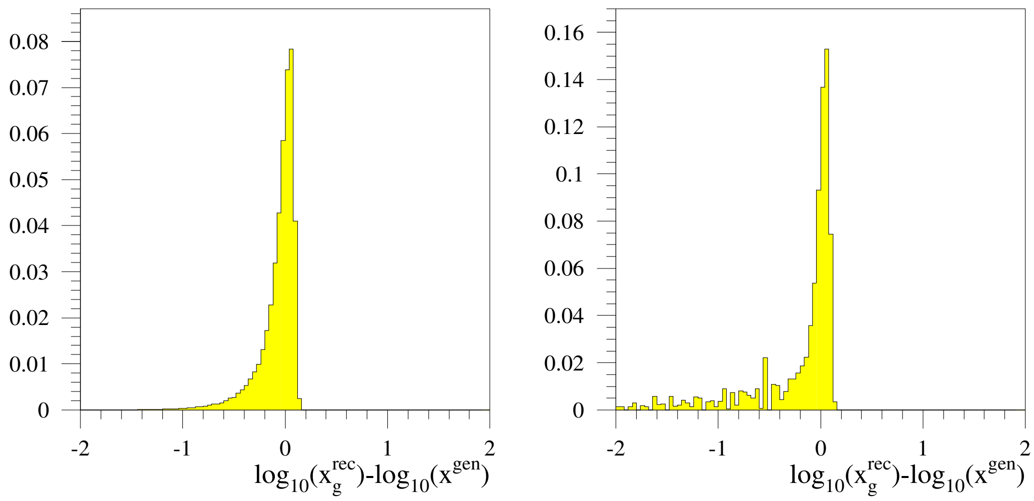

Figure 1.2: Difference between generated and reconstructed x in LO (left) and LO+NLO (right). The massive scheme calculation with a PSSZ fragmentation function ($\epsilon = 0.035$) has been used at a fixed γp-center of mass energy of $W_{\gamma p} = 194\,GeV$, corresponding to the data sample triggered by the e-tagger at -33 m.

Inclusion of Radiative Corrections While in LO only the photon-gluon fusion process $\gamma g \rightarrow c\bar{c}$ contributes to charm production in the analysed phase space, in NLO it also proceeds via photon-quark collisions $\gamma q \rightarrow q c\bar{c}$. The interpretation of x_g^{rec} as the momentum fraction of a gluon is not valid any more and only on a statistical basis it is possible to extract information on the gluon density, using the well known quark densities as an input. Moreover even in the case when the process is initiated by the photon and a gluon in the proton in a process $\gamma g \rightarrow gc\bar{c}$, the interpretation of x_g^{rec} as the momentum fraction of the initiating gluon is invalid since in these $2 \rightarrow 3$ particle processes the kinematics is different from the one in LO. The inclusion of radiative corrections must therefore be done by unfolding the measured cross section $d\sigma/dx_g^{rec}$ to the "true" values $d\sigma/dx^{gen}$ using the appropriate QCD calculation. The quark induced part can be subtracted after the unfolding, so that only a quantity directly proportional to the gluon density is left. As will be seen in chapter four, the quark contribution is comparatively small and the tails in the correlation between x_g^{rec} and x^{gen} mainly due to initial state gluon radiation. In fact, the inclusion of radiative corrections is not a complication but allows to extend the probed kinematical region in x_g to higher values.

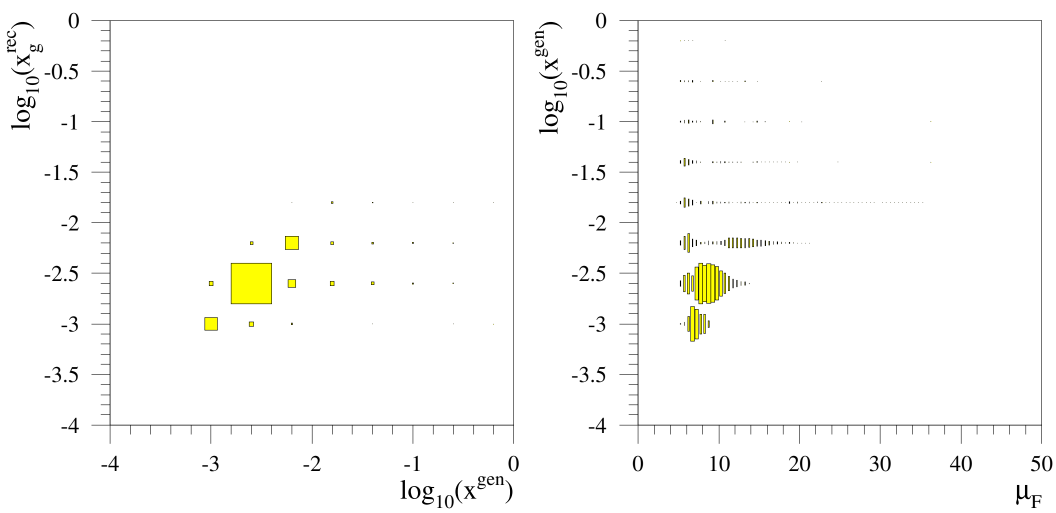

Figure 1.3: Unfolding matrix from the observed value x_g^{rec} to the generated x_g^{gen} for $\overline{W_{\gamma p}} = 194\ GeV$ (e-tagger at -33 m) according to the NLO massive scheme calculation (left). The picture on the right hand side shows the correlation between x_g and the factorization scale μ_F for the analysed sample as described in the text. The prominent peaks on the diagonal are the LO contribution. It is restricted to the three lowest bins in x_g. The other area is only accessible via radiative events where x_g and μ_F^2 are not well correlated any more.

Summary The full procedure of the measurement can be summarized as follows:

- The cross section $d\sigma_{\gamma p \rightarrow D^* X}/dx_g^{rec}$ is measured with x_g^{rec} being defined according to equations 1.20-1.24.
- The measured cross section $d\sigma/dx_g^{rec}$ is unfolded to the "true" values $d\sigma/dx^{gen}$, using the appropriate massive scheme NLO calculation [14].

- The contribution from processes $q + \gamma \rightarrow c + X$ is subtracted relying on the same calculation.
- The gluon density is obtained in several bins of x_g by dividing the measured differential cross section $d\sigma/dx_g^{gen}$ by the subtracted partonic cross sections from the QCD calculation, where every bin corresponds to another average scale μ_F.
- The average factorization scale μ_F for each bin in x_g is determined from the NLO QCD calculation (fig. 1.3).

Overview Over the Theoretical Uncertainties The theoretical uncertainties are the following:

- The perturbative calculation of the subtracted partonic cross section stops at NLO. Higher order corrections are large, as the scale dependences show. The systematic error can be estimated by varying the renormalization scale (typically by a factor of 2).
- The charm quark mass is poorly known. In principle this introduces an additional error which should be estimated by varying the charm quark mass separately from the renormalization scale, also since the mass is a physical parameter and the scale is not. On the other hand, the renormalization scale and the charm mass are strongly correlated by definition and therefore an independent variation would certainly overestimate the systematic error. I will therefore only vary the renormalization scale.
- The partonic structure of the photon is poorly known and the systematic error introduced by it will be estimated using different photon parton density parametrizations.
- The fragmentation function of the charmed meson is known with good precision from e^+e^- experiments and I assume that the fragmentation function in that process is the same as in γp-collisions. Several different parametrizations have been used in the past to describe the data and a variation of the parametrization could be used in principle to determine the systematic error coming from this side. Unfortunately, only the PSSZ fragmentation function is implemented in the NLO calculation and therefore the error can only be estimated by varying the parameter ϵ.

The outlined analysis can be carried out both in photoproduction and in DIS and most of the systematic uncertainties are common to both cases. The only specific advantage of deep inelastic scattering is that the signal to background ratio is better for tagging the D^*. The problem of the choice of the scale (the factor 2 in μ_F) is not unique in photoproduction, it might even be worse in deep inelastic scattering since in this case an additional scale appears in the process, namely the virtuality

Q^2 of the photon, and it is unclear yet if for example $\sqrt{m_c^2 + Q^2}$ or $\sqrt{m_c^2 + p_t^2}$ is the appropriate choice.

In photoproduction one might argue (having in mind the somewhat poor description of low-energy fixed target results by perturbative QCD [4]) that the production mechanism of charm is not well understood and one can speculate that other production mechanisms like intrinsic charm in the photon or flavour excitation play a significant role.

I will therefore first investigate the production process using single inclusive D^*-spectra and a measurement of the energy flow in chapter three. As we will see, tagged photoproduction of D^*-mesons at HERA is very well described the explained QCD model and no signals of a competing production process are visible.

Chapter 2

The H1 Detector at HERA

2.1 The HERA storage ring

HERA consists of two independent storage rings for the proton (820 GeV) and the positron beam (27.5 GeV). It is used at four places spaced evenly along its 6.3 km circumference for high energy physics experiments: In the east hall, the HERMES collaboration investigates the spin structures of the proton and neutron by deep inelastic scattering of the polarised positrons off various polarised targets. The west hall is the home of the HERA-B experiment, which will use an internal target in the proton beam to detect CP-violation in the b-system. The halls south and north respectively are reserved for the two colliding beam experiments ZEUS and H1. To preaccelerate the particles to the HERA injection energies of 12 GeV (positrons) and 40 GeV (protons), the older storage rings DESY and PETRA were adapted for this purpose. Some collider parameters relevant for the physics experiments are listed in table 2.1. Specific for HERA and important for the design of the detectors are the short time difference between bunch crossings (96 ns) and the highly asymmetric beam energies.

The free space at the H1 interaction region is restricted to ± 5 meters by the last two focusing quadrupoles. The electron beam is deflected by several excentric quadrupole magnets and a dipole magnet at a position of about -25 m by 10 mrad to achieve head on collisions. The main components of the H1 detector are shielded against the produced synchrotron radiation (the characteristic energy is 70 keV) by a system of collimators and absorbers which reduce the photon flux by eleven orders of magnitude [46]. The main backgrounds to e^+p-collisions are [47]

- Proton beam induced background: Interactions of the proton beam with residual gas or the beam pipe. These events are usually characterized by a vanishing $E - p_z$ and very many tracks with a small angle to the proton beam direction.

- Proton beam satellites: A run dependent fraction of protons are found between two regular bunches. They may collide with the positron beam or with residual gas at different z-position.

- Positron beam induced background: The main contribution comes from secondary particles which are produced when an positron or a highly energetic photon from synchrotron radiation hits the beam pipe or a collimator. The events show usually a high number of large local charge deposits in the tracking chambers pointing to photon conversion and a high but inhomogenously distributed energy deposit in the backward calorimeter.

Only a very small fraction of the interactions is a wanted e^+p-collision. It is the task of the first level trigger to suppress this abundant background. The rates of the proton and electron beam induced backgrounds are estimated during data taking by the rates of the time of flight system (TOF). These rates are used to decide whether the high voltage for the trackers can be switched on safely, and for tuning the beam optics by the HERA machine group. H1 also provides information about the beam positions at the interaction point (measured with the luminosity system) to enable a fast optimisation of the luminosity.

	e^+	p
energy * (GeV)	30	820
energy spread * (10^{-1})	0.91	0.2
RF frequency * (MHz)	500	52
bunch length * (cm)	0.83	8.5
beam width σ_x * (μm)	280	265
beam width σ_y * (μm)	50	50
crossing angle (deg)	0	
Δt between crossings (ns)	96	

year	94		95		96	
	e^+	p	e^+	p	e^+	p
beam energy (GeV)	27.58	819.90	27.54	820.77	27.57	821.57
number of bunches	153+15	153+17	174+15	174+6	175+14	175+6
$< I >$ (mA)	17.0	41.0	18.4	54.0	20.6	60.26
$\int L$ (pb^{-1})	2.9		10.1		13.3	
$L\,peak$ ($cm^{-2}s^{-1}$)	$4.3 \cdot 10^{30}$		$5.9 \cdot 10^{30}$		$8.3 \cdot 10^{30}$	
$< L >$ ($cm^{-2}s^{-1}$)	$1.4 \cdot 10^{30}$		$2.1 \cdot 10^{30}$		$2.6 \cdot 10^{30}$	

Table 2.1: HERA collider parameters. Design values are marked with *.

2.2 The H1 Detector

2.2.1 Overview

A detailed description of the H1 detector can be found in [48].

The measurement of the proton structure functions in deep inelastic scattering and the search for previously undetected particles within or beyond the standard model were the main motivations to build HERA and H1/ZEUS. In the design of the H1 detector, prime attention has therefore been given to the clean identification of the scattered positrons and the measurement of their energy and scattering angle as well as the good reconstruction of hadronic final states. The measurement of the scattered positron and the hadronic final state in deep inelastic scattering events allows a redundant determination of the event kinematics and is a major innovation compared to fixed target experiments.

Fig. 2.1 shows a 3-dimensional view of the H1 detector. The protons enter the interaction zone from the right side, the positron beam comes from the left. A quadrupole magnet (7) compensates the effect of the beam-beam interaction. The H1 detector is asymmetric to account for the highly asymmetric beam energies. Although the laboratory system is a good approximation to the partonic center of momentum system in most of the hard collisions, energy flow measurements and the detection of the events with highest Q^2 profit significantly from the hermetic and homogenous coverage of the forward region. A large superconducting coil (6) producing a magnetic field of 1.2 Tesla enclosing both the electromagnetic (4) and the hadronic (5) section of a highly granular liquid argon calorimeter was chosen. The main calorimeter is supplemented by a high resolution jet chamber for tracking in the central part of the detector and a forward drift chamber. The backward region which gives access to the tracking devices during shutdown is hermetically covered by a thin drift chamber (BDC) and a spaghetti calorimeter with an electromagnetic and hadronic section (12) [1]. The return yoke (10) is equipped with limited streamer tubes for the detection of highly energetic muons. Muons in the forward region ($3° \leq \theta \leq 17°$) are detected in the forward muon chambers (9).

Not shown in the picture are the vertex detector, a silicon microstrip detector with two layers (operational since spring 1997), the backward silicon tracker (BST), the forward neutron counter and the forward proton spectrometer. Also missing are the scintillator walls (TOF system) on both ends of the detector which are vital for suppressing beam induced background.

The luminosity is measured by counting the rate of the Bethe-Heitler process. A positron detector at $-33\ m$ and a photon detector at $-103\ m$ have been installed for this purpose. The positron detector also serves to measure the energy of the positron in photoproduction events with high accuracy. A second and similar positron detector for tagging photoproduction is installed since 1995 at $-44\ m$, it covers a different photon-proton center of mass energy.

[1] Since spring 1995. The picture refers to the previous backward electromagnetic calorimeter BEMC which had no hadronic section. The BDC was installed together with the new calorimeter.

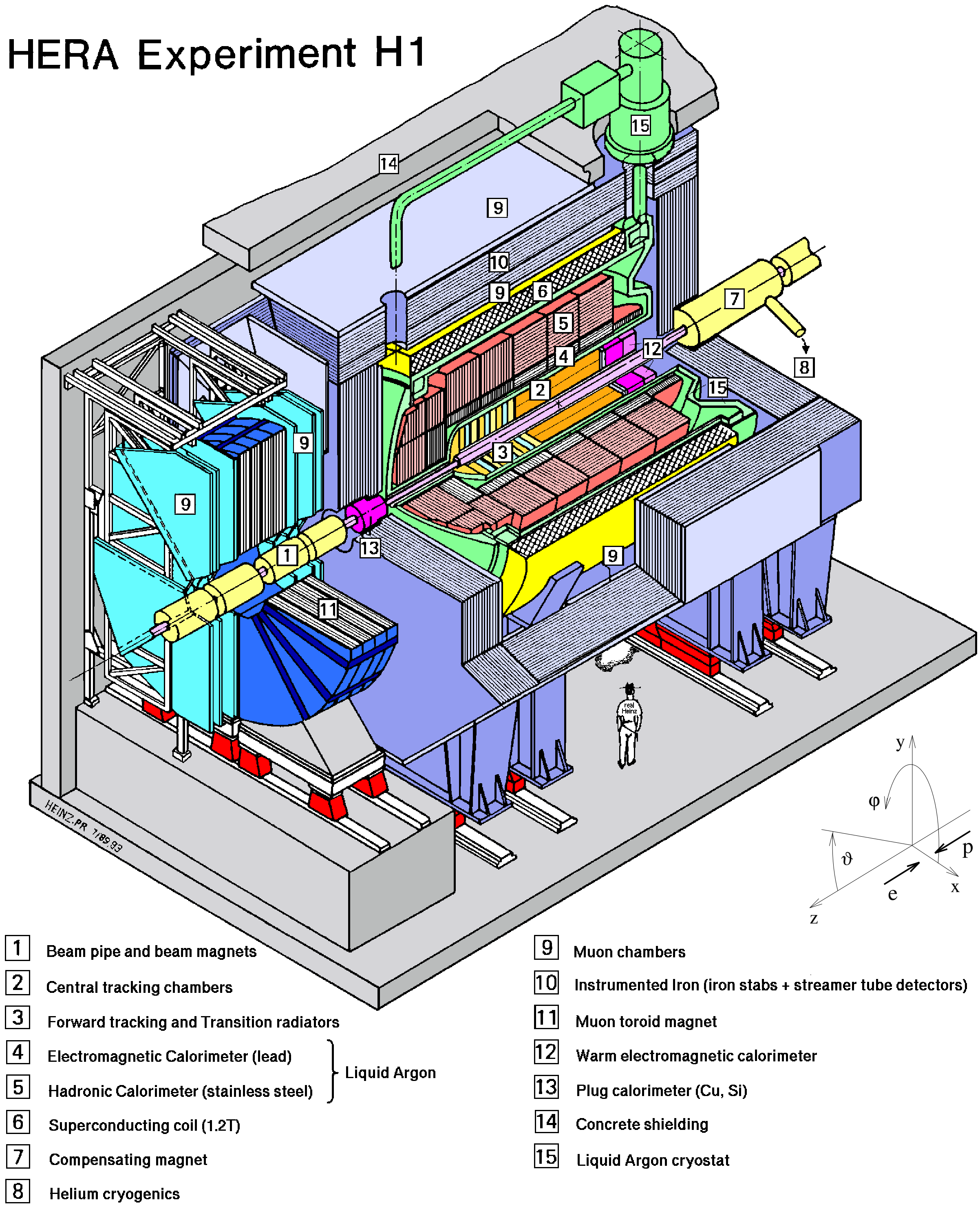

Figure 2.1: The H1 detector with its main components. On the right the coordinate system as used in the H1 collaboration is defined.

2.2.2 The Luminosity System

Luminosity Measurement H1 determines the luminosity by measuring the rate of the elastic scattering (Bethe-Heitler) $e^+p \to e^+\gamma p$ [49]. The cross- section for this QED process is known with high precision. To subtract the background from interactions between positrons and the residual gas, the pilot bunches [2] are used and the luminosity calculated as

$$L = \frac{R_{tot} - (I_{tot}/I_0)R_0}{\sigma_{theor}} \tag{2.1}$$

where R_{tot} is total rate of bremsstrahlung events, R_0 the rate in the pilot bunches, $\frac{I_{tot}}{I_0}$ the ratio of the corresponding beam currents and σ_{theor} the calculated cross section. H1 has detectors for both the positron and the photon in the final state. For the online luminosity measurement and the beam steering, the rate of coincidences of a photon and a positron is used, whereas for the offline determination of the integrated luminosity the single photon rate (above a threshold of 10 GeV) is taken, which gives a slightly smaller systematic error [50].

The energy and position of the scattered positrons are measured in the so-called electron tagger, a Čerenkov calorimeter with a thickness of 21.5 radiation lengths, which is located at -33 m (ET 33).

Photons are detected in the photon-detector (PD) at a position of -103 m. The same crystals (TlCl/TlBr) as for the ET 33 are used, also the radiation length is the same. To protect the PD from the high flux of synchrotron radiation, it is shielded by a Pb filter (thickness 2 X_0) followed by a water Čerenkov counter (VC, thickness 1 X_0).

The calorimeters are calibrated online using the constraint $E_\gamma + E'_{e^+} = E_{e^+}$.

	unit	ET	PD
range in E_γ/E_e		0.2 - 0.8	0.004 - 1.
polar angle acceptance	mrad	0 - 5	0 - 0.45
Aperture x × y (granularity)	mm^2	154 × 154 (7 × 7)	100 × 100 (5 × 5)
Chemical composition		TlCl(78%)+TlBr(22%)	
Radiation length (Molière radius)	cm	0.93 (2.10)	
Crystal length (radiation hardness)	cm (Rad)	20 ($> 6 \cdot 10^7$)	
Energy resolution σ_E/E	%	$1 \oplus 13/\sqrt{E}$ (E in GeV)	
Position (time) resolution	mm (ns)	0.3-1.2 (≤ 3)	

Table 2.2: Parameters of the Luminosity System.

[2] Pilot bunches have no corresponding bunch to collide with in the other beam.

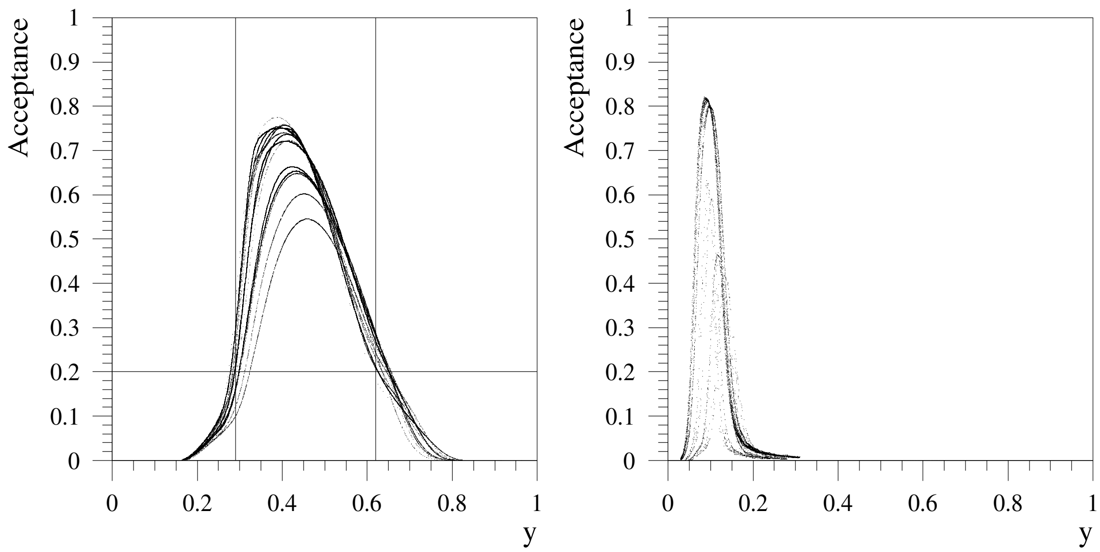

Figure 2.2: Acceptance of the positron detectors as a function of the momentum fraction of the positron carried by the photon (y). Left: Tagger at -33 m. Right: Tagger at -44 m. The curves correspond to different beam positions. The vertical lines in the left figure mark the used range in y whereas the horizontal line indicates a weight of five (see text), the maximum weight used in the analysis.

Photoproduction The two positron detectors at -33 m and at -44 m are used in this analysis to measure the scattered positrons in photoproduction events. Their acceptance in the variable $y = \frac{E-E'}{E}$, which represents the momentum fraction of the incoming electron carried by the photon (in the Weizsäcker-Williams picture), is shown in figure 2.2. The two detectors have to be treated differently in the analysis.

E-tagger at -33 m In this case, only positrons which are at least 1.2 cm away from the edge of the crystal (in the accelerator plane) are used in this analysis to minimize leakage and ensure a precise energy measurement. To correctly measure a photoproduction cross section without biasing the result by the acceptance of the tagger, each event has to be weighted with the corresponding weight given by the inverse of the acceptance. A restriction in the accepted range in y from 0.29 to 0.62 limits the weights to be smaller than about a factor of five. This is necessary since we are dealing with a small number of events and a single event with an extremely high weight could easily distort all distributions. The average $W_{\gamma p}$ and y and the photon flux for this tagger have been calculated in chapter one.

E-tagger at -44 m For the second positron detector, the situation looks different. Most of the positrons hit the crystal right at the edge and a cut on the reconstructed position of the positron would result in a loss of most of the available statistics. But since the acceptance of this tagger is already very small compared to the previous case (fig. 2.2), the approximation of a constant $W_{\gamma p}$ is good and there is no need to weight the events separately. The measured average weight for the events is $5.56 = 1/0.18$. For the determination of the average $W_{\gamma p}$, the acceptance of the tagger weighted with the photon flux is taken into account:

$$\overline{W_{\gamma p}} = \sqrt{4E_pE_e} \cdot \frac{\int_0^1 dy\sqrt{y}\ A(y)\ f_\gamma^{(e)}(y)}{\int_0^1 dy\ A(y)\ f_\gamma^{(e)}(y)} = 88\ GeV. \tag{2.2}$$

where A(y) denotes the tagger acceptance. The corresponding photon flux in the range where A(y) is not zero is

$$\int_{0.02}^{0.32} dy\ f_\gamma^{(e)}(y) = 8.38 \cdot 10^{-2}. \tag{2.3}$$

To be very explicit, in both cases the measurement of the cross sections will be given at an average photon-proton energy, but the effect of the acceptance of the e-taggers is once (e-tagger at -33 m) taken into account in the determination of the number of events and in the other case in the calculation of the average photon-proton energy.

2.2.3 Central Jet Chamber

2.2.3.1 Design

Track reconstruction in the central region (fig. 2.4) is based on two concentric cylindrical drift chambers, CJC1 and CJC2, centered at the nominal interaction point. Their design followed closely the jet chambers used for the JADE experiment at PETRA [51]. They provide simultaneously track triggering, reconstruction and (in a limited momentum range) particle identification. The inner jet chamber (CJC1) consists of 30 drift cells with 24 signal wires each. It's active length is 2.2 meters, covering an angular range from 20° to 160°. The wire direction is parallel to the z-axis, so that the $r\phi$-coordinate can be measured using the drift time information. Information on the z-coordinate of a hit is available from charge division: $z = \frac{l_{eff}}{2}\frac{Q^+-Q^-}{Q^++Q^-}$, where $Q^\pm$ denote the charge measured on both ends of a wire and l_{eff} is the effective length of the wires. To account for the magnetic field, all drift cells are tilted by about 30°. The ionization electrons from stiff tracks originating at the z-axis therefore drift perpendicular to the track direction. This gives optimum track resolution and resolves the usual drift chamber ambiguity (mirror hits) when the track segments from different cells are combined. A closer inspection of a single drift cell reveals that adjacent sense wires are separated by two potential wires, which reduces the surface field and cross talk, and which allows to adjust drift field and gas amplification nearly independently. The outer chamber (CJC2) has 60 cells with 32 wires and is similar to CJC1. Both chambers have their own gas system, but are operated with the same gas (various mixtures have been tried in the three years). A typical Lorentz angle is 40°, the drift velocity being around 50 $\mu m/ns$. The following resolutions have been achieved:

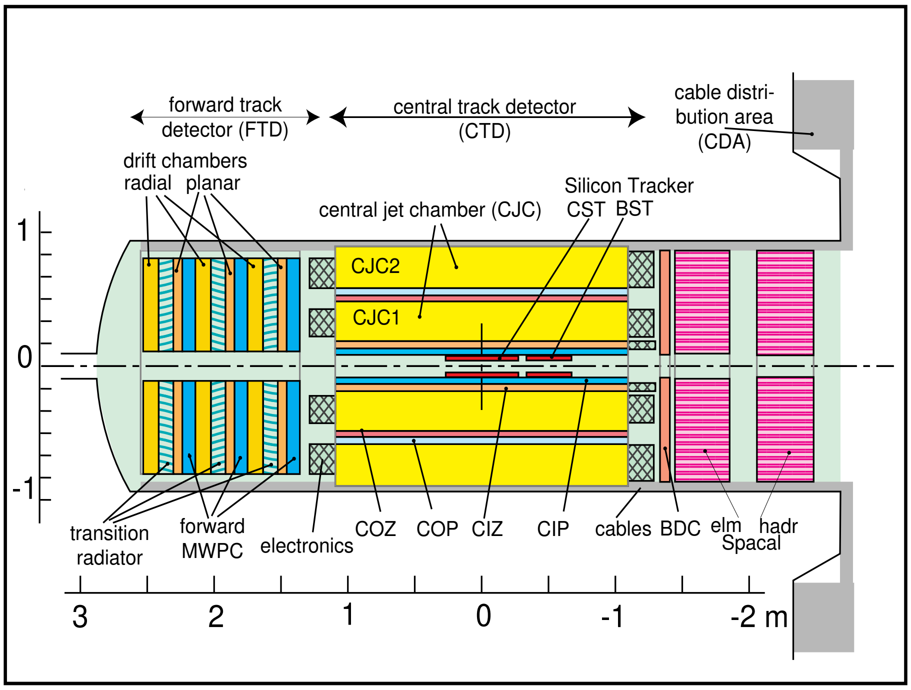

Figure 2.3: Tracking devices of the H1 detector.

- Point resolution in $r\phi$ (drift coordinate): 145 μm
- Z-Resolution (from charge division): 25 mm
- Double track resolution: 2.5 mm
- dE/dx resolution: 10 %
- p_T resolution: $\sigma_{p_t}/p_t = 0.5\%\ GeV^{-1} \cdot p_t$

2.2.3.2 Track Reconstruction

Principle Since the resolution in the drift coordinate $r\phi$ is much better than in z, track finding is based almost completely on that information. A first estimate of the event t_0 is provided by the threshold in the drift time histogram. The track finding program then searches first for triples of hits. κ and ϕ of these small track segments are then estimated by making the assumption that they are part of tracks coming from the nominal interaction vertex. Accumulations in the $\kappa - \phi$ histogram indicate tracks, which are fitted (with a fast, non iterative procedure) to a circle in the $r\phi$-plane:

$$\frac{1}{2} \cdot \kappa \cdot (r^2 + d_{ca}^2) + (1 - \kappa \cdot d_{ca}) \cdot r \cdot sin(\Phi - \phi) - d_{ca} = 0 \tag{2.4}$$

The symbols have the following meaning:

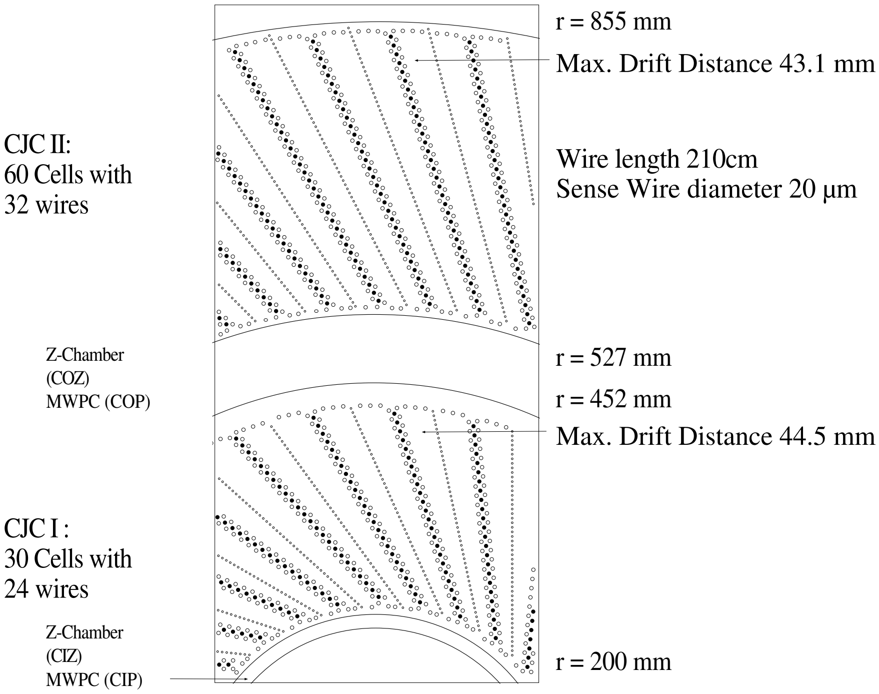

Figure 2.4: Central tracking system, section perpendicular to the beam.

- r: Radius of the circle, κ: Inverse radius of the circle (in cm^{-1}). Positive tracks have a negative sign and vice versa.

- d_{ca}: Distance of closest approach of the circle to the z-axis. d_{ca} gets the sign of (the z-coordinate of) $\vec{d_{ca}} \times \vec{p_t}$.

- Φ: Angle at the point closest to the axis.

Outlyers are removed for the fit. A hit can only be used for a single track. The remaining two parameters are determined by a linear fit of $z_i = z_0 + S_i^{xy}(dz/dS)$, where S_i^{xy} is the track length for the point z_i in the xy-projection. The angle θ is then given by the fitted value of dz/dS: $\theta = arctan(1/(dz/dS))$.

The above described version of the track finding program is very fast and running online during data taking for event classification and background suppression. It is efficient for tracks with $p_t \geq 100\ MeV$. At lower transverse momenta, the tracks are not well described by a helix any more due to multiple scattering.

All data is processed a second time offline. The track finding is repeated more thoroughly. The only information taken from the first approximative reconstruction are the long tracks. They can be used now to determine more exactly t_0, since a wrong t_0 leads to an offset of the track segments at the signal wire planes. Again, triples of hits are searched. But now they are not connected if they are sitting at the same place in the $\kappa - \phi$-plane, but if they have common wires. Chains of triples are first connected within the cells, then between neighbouring cells within a ring, and then between the rings. Chains are linked, if they are close in the κ-ϕ−plane. The linked track segments are fitted to a circle with a χ^2-fit. If there exist different hypothesis, the one with the lowest χ^2 is taken.

In a later stage, the tracks are extrapolated to the full drift chamber volume to search for unused hits belonging to the found tracks. They are picked up and the fit performed again. Very short tracks without hits in the first layers are rejected. The error matrix is derived from error propagation from the errors of the measured points.

Vertex Determination Using stiff tracks with small d_{ca} from several hundred events, the xy-position of the run-vertex is calculated. This run vertex is then used as a constraint when fitting the tracks again. A search for secondary vertices is made at this stage. The z-position of the primary vertex is determined event by event from a fit of tracks pointing in $r\phi$ to the run vertex.

2.2.4 Central Z-Chambers

The central inner and outer z-chambers CIZ and COZ complement the measurement of charged track momenta. Their z-resolution is 300 μm. For the final values of the track momenta, hits in the CIZ and COZ which can be linked to a track are included and a last fit performed. Since the linking efficiency is low, the z-chambers do not improve the detector performance considerably.

2.2.5 Multiwire Proportional Chambers

The center inner proportional chamber (CIP) and the center outer proportional chamber (COP) complement the central tracking system of the H1 detector. They have no impact on the final track measurement but provide very fast information for triggering. The CIP is located between CIZ and CJC1 (see fig. 2.3) and the COP between COZ and CJC2. The granularity is given by the design and is in ϕ-direction 16 and in z-direction 60 (CIP) and 18 (COP). Hits in CIP and COP are combined to "rays" which are used to determine the z-position of the primary vertex (see later).

2.2.6 Calorimetry

Liquid Argon Calorimeter (LAr) To obtain the needed high position and energy resolution, a highly segmented liquid argon calorimeter has been chosen. The inner, *electromagnetic* part of the calorimeter (ECAL) - which is designed to absorb the electromagnetic showers of photons and positrons/electrons - is composed of lead absorbers ($d = 2.4$ mm) and gaps filled with liquid argon ($d = 2.35$ mm). It has a thickness of 20 - 30 radiation lengths. For the outer part, the hadronic calorimeter (HCAL), the absorbers are made out of stainless steel ($d = 16\ mm$), the gaps have a thickness of $d = 4.8\ mm$. The nuclear interaction length of both sections together adds up to five to eight.

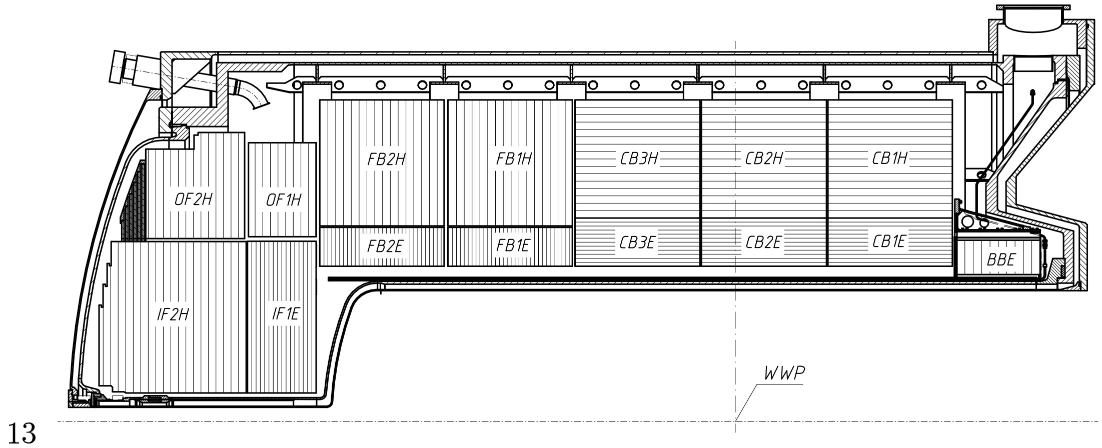

Figure 2.5: Side view of the liquid argon calorimeter.

The size of the readout pads is only $4 \times 4\ cm^2$ in the electromagnetic section and $8 \times 8\ cm^2$ in the hadronic section. The calorimeter is divided radially in 3-4 (ECAL) and 4-6 (HCAL) layers which leads to 45'000 channels in total (70 % are in the ECAL). The pad size in the ECAL corresponds to about 2 Molière radii and allows the separation of hadronic and electromagnetic showers depending on the lateral shower size. The high granularity allows also an excellent angular resolution.

The achieved energy resolution for electromagnetic showers is $\sigma_E/E = 11.5\%/\sqrt{E} \oplus 1\%$, with an uncertainty in the absolute scale of about 3%. For hadronic showers it is $\sigma_E/E = 51\%/\sqrt{E} \oplus 1.6\%$, as measured in test beams. The systematic uncertainty of the hadronic scale has been determined using the double angle method and the balance of transverse momentum to be 5%.

The very forward region ($0.7^\circ - 3.3^\circ$) of the H1 detector is covered by a silicon-copper sandwich calorimeter (PLUG). Before the backward region has been upgraded (shutdown 1994/1995), a lead-scintillator sandwich calorimeter (BEMC) (which was readout via wavelength shifters and silicon photodiodes) has been used. It's main application was the measurement of the positrons in DIS in an intermediate Q^2-range ($Q^2 < 100\ GeV^2$). With only about one hadronic interaction length, it was too thin to measure hadronic showers.

Spaghetti Calorimeter (SpaCal) The electromagnetic section of the SpaCal consists of scintillating fibers with a diameter of 0.5 mm embedded in a lead matrix. The lead to fiber ratio of 2.3:1 results in an energy resolution of $\sigma_E/E = 7.1\%/\sqrt{E/GeV} \oplus 1.0\%$. While the electromagnetic part is quite thick (27 radiation lengths), the hadronic section (lead to fiber ratio 4:1) is still thin due to the limited space available (total number of interaction lengths of both sections is 2.2). The energy resolution for hadrons is about $70\%/\sqrt{E} \oplus 20\%$ (for non leaking showers).

2.2.7 Trigger

To suppress background as fast as possible, H1 has five trigger levels which differ in input information, technology and decision time.

- **L1** The first level trigger needs 2.4 μs to decide if the event was useful. The decision relies on logical combination of quickly available detector signals, the "trigger elements" delivered by the subdetectors and the output of the decision are about 100 bits, the so-called trigger elements. Since 2.4 μs correspond to 25 bunch crossings, all data needs to be stored in pipelines for at least this time.

- **L2, L3** These trigger level had no influence for this analysis

- **L4** Level four uses a processor farm with high computing power to run a fast version of the reconstruction program to reconstruct tracks in the tracking devices and clusters in the calorimeters. The achieved reduction of the rate in L4 is of the order of 5:1. This level is also used, apart from event selection, to monitor detector components and to calculate preliminary calibration constants. Accepted events are written on tape with a rate of about 20 Hz.

- **L5** This last level runs offline. It performs the full reconstruction and sorts the events into several classes (for example DIS candidates, heavy quark event candidates etc.). All events which belong to at least one class are written to data summary tapes (DST) which are the starting point for physics analysis.

The most important trigger systems (for this analysis) delivering L1 trigger elements and the derived subtriggers are described below.

2.2.7.1 Drift Chamber Trigger

The drift chamber $r - \phi$ trigger ($DCR\phi$,[52]) uses the drift time information of 10 layers (out of 56) of the central jet chamber to search for tracks. The signals of these wires are digitised with a comparator and synchronized with the HERA clock and then serially clocked into a shift register. Hit masks are defined according to track position in drift space and track curvature in the magnetic field. 10^4 masks are applied in parallel to the output of the shift registers to mark active roads. The number of high momentum tracks is determined as well as the number and charge of tracks below 0.8 GeV. Since the masks do not fit to tracks with a d_{ca} larger than about 2 cm, background events are suppressed. The following trigger elements used in subtrigger 83, which is used in this analysis, are derived:

- DCRPh-TNeg: At least one negative track above 420 MeV.

- DCRPh-Tc: At least three tracks with p_T above 420 MeV

2.2.7.2 Z-Vertex Trigger

The z-vertex trigger [53] is entirely based on the signals of the multiwire proportional chambers CIP, COP and the first double layer of the forward proportional chambers FPC. It's aim is to reconstruct online the primary interaction vertex along the beam axis. This is realized by building "rays" out of the coincidence of four pad signals which can be connected by a straight line pointing to the z-axis. The z-axis is divided in bins and each ray is unambiguously assigned with one bin, so that each ray contributes with one entry to the so-called z-vertex histogram. The histogram bin with most entries is expected to contain the interaction vertex of the event. A total length of 88 cm around the nominal interaction point is covered by 16 bins with a size of 55 mm each. The following trigger elements are derived:

- zVtx-T0: At least one ray
- zVtx-mul>1: More than one entry in the z-vertex histogram
- zVtx-sig: Significant peak in the z-vertex histogram

2.2.7.3 Subtrigger 83 and 84

By simple logical combination, "subtriggers" are built out of the trigger elements. There exist in total more than hundred subtriggers. Two of them are used in this analysis:

- **Subtrigger 83:** The idea is to trigger on a positron in the e-tagger at -33 m in coincidence with a reconstruced z-vertex and some tracks in the CJC. No signals of beam induced background should be observed by the veto detectors. A typical combination is therefore
  $st83 = eTAG + zVtx{-}T0 + DCRPh{-}TNeg + (FToF{-}IA||!FToF{-}BG)$, where "+" is a logical AND, "!" a NOT and "||" stands for the OR. The trigger elements which have not been already explained are:
  - *eTAG:* Reconstructed positron in the e-tagger at -33 m.
  - *FToF-IA,FToF-BG*: Signals in the forward (F) time of flight system (TOF) in the interaction (IA) time window or the background (BG) time window.
- **Subtrigger 84:** Is similar to subtrigger 83, but with a reconstructed positron in the e-tagger at -44 m.

Chapter 3

Single Inclusive $D^{*\pm}$ Spectra and Energy Flow

3.1 Single Inclusive $D^{*\pm}$ Spectra

In this section a measurement of the photoproduction cross section of $D^{*\pm}$-mesons in the visible range $-1.5 \leq \eta(D^*) \leq 1.5$ and $p_t(D^*) \geq 2$ (2.5) GeV is presented. The accessible range in the rapidity η [1] is given by the acceptance of the central jet chamber, whereas the cut on the transverse momentum p_t of the D^* reduces the combinatorial background. Using both positron detectors at -33 and -44 m, two independent samples covering different ranges of the photon-proton center of momentum energy are analysed.

Previous measurements [18, 54] left open the question (due to a lack of statistics) if the massive scheme NLO QCD calculation (see chapter 1) with a phenomenological fragmentation function is really the appropriate description for D-meson photoproduction in the visible kinematical range at HERA. Since the determination of the gluon density will be based on this "standard" approach, it is essential to check it's validity.

Single inclusive $D^{*\pm}$ spectra provide a good testing ground, because the experimental uncertainties are small and mainly of statistical nature (the measurement of the differential cross sections itself is nearly independent on theoretical assumptions since no extrapolation is needed). On the theoretical side, the dependence of the QCD calculation on the involved scales is comparatively small in the visible phase space and higher order corrections therefore expected to be well under control. Also the form and parameter of the fragmentation function are well known from fits to e^+e^--data.

$D^{*\pm}$-mesons are identified by explicit reconstruction of the exclusive decay channel $D^{*\pm} \to D^0\pi^+ \to K^-\pi^+\pi^+$. The data collected by the H1 collaboration in the years 1994 to 1996 is analysed.

[1] $\eta = 0.5\ \ln\frac{E+p_z}{E-p_z}$. The rapidity can be approximated for small masses by the pseudo-rapidity $\tilde{\eta} = 0.5\ \ln\frac{p+p_z}{p-p_z} = arctgh(\frac{p_z}{p}) = -\ln\tan(\frac{\theta}{2})$.

3.1.1 D^*-Tagging

The mass difference between the $D^{*\pm}$ and the D^0-meson ($\Delta m = 145.42 \pm 0.05\ MeV$) [2] is slightly larger than the mass of a charged pion. The strong decay $D^* \rightarrow D^0 + \pi$ (branching ratio $68.3\% \pm 1.4\%$) has accordingly a small Q-value ($Q = \Delta m - m_\pi = 5.85\ MeV$) with respect to the masses of the decay products, which means that the pion and the D^0 are produced nearly at rest in the D^* system ($p^* = 39\ MeV$). In the laboratory system, where the D^* is boosted, the momenta of the pion and the D^0 appear highly correlated: $\vec{p}_\pi \approx \frac{1}{13}\vec{p}_{D^0}$. Due to this kinematic constraint, the allowed momentum space for combinatorial background is small. Therefore it is advantageous to reconstruct the mass difference of the D^* and the D^0 in the decay $D^* \rightarrow D^0\pi$ to get rid of the highly abundant combinatorial light quark background (D^*-tagging, [55]). The pion is often called soft or slow (π_s). Moreover, by taking the difference of two reconstructed masses, systematic errors in the track measurement cancel out and the resolution for the mass difference is much better than the resolution for the D^* and D^0 masses (roughly a factor of 25). I use the decay channel $D^0 \rightarrow K^-\pi^+$ of the D^0 with a branching ratio of $3.83\% \pm 0.12\%$. This large branching fraction and the fact that it is only a 2-body decay make the $K^-\pi^+$-channel especially attractive.

Every charged track in the CJC is assumed once to be a pion and once to be a kaon. Then all possible pairs of a K and a π (with opposite charge) are built and the mass of the pair calculated, using the measured momentum and the corresponding mass hypothesis. This gives a distribution of the mass of the D^0 candidates. Only pairs around the nominal D^0 are used for the further selection. All remaining tracks are assumed to be candidates for the slow pion. Again, the measured momentum is completed to a 4-vector with a π mass hypothesis, and the sum of the 4-momenta of the three tracks is the D^* candidate. Both π candidates are requested to have the opposite sign of the K candidate. The presence of D^*-mesons reflects in a narrow peak in the Δm distribution around $0.145\ MeV$.

3.1.2 Determination of the Observed Number of D^*

3.1.2.1 Event Selection

I consider e^+p-data at the nominal beam energy of around $27.5\ GeV \times 820\ GeV$ and runs where the relevant subdetectors - luminosity system, central jet chamber, proportional chambers (CIP/COP/FPC), veto counters and calorimeters (BEMC/Spacal, LAR) - have been fully operational. Additionally, a selection of run ranges with stable trigger conditions is applied. A list of the allowed/rejected run ranges for subtrigger 83 is given in table 6.1 in the appendix.

Two independent data samples are analysed: One where the scattered positron is measured in the e-tagger at -44 m, and one with the electron found in the e-tagger at -33 m. They correspond to the subtriggers 83 and 84 (see page 30). The acceptance

[2] All numbers on particle properties are taken from [34].

device	range in y	$\overline{y}$	$\overline{W_{\gamma p}}$	photon flux
e-tagger at -33 m	0.29 - 0.62	0.420	194	$1.284 \cdot 10^{-2}$
e-etagger at -44 m	0.02 - 0.32	0.092	88	$8.38 \cdot 10^{-2}$

Table 3.1: Acceptance of the small angle positron detectors. $\overline{W_{\gamma p}}$ and the photon flux are calculated as described on pages 6 and 24.

of both taggers is shown in fig. 3.1. The average values of y and $E_{\gamma p}$ are shown in table 3.1.2.1

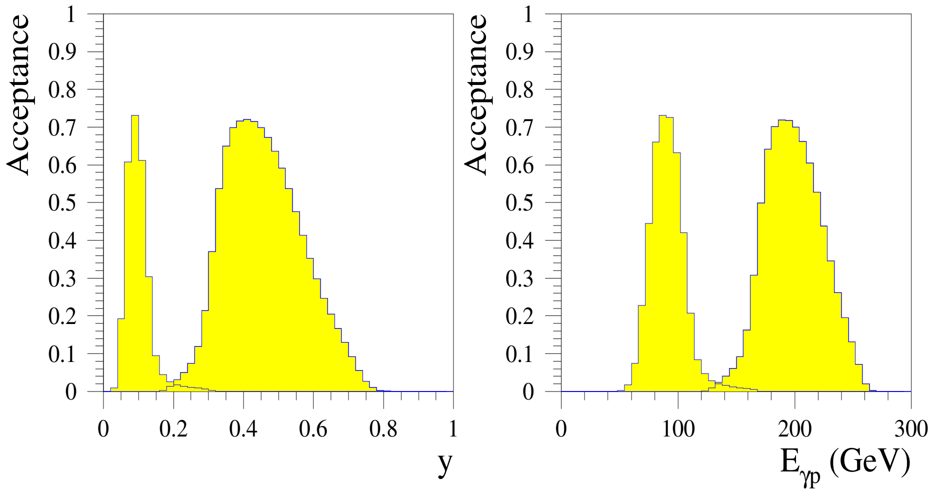

Figure 3.1: Acceptance in y and $E_{\gamma p}$ of the electron taggers. The left peak corresponds (in both diagrams) to the acceptance of the device at 44 m, the peak on the right side to the e-tagger at 33 m.

3.1.2.2 Track Selection

For the reconstruction of the D^* mesons, tracks measured in the central jet chamber are used. The following conditions were applied for a track to be a candidate for a π or a K:

- track must be successfully fitted to the primary vertex
- distance of closest approach of the track to the primary vertex (in the $r\phi$-plane) must be less than 2.0 cm

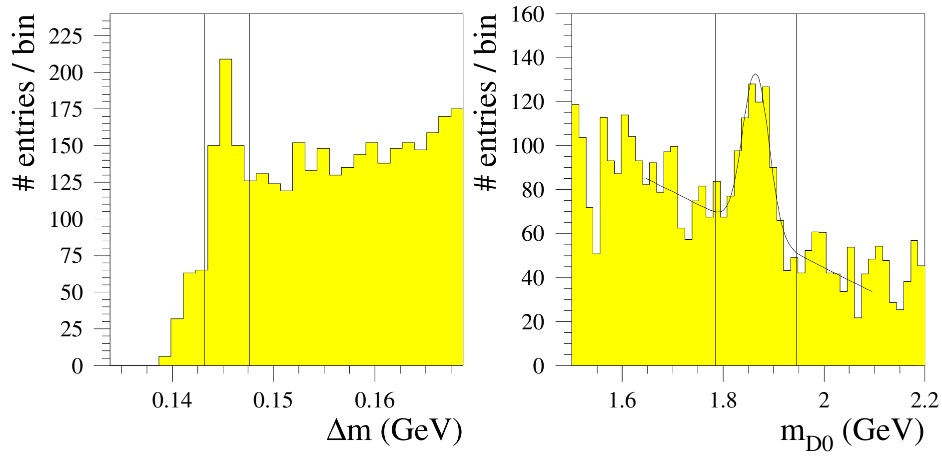

Figure 3.2: Mass difference $\Delta m = M(K\pi\pi) - M(K\pi)$ (left histogram) and D^0-mass (right histogram) for the data sample of subtrigger 83 after all selection cuts described in the text.

- track must be seen in the CJC 1 (distance of the closest wire with a hit to the z axis less than 50.0 cm)
- $20^\circ \leq \theta \leq 160^\circ$
- radial track length at least 10.0 cm for tracks within $30^\circ \leq \theta \leq 150^\circ$ and 5.0 cm for all other tracks
- $p_t \geq 150\ MeV$

3.1.2.3 Determination of the Number of D^*: Data Sample from ST 83

In order to reduce the background, it is advantageous to use the fact that the daughter particles of the D^0 have a harder p_t spectrum than the particles from light quark photoproduction. A cut of 500 MeV on the p_t of the π and the K candidate is applied for this purpose. Fig. 3.2 shows the ΔM distribution for D^*-candidates satisfying all the above mentioned selection criteria and having a D^0 mass within a window of 80 MeV around the nominal mass of $1864.5 \pm 0.5\ MeV$. A clear signal is visible with a width of $\sigma = 1.08 \pm 0.16\ MeV$ [3] centered at $145.41 \pm 0.17\ MeV$, in agreement with the value given by the particle data group ($145.42 \pm 0.05\ MeV$). To

[3] The given values for position and width of the peak are from the fit according to the method of the equivalent number of events which is described below.

justify the width of the D^0 mass window of 80 MeV, the D^0 mass distribution for candidates with a ΔM in a range $\pm 2\sigma$ around the measured peak position is shown. Also here, a significant peak at 1864.8 ± 2.4 MeV with a width of 25.7 ± 2.4 MeV is observed, showing that the chosen mass window is wide enough ($> 3\sigma$) to ensure full efficiency of this selection cut.

3.1.2.4 Background

The dominant contribution to the background in fig. 3.2 originates from the photoproduction of light quarks and gluons, simply because the total photoproduction cross section at 200 GeV is $165 \pm 2(stat.) \pm 11(syst.)$ [56], two orders of magnitude higher than the total charm cross section [18]. The shape of the background has a typical threshold behaviour and can be approximated by the phase space volume:

$$\frac{dN}{d(\Delta m)} = a(\Delta m - m_\pi)^2. \tag{3.1}$$

The closer the distance to the threshold, the better the approximation gets. To obtain a good description of the background up to $\Delta m = 0.17$ GeV it is necessary to fit the exponent together with the amplitude (typical values are 0.3 to 0.4).

Charm quark decays add roughly ten percent background, as can be deduced from a comparison of fig. 3.3 and fig. 3.2. For fig. 3.3 the same selection cuts as used in the analysis were applied to a sample of $c\bar{c}$-Monte Carlo events, generated by AROMA [57]. The shape of the $c\bar{c}$-background is well described by a function of the form $(\Delta m - m_\pi)^{0.3}$, a function very similar to what fits best the total background.

From the left histogram, where the exactly known 3-momenta of the generated particles are combined to a Δm, in exactly the same way as the 3-momenta of reconstructed tracks, it can be inferred that there are no reflections from other decay channels which could not be absorbed into the usual background function. The S_0 is irrelevant for this analysis [58].

Background from decays of b-hadrons is negligible due to the small b cross section at HERA energies [7].

The Method of the Equivalent Number of Events The acceptance of the electron tagger at -33 m does not depend on the properties of the event, but is a function of y only. Since we deal with a small number of events, it is preferable to account for acceptance of the tagger by weighting each event with the inverse of the acceptance. For the e-tagger at -33 m, this procedure is possible because the energy of the scattered electron is measured with good precision ($13\%/\sqrt{E} \pm 1\%$) and the acceptance consequently well known. To limit the weights to values below or equal to 5.0, only events in the restricted range $0.29 \leq y \leq 0.62$ are analysed. The error on the weighted number of events

$$\tilde{N} = \sum_{i=1}^{N} \frac{1}{\epsilon_{ET,i}} \tag{3.2}$$

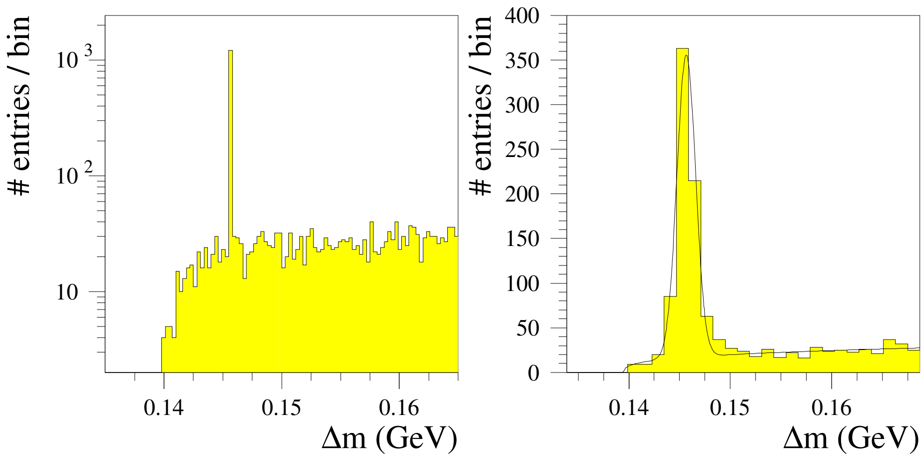

Figure 3.3: Δm-distribution of a MC sample generated by AROMA. Left histogram: Generated particles. Right histogram: Reconstructed tracks.

is given by

$$\sigma^2_{\tilde{N}} = \sum_{i=1}^{N} \left\{ (\frac{1}{\epsilon_{ET,i}})^2 + \sigma^2(\frac{1}{\epsilon_{ET,i}}) \right\}, \tag{3.3}$$

where the first term represents the purely statistical error and the second term the error introduced by the error in the measurement of the weight. Summing up the data from the three years 1994 to 1996 gives enough statistics to divide the visible range in η $(-1.5 \leq \eta \leq 1.5)$ into six bins and in p_t $(\geq 2.5\ GeV)$ into four bins. Because the underlying statistics is neither gaussian (too small number of events) nor Poissonian (since the events have weights) [58], a straightforward fit would yield unreliable results for the bins with a small number of entries. A statistically correct method for any number of events is the "method of the equivalent number of events" [59]: Given a certain number of weighted events $\tilde{N}$, we define the equivalent number of events N' by

$$N' = \frac{(\sum_{i=1}^{N} 1/\epsilon_i)^2}{\sum_{i=1}^{N} (1/\epsilon_i)^2} \tag{3.4}$$

which has the nice property that

$$\sigma(N') = \sqrt{N'}. \tag{3.5}$$

For a given Δm-distribution this means, that every bin j, which contains a certain weighted number of events $\tilde{N}_j$, has to be scaled with a factor $N'_j/\tilde{N}_j$, and then a maximum likelihood fit can be made. After the fit is performed, the parameters of the fit have to be scaled with an average scale factor

$$\frac{\sum_{j=1}^{N_{bin}} \tilde{N}_j / N'_j}{N_{bin}}. \tag{3.6}$$

This scale factor does not depend on the choice of the sample of bins with which the average is calculated, since the scale factor is in principle independent of the number of entries in the bins. The only complication could be that different ranges in the histogram have different average weights. It has been checked that for the Δm-histogram with all the measured events from subtrigger 83 the scale factor is compatible with a constant value over the full range. To fit $N' - \Delta m$-distributions, the sum of a gaussian and a root function has been used:

$$f(\Delta m) = a(\Delta m - m_\pi)^b + c\, e^{\frac{(\Delta m - \Delta m_0)^2}{2\sigma^2}}. \tag{3.7}$$

Fig. 3.4 shows the $N' - \Delta m$-distributions for the different bins in p_t, the first histogram being the total signal in the range $p_t \geq 2.5\ GeV$ and $-1.5 \leq \eta \leq 1.5$. Since the background is quite high, a simultaneous fit of all the parameters is unstable. I prefer to fit only the parameters a, b and c for the different bins in η and p_t, and take fixed values for position and width of the peak. The values of the position and width are determined from a 5-parameter fit of the full signal and are $\sigma = 1.08 \pm 0.16\ MeV$ and $145.41 \pm 0.17\ MeV$. The dependence of the width has been measured with the data sample from the second e-tagger (-44 m), which provides a better signal to background ratio to be

p_t	$2-3\ GeV$	$3-4\ GeV$	$4-6\ GeV$	$6-10\ GeV$
data	$1.1 \pm 0.15\ MeV$	$1.02 \pm 0.2\ MeV$	$0.97 \pm 0.2\ MeV$	
MC	$0.80 \pm 0.01\ MeV$	$0.76 \pm 0.02\ MeV$	$0.78 \pm 0.04\ MeV$	$0.81 \pm 0.04\ MeV$

A dependence on p_t of the order of ten percent is observed, the change of N' under variation of σ of ten percent is therefore added quadratically to the statistical error. The MC indicates that in the bin above 6 GeV, where no conclusion from data can be made, no change in the width is expected. For the variable η, the table looks as follows (all values in MeV):

	$-1.5 - -1$	$-1 - -0.5$	$-0.5 - 0$	$0 - 0.5$	$0.5 - 1$	$1 - 1.5$
data	-	-	0.86 ± 0.17	1.12 ± 0.18	0.89 ± 0.16	-
MC	1.03 ± 0.04	0.83 ± 0.02	0.77 ± 0.02	0.77 ± 0.02	0.83 ± 0.04	1.00 ± 0.06

The errors on the fit parameters of the data are not small enough to allow a conclusion to be made. Statistical fluctuations are dominating. A closer inspection of the MC results yields that on the edge of the acceptance it sometimes happens that a track does not cross CJC 2 which leads to a 20% worse resolution in the first and last bin than in the central region. Since it is preferable for the η-distribution to fix the width to stabilize the fit, too, I account for the larger width in the outmost bins by adding an error which is obtained by varying the width by 20% instead of 10% as in the case of the central region. The N'- and $\tilde{N}$-histograms of the different bins in η are shown in figs. 3.6 and 3.7. In the following table, the measured number of events is given, where the error is determined from the errors on the fit parameters plus the contribution from varying the width as described:

p_t (GeV)	≥ 2.5		$2.5-3.5$	$3.5-4.6$	$4.5-6.5$	$6.5-10.5$
$\tilde{N} \pm \sigma(\tilde{N})$	489 ± 92		257 ± 59	134 ± 32	65 ± 20	29 ± 10
η	$-1.5--1$	$-1--0.5$	$-0.5-0$	$0-0.5$	$0.5-1$	$1-1.5$
$\tilde{N} \pm \sigma(\tilde{N})$	73 ± 20	115 ± 26	106 ± 29	91 ± 28	63 ± 28	34 ± 22

In a previous analysis, the wrong sign background ($D^{*\pm} \rightarrow \pi_s^{\pm}\pi^{\mp}K^{\mp}$) has been fitted simultaneously. To save disk space, wrong sign combinations have not been stored any more for the 1995 and 1996 data. Those wrong sign combinations which are found in the stored data have survived the L4 and L5 selection because they

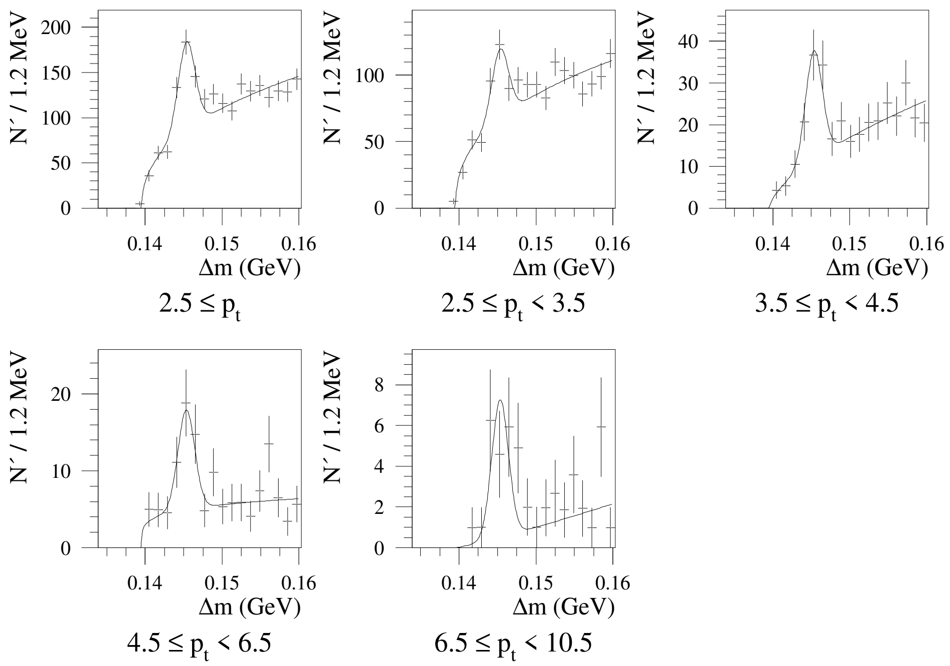

Figure 3.4: Data sample of subtrigger 83 (e-tagger at -33 m). Shown are the Δm-histograms of the equivalent number of events (N') in bins of p_t. The first histogram contains the total signal. These are the histograms which are fitted.

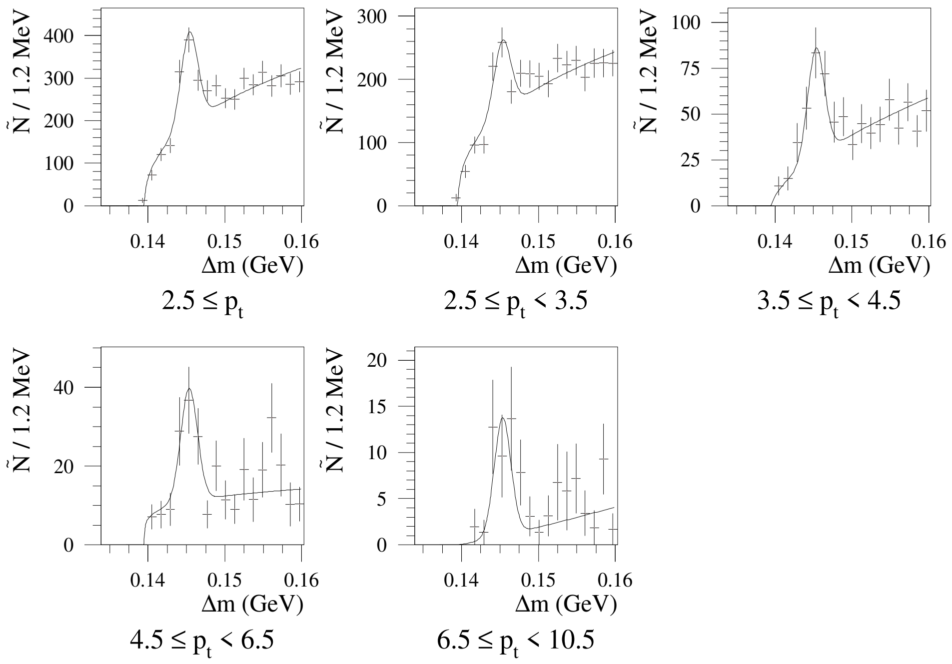

Figure 3.5: Data sample of subtrigger 83. Δm-histograms of $\tilde{N}$ in bins of p_t.

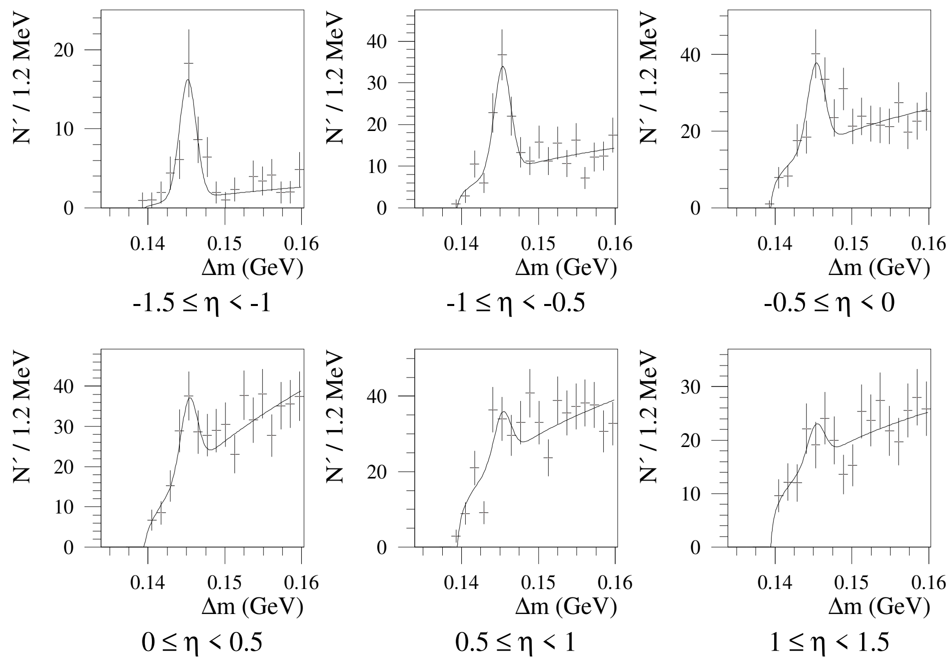

Figure 3.6: Data sample of subtrigger 83. Δm-histograms of N' in bins of η.

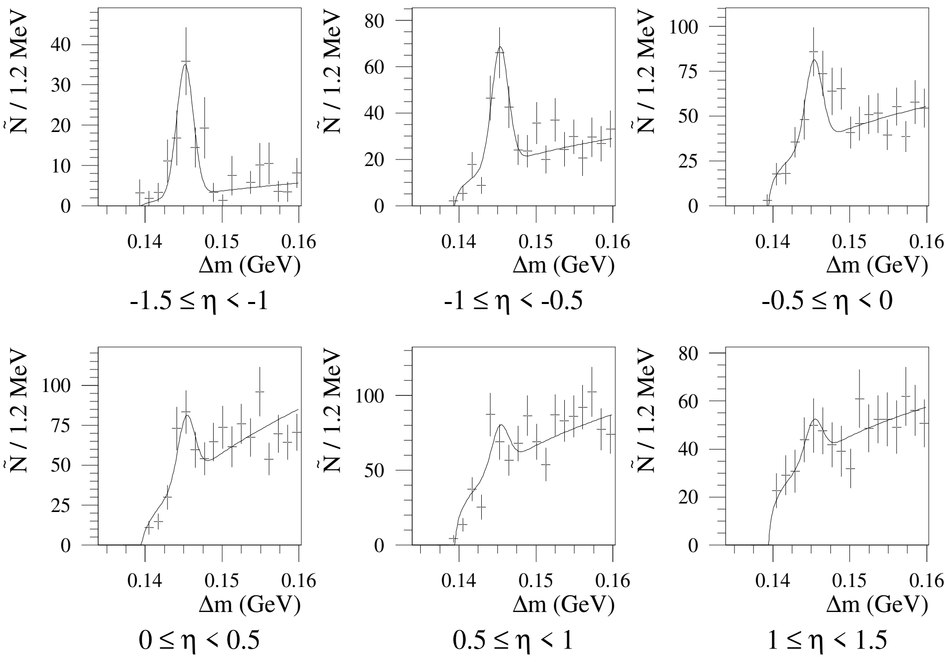

Figure 3.7: Data sample subtrigger 83. Δm-histograms of $\tilde{N}$ in bins of η.

belong also to another interesting category of events (they contain for example muon candidates, high p_t jets etc.), and this sample is therefore biased, thus the shape of the Δm-distribution is not expected to be the same as for the combinations of correct sign.

Another method to determine the number of D^* in the peak is to fit only the background and to *count* how many events there are in the peak above the background. This method has the drawback, that information on the shape of the signal is not used (leading to a larger statistical error) and that an arbitrary number of bins (five in this case) has to be chosen for the counting.

Yet another method is to perform a χ^2-fit of the $\tilde{N}$-histogram. The results of these different methods are compared in Fig. 3.8 to the number of events obtained using the standard method. The differences give an estimate of the systematic error. The results for the total signal are compiled in the table 3.2, adding also the results from simultaneous fits to the wrong sign background (which should be taken with the grain of salt mentioned above). The results agree within the errors. It seems that counting gives results which are five to seven percent below the results from fitting. The difference between the numbers obtained are a measure for the systematic error. Systematic deviations of the chosen fit-function and the signal or the background would show up here.

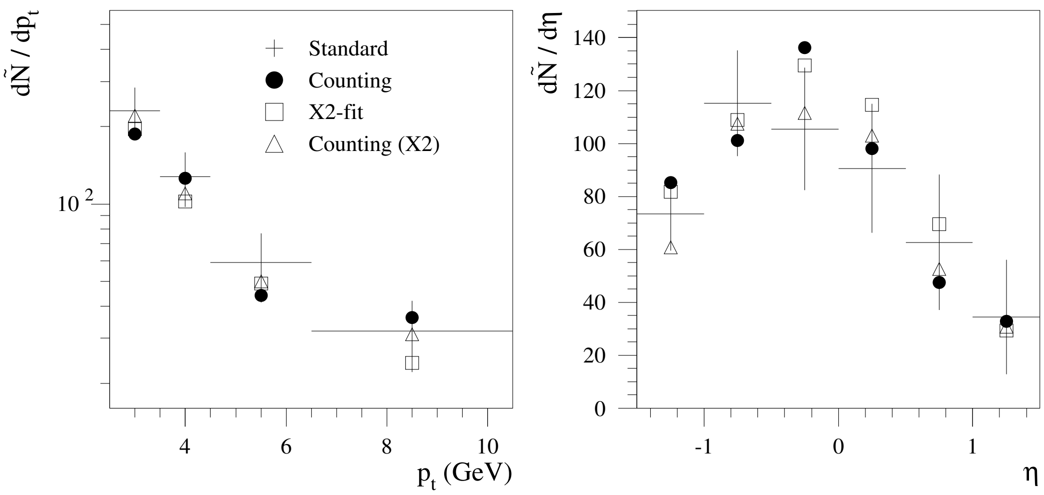

Figure 3.8: Comparison of the results of different methods to determine the number of events. 'Standard' means the method of the equivalent number of events, "Counting" stands for counting the entries above the fitted background in the five signal bins, "X2" is a χ^2-fit and "Counting (X2)" means that the background was determined using the χ^2-fit.

Method	Total number of events
Standard method	489 ±92
χ^2-fit	485 ±72
Counting (background from standard fit)	466 ±98
Counting (background from χ^2-fit)	455 ±96
Simultaneous standard fit of signal and background	488 ±92
Simultaneous χ^2-fit of signal and background	488 ±69

Table 3.2: Total number of events ($\tilde{N}$) in the data sample of the subtrigger 83 in the visible range $-1.5 \leq \eta \leq 1.5$ and $2.5 \leq p_t$ as determined with different methods.

3.1.2.5 Determination of the Number of D^*: Data Sample of ST 84

Fig. 3.9 shows the Δm - histogram of the unweighted events of subtrigger 84 whereas only the two following cuts have been changed with respect to the st 83 data sample:

- $p_t(D^*) \geq 2.0\ GeV$
- $p_t(K,\pi) \geq 350\ MeV$.

Thanks to the lower $\gamma - p$ center of momentum energy, the combinatorial background is smaller and a lower p_t cut than for subtrigger 83 can be applied. A clear signal is visible. Again, the D^0 mass peak is shown for candidates with a Δm closer than 2.5 σ to the center of the peak. Also here, the chosen D^0 mass window of 80 MeV is clearly wide enough ($> 3\sigma$).

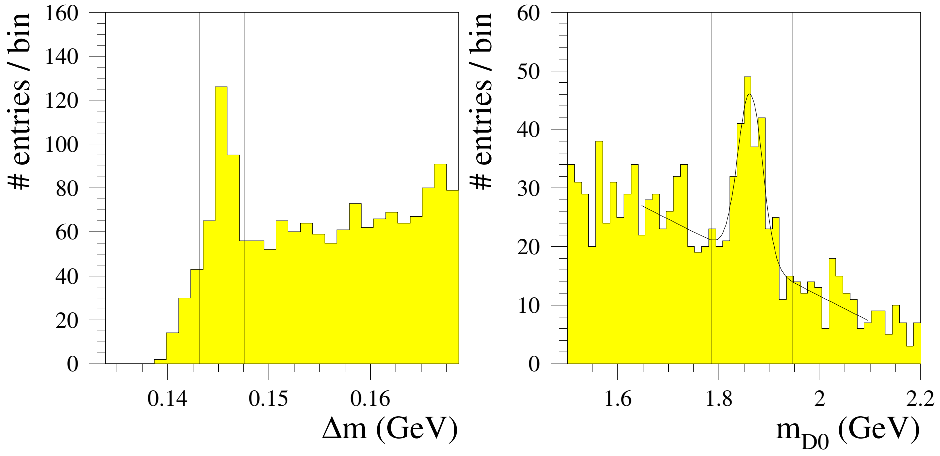

Figure 3.9: Mass difference $\Delta m = M(K\pi\pi) - M(K\pi)$ (left histogram) and D^0-mass (right histogram) for the data sample of subtrigger 84 after all selection cuts described in the text.

The event and track selection is the same as for subtrigger 83, but a different run selection needs to be applied which is listed in table 6.2 in the appendix. The run selection for 1995 ist taken from [54].

As explained in the detector chapter, the e-tagger at -44 m is hit usually right on the edge of the crystal, resulting in a very poor energy measurement. It is therefore impossible to weight every event with the inverse of the acceptance as it was done for the subtrigger 83. The measured average weight of 5.56 will be used later on to calculate the cross section. When comparing the measured cross section

p_t (GeV)	≥ 2.0		$2.0-3.0$	$3.0-4.0$	$4.0-6.0$	$6.0-10.0$
$\tilde{N} \pm \sigma(\tilde{N})$	299 ± 75		146 ± 38	87 ± 22	39 ± 30	10 ± 4.5
η	$-1.5 - -1$	$-1 - -0.5$	$-0.5 - 0$	$0 - 0.5$	$0.5 - 1$	$1 - 1.5$
$\tilde{N} \pm \sigma(\tilde{N})$	5.2 ± 3.7	2.5 ± 2.5	46 ± 14	113 ± 28	108 ± 28	20 ± 15

Table 3.3: Measured number of D^*-mesons for the data sample of subtrigger 84 (e-tagger at -44 m).

with calculations, one has to keep in mind this approximation. A correct way to proceed is to use an acceptance-weighted Weizsäcker-Williams photon flux in the QCD calculation.

Because of the strongly changing beam background conditions, subtrigger 84 received a prescale factor of 1 to 99. Such a varying prescale factor is clearly a source of an event weight which has to be treated like the weight from the tagger acceptance in the subtrigger 83 data sample (if one has to deal with a small number of events). In order to avoid very high event weights, only runs with a prescale of less than five are considered [4].

Figures 3.10 to 3.13 show the corresponding N' and $\tilde{N}$ histograms for subtrigger 84. The procedure to obtain the number of events is similar to the previous case: The position and width of the peak has been fixed to the values obtained with a fit to the whole st 84 data sample. Then a 3-parameter (amplitude of peak and background and exponent of the background) log-likelihood fit of the histogram of the equivalent number of events with the function 3.7 is performed. The fit parameters are scaled according to equation 3.6. There are obviously three histograms with too few entries for a fit: The first two bins in eta and the last bin in pt. In these cases, the number of events is determined by counting the number of entries in the five closest bins to the nominal peak center, the background beeing estimated by assuming a constant background over the whole Δm-range. Table 3.3 list the reconstructed number of events.

[4]This has been taken into account in the calculation of the luminosity.

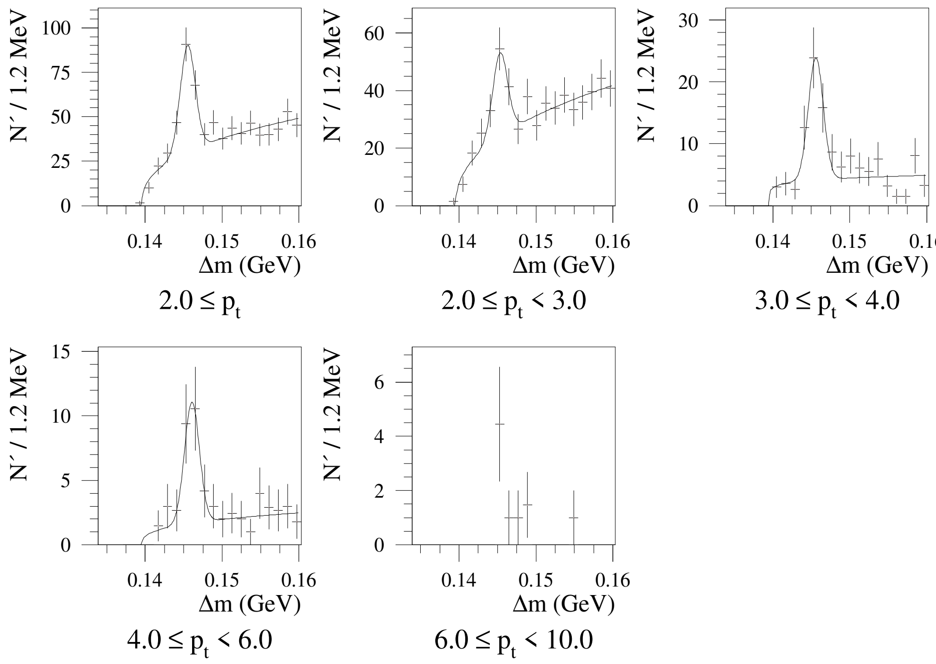

Figure 3.10: Data sample of subtrigger 84. Δm-histograms of N' in bins of p_t.

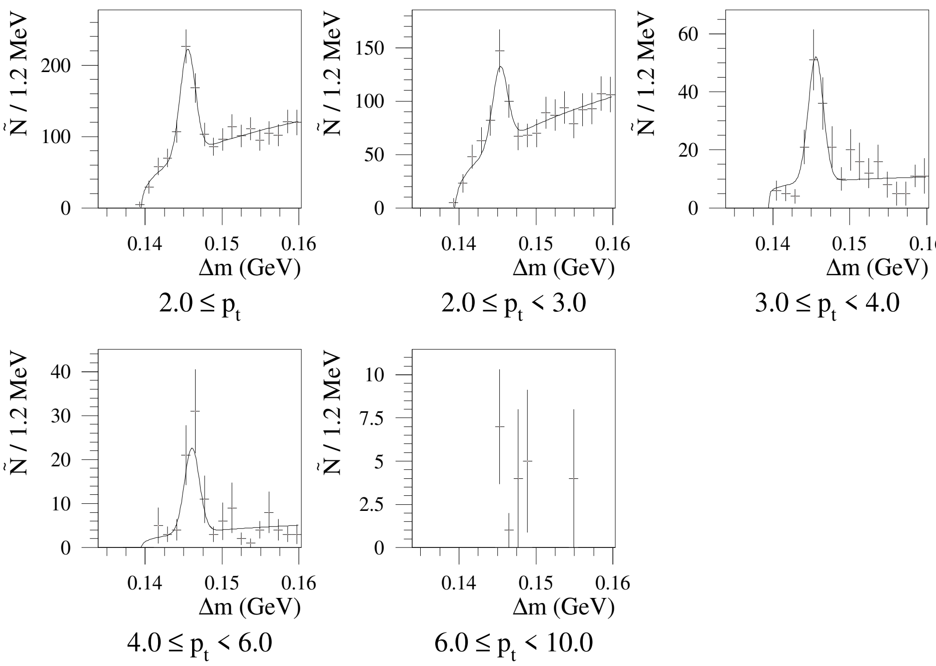

Figure 3.11: Data sample of subtrigger 84. Δm-histograms of $\tilde{N}$ in bins of p_t.

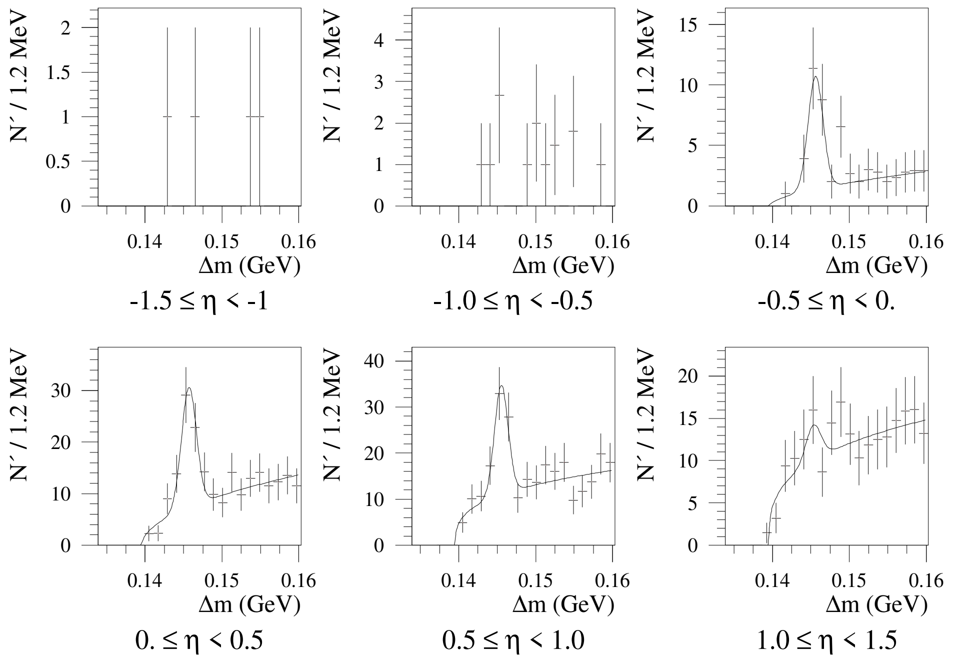

Figure 3.12: Data sample of subtrigger 84. Δm-histograms of N' in bins of η.

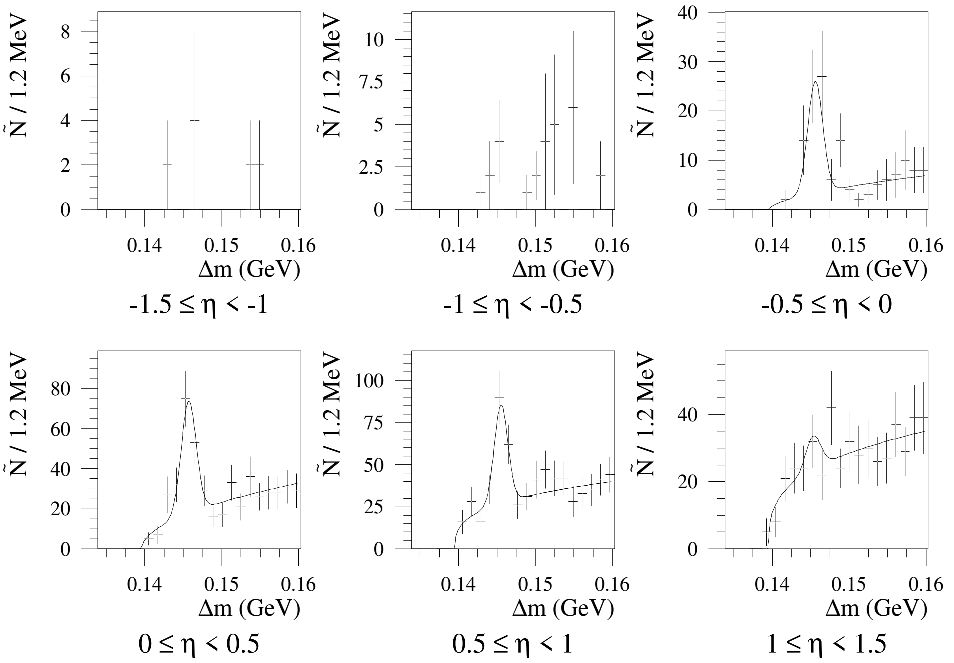

Figure 3.13: Data sample of subtrigger 84. Δm-histograms of $\tilde{N}$ in bins of η.

3.1.3 Efficiency

The number of D^* which are seen are only a fraction of these mesons which have really been produced in the visible range $-1.5 \leq \eta \leq 1.5$ and $p_t \geq 2.0\ (2.5)\ GeV$. A significant part of the D^* are lost due to one of the following reasons:

- The event has not been triggered (*trigger efficiency*).
- The event has been rejected because the trigger element has been prescaled.
- One or more daughter particles of the D^* did not enter the CJC or did not fulfill one of the applied cuts (e.g. the transverse momentum is too small).
- All the three daughter particles enter the CJC but at least one of them is not reconstructed.

While the prescale is already taken into account in the determination of the luminosity (for subtrigger 83) or by the event weights (subtrigger 84), the trigger efficiency and the two last reasons for losses which are summarized as *reconstruction efficiency* still need to be determined.

3.1.3.1 Trigger Efficiency

Subtrigger 83 Subtrigger 83 had a different composition of trigger elements in the three years. Moreover, it had to be changed even during every year several times to fight changing beam background conditions. But the main elements have always been the same:

- A positron found in the e-tagger at -33 m ("etag")
- At least one ray from the z-vertex trigger ("zVtx-T0"), 1996 a significant peak in the z-vertex histogram ("zVtx-sig")
- At least one track above a certain threshold in p_t reconstructed in the central jet chamber ("DCRϕ-T0,DCRϕ-Tc")
- No signals of background given by the veto detectors

The efficiency of the electron taggers is absorbed in the acceptance and does not need to be determined here.

There are a priori two possibilities to calculate the efficiency of a certain subtrigger.

The first one uses real ep data and requires the existence of an independent (parallel) subtrigger which triggers on the same class of events. Then one simply counts the fraction of events in the sample of the parallel trigger which have also been triggered by the subtrigger under investigation. This method can be extended and one can try to determine similarly the efficiency of the trigger elements which make up the interesting subtrigger. Unfortunately in our case this method can not be used

1994	(DCRPh-TNeg+eTAG)+(!ToF-BG)+(zVtx-T0)+(FToF-IA||!FToF-BG)
1995	(DCRPh-TNeg+eTAG)+(!BToF-BG)+(zVtx-T0)+(FToF-IA||!FToF-BG)
	(DCRPh-TNeg+zVtx-mul>1+eTAG)+(!BToF-BG)+(zVtx-T0)+ (FToF-IA||!FToF-BG)+(!SPCLe-AToF-Etot)
1996	(DCRPh-Tc+zVtx-sig+eTAG)+(!BToF-BG+!CIP-Backward)+(zVtx-T0)

Table 3.4: Trigger elements of subtrigger 83. The meaning of the trigger elements is explained in the detector chapter. A "+" stands for a logical AND, the "||" is an OR and the exclamation mark represents a logical NOT. Minor variations (especially of the veto elements) are not listed.

since it is based on the assumption that one starts with a (more or less) clean sample of events. For the present analysis, the number of D^* which have been triggered by subtrigger 83 is by far too small to allow a precise determination of the trigger efficiency in bins in η and p_t with charm events, moreover there is no parallel trigger with enough overlap. Nevertheless the method has been used in previous analysis [54], assuming that the event properties which are relevant for the trigger efficiency are the same for D^*-events and the light quark background, so the efficiency was determined using (mostly) background. As can be inferred from the Δm-histograms in the six bins in eta, the background has exactly the opposite behaviour than charm: It increases in forward direction. A second (relevant) difference between charm and background is the number of tracks per event: Charm events have a smaller multiplicity of charged tracks than the background as is well known (a cut on the number of tracks improves significantly the signal to background ratio in the Δm-histogram). Therefore this method can not be used.

The second way to determine the trigger efficiency is to use monte carlo simulations, assuming that the used event generator describes the relevant event characteristics correctly. The trigger part of the H1 detector simulation has been especially carefully tuned to describe the data as well as possible and can be reliably used for the determination of the trigger efficiencies. They are given in table 6.3 in the appendix. Since the composition of subtrigger 83 was different for every year, the efficiency needs to be calculated for every year separately and weighted with the luminosity of that year. A list of the trigger elements of st 83 is given in table 3.4. Moreover, the efficiency for the direct and the resolved part is not the same and one needs an assumption on the relative size of the direct and the resolved part in the different bins. I use the NLO QCD result from [14] with the following set of parameters:

- Monochromatic photon beam, $E_{\gamma p} = 194\ GeV$
- Parton density parametrizations: MRSA(P') [60] (proton) and GRV HO [61] (photon)

1995	(DCRPh-TNeg+(LU-ET-44+!LU-PD-low+!LU-WatVet))+ (!BToF-BG)+(DCRPh-T0)
1996	(DCRPh-TNeg+(LU-ET-44+!LU-PD-low+!LU-WatVet))+ (!BToF-BG)+(zVtx-T0)+(!SPCLe-AToF-E-1)
	(DCRPh-Tc+zVtx-sig+(LU-ET-44+!LU-PD-low+!LU-WatVet))+ (!BToF-BG+!CIP-Backward)+(zVtx-T0)+(FToF-IA||!FToF-BG)+ (!SPCLe-AToF-E-1)

Table 3.5: Trigger elements of subtrigger 84. Minor variations and settings with a small fraction of the total luminosity are not listed.

- $m_{charm} = 1.5\ GeV$
- Standard choice of μ_F, μ_R and μ_γ
- $\epsilon_{Peterson}$

For the direct part, the MC generator AROMA 2.2 [57] is used while the resolved part is simulated by PYTHIA 5.7 [62]. The obtained results are listed in table 6.3 in the appendix. A combination of the efficiencies in the different years taking into account the corresponding luminosities and the relative weights of the direct and resolved part is shown in 6.4, also in the appendix. The average trigger efficiency for the full data sample is $87.4\% \pm 1.2\%(stat)$. One systematic uncertainty stems from the question if the used MC generators correctly describe the topology of the events. The difference between AROMA and IJRAY-PYTHIA may therefore serve as an estimate of the size a potential error. Since this difference is about 5%, I use this number for the systematic error of the trigger efficiency. The second systematic error is given by the performance of the detector simulation.

Subtrigger 84 Subtrigger 84 is similar to the previous case, with the difference that the resolved contribution is expected to be tiny (see next section). All efficiencies are therefore calculated from a MC sample generated by AROMA. The trigger elements of subtrigger 84 are listed in table 3.5 and the efficiencies can be found in table 6.5 in the appendix. For the year 1996, where there are two different important compositions, both have been analysed and the results combined according to the relative luminosity.

3.1.3.2 Reconstruction Efficiency

Two effects which add up to the total reconstruction efficiency can be separated: First, the daughter particles of the D^* need to fulfill the selection cuts ($p_t(\pi_s) \geq 150\ MeV$, $p_t(\pi, K) \geq 500\ (350)\ MeV$, $20° \leq \theta_{track} \leq 160°$), and second, the tracks of the daughter particles must be reconstructed in the central jet chamber. Whereas the first part (A) is depending on kinematics only and expected to be well described in the monte carlo generator, the second part (B) depends crucially on a correct simulation of the response of the jet chamber to charged particles and needs to be carefully checked. The following table lists exemplary the two contributions to the full efficiency separately for subtrigger 83 and the year 1995 to give the reader a feeling for the absolute and relative size and importance of them. As can be inferred

	part A of the reconstruction efficiency	part B of the reconstruction efficiency
$-1.5 \leq \eta \leq -1.0$	48.9 ± 2.2	72.6 ± 3.0
$-1.0 \leq \eta \leq -0.5$	69.7 ± 1.8	79.8 ± 2.4
$-0.5 \leq \eta \leq 0.0$	74.1 ± 2.2	79.9 ± 3.0
$0.0 \leq \eta \leq 0.5$	74.8 ± 2.9	81.7 ± 3.9
$0.5 \leq \eta \leq 1.0$	74.2 ± 4.2	82.2 ± 5.6
$1.0 \leq \eta \leq 1.5$	54.1 ± 7.0	71.4 ± 9.3
$2.5 \leq p_t$	64.7 ± 1.0	78.4 ± 1.4
$2.5 \leq p_t \leq 3.5$	55.9 ± 1.4	76.2 ± 2.0
$3.5 \leq p_t \leq 4.5$	72.3 ± 2.1	79.9 ± 2.8
$4.5 \leq p_t \leq 6.5$	82.5 ± 2.6	83.3 ± 4.5
$6.5 \leq p_t \leq 10.5$	91.3 ± 4.3	76.4 ± 6.0

Table 3.6: The two contributions to the full efficiency for charm photoproduction. The MC generator AROMA 2.2 was used for part A and for part B it was combined with the H1 detector simulation (for the year 1996).

from this table, both contributions are of about the same size. Responsible for the inefficiencies are for (A) mainly the p_t cuts on the daughter particles of the D^* and for (B) the track selection cuts. On both ends of the acceptance in η, the efficiency drops significantly as expected.

To check the validity of the obtained numbers for the track reconstruction efficiency it is necessary to test if the detector simulation correctly describes the data.

Dead Drift Cells Because of detector problems, some drift cells have not been operational during certain periods. This causes inefficiencies at the corresponding positions in ϕ. Problems with single wires or drift cells are taken care of in the detector simulation by means of a "sick wire map" which is produced at the end of a run period using real data. Fig. 3.14 and 3.15 show the number of hits per track for tracks above 150 MeV in the CJC 1 and the CJC 2 for the years 1995 and 1996. Good agreement between detector simulation and data is found, except for the CJC2 in 1995. To reduce this problem, only tracks which start already in the CJC1 are used. For the year 1994 a similar check has been done in [58].

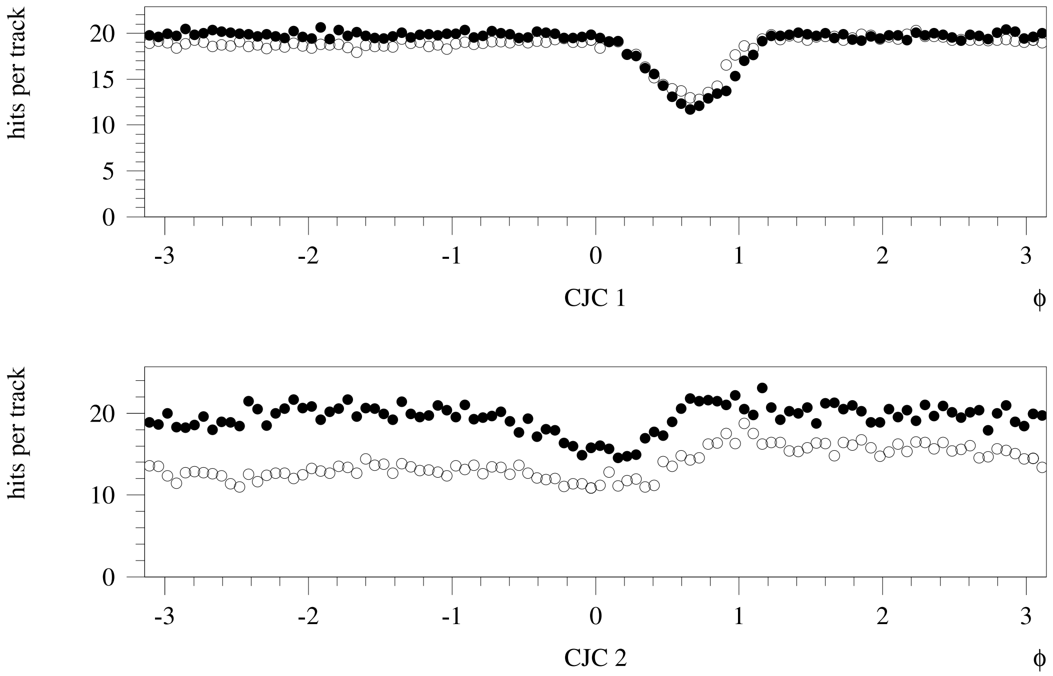

Figure 3.14: Average number of hits per track in the central jet chambers in 1995. Data: Open circles, MC: Filled circles.

Radial Track Length The radial track length is the difference of the radius of the last and the first measured hit of a track. In fig. 3.16 the distribution of the radial track length for data and MC events (AROMA 22 + detector simulation) are shown. Both distributions peak at 20 cm and 60 cm which corresponds to the radial thickness of the CJC 1 and CJC 1 plus CJC 2. Table 3.7 lists the efficiency of the cut on the radial track length ($L \geq 10\ cm$ for $30° \leq \theta \leq 150°$ and $L \geq 5\ cm$ else) for data and MC. Agreement within 2% for tracks above 150 MeV is found.

Distance of Closest Approach (d_{ca}) The d_{ca} distributions are shown in fig. 3.17. The cut on d_{ca} of two centimeters is applied to reduce the number of tracks from secondary vertices. Three effects are responsible for a non vanishing d_{ca}: First of all, not all the tracks originate from the primary vertex. Then a particle can change its direction because of multiple scattering in the material before or in the jet chamber. And finally the energy loss of low momentum particles changes the

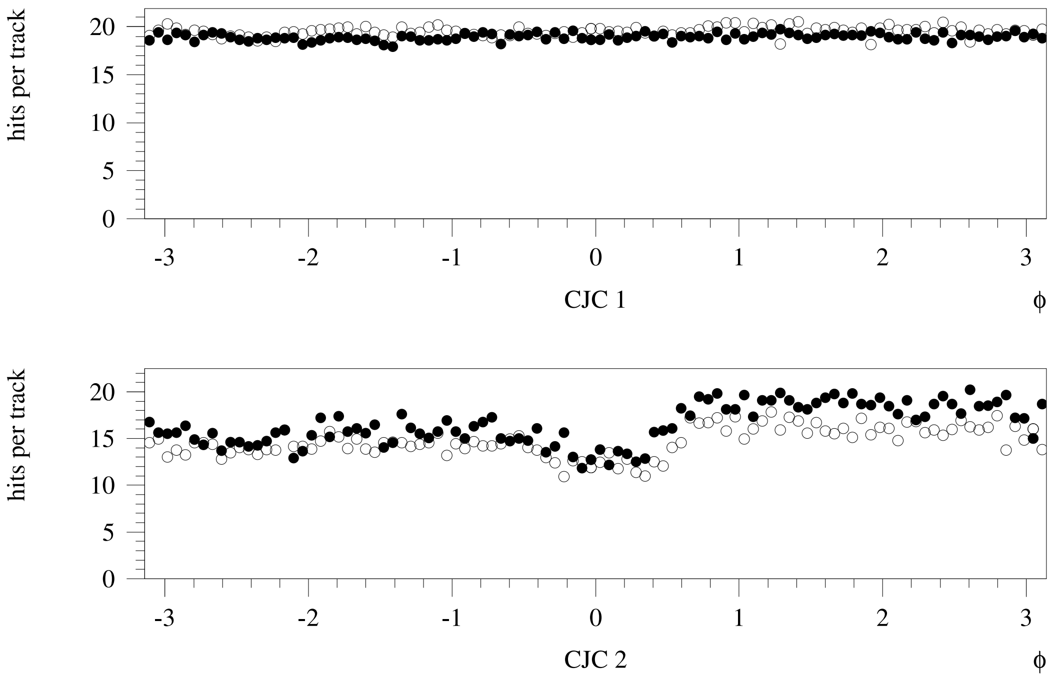

Figure 3.15: Average number of hits per track in the central jet chambers in 1996. Data: Open circles, MC: Filled circles.

curvature of the track so that the track parameterization with a constant curvature becomes insufficient. Fortunately for tracks above 150 MeV the two last effects are small and reliably described in the detector simulation. A quantitative comparison of the efficiency of the d_{ca} cut is listed in table 3.8. Good agreement of the MC with the data is found (within 2.5%).

Vertex Fit Efficiency To improve the momentum and direction resolution of the chamber, the run vertex is used in the track fit as a constraint.

The distance Δz from the z_0 of a track to the z-vertex position and the error on this quantity are a measure for the compatibility of a track with the event vertex and

p_t-range	H1 data	Monte Carlo
$0\ MeV \leq p_t \leq 150\ MeV$	25.8 %	22.4 %
$150\ MeV \leq p_t \leq 400\ MeV$	10.6 %	11.4 %
$400\ MeV \leq p_t \leq 800\ MeV$	6.4 %	6.2 %
$800\ MeV \leq p_t$	8.2 %	6.4 %

Table 3.7: Inefficiency of a cut on the radial track length as described in the text.

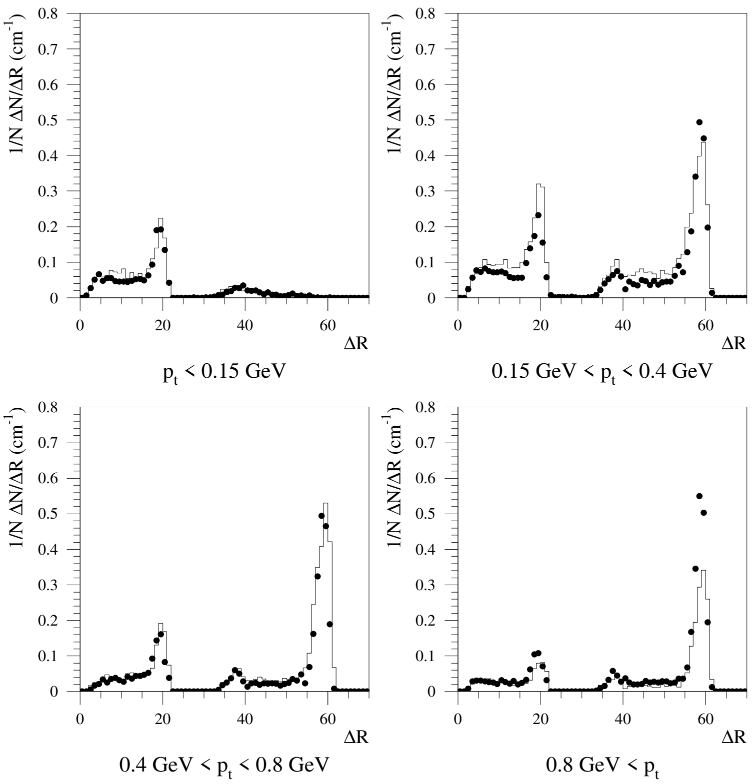

Figure 3.16: Distributions of the radial track length in data (dots) and MC (histogram) in different bins of p_T in the year 1996.

play therefore a significant role in the fit. If the fit converges depends crucially on the residual $\Delta a/\sigma(\Delta z)$. In fig. 3.18 this residual is shown for data and MC for a sample of tracks which point in $r\phi$ to the vertex ($d_{ca}/\sigma(d_{ca}) \leq 1$). The two distributions are not in very good agreement and the vertex fit efficiency can therefore not be reliably determined with MC. From a track in data it is principally never known if it originates from the primary vertex. The vertex fit efficiency for any sample of tracks from data is therefore always a lower limit for this efficiency. To get a good limit, one needs a sample with a very high number of tracks originating from the primary vertex. Such a sample can be obtained by requiring $|d_{ca}|/\sigma_{dca} \leq 1$ and a minimal track length of 10 cm as well as $p_t \geq 150\ MeV$, which yields a vertex fit efficiency of $98.0^{+1.5(syst)+0.5(stat)}_{-0.5(stat)}\%$. The effect of the secondary particles is estimated comparing monte carlo samples with and without any secondaries to be 0.5% percent, so that we end up with $98.5\% \pm 0.5\%(stat)$. Since a D^* has three daughters, the total vertex fit efficiency is therefore $95.6\% \pm 1.5\%$. The H1 detector simulation gives for this total vertex fit efficiency $99.5\% \pm 0.5\%$, so that the obtained value from data has to be included additionally to the reconstruction efficiency discussed below.

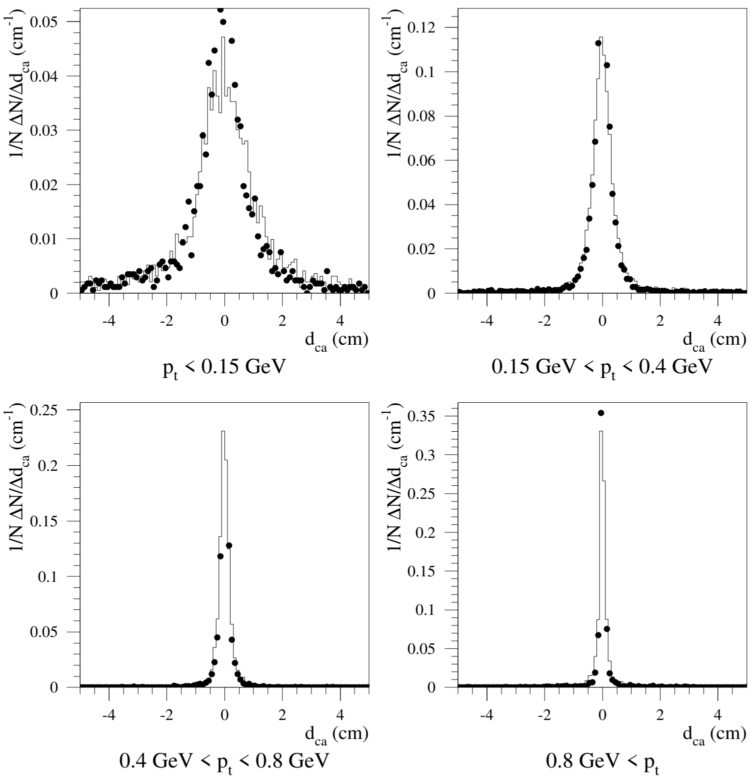

Figure 3.17: Distributions of d_{ca} in data (1996) and MC for different bins in p_T.

Reconstruction Efficiency The obtained numbers for the reconstruction efficiencies from MC are given in the tables 6.6-6.10 in the appendix. Like for the trigger efficiencies, the efficiency for the direct and the resolved part have been determined separately for the three years and both positron detectors and then weighted with the luminosity and the ratio direct/resolved. The final reconstruction efficiency for a D^* (including vertex fit efficiency and trigger efficiency) is $40.0 \pm 4.0\%$ for subtrigger 83 and 37.3 ± 2.8 for subtrigger 84, where the given errors are statistical errors only. The systematic error is estimated to be 2.5% per track, which is the typical precision with which the MC describes the efficiencies of the cuts in d_{ca} and the radial track length. This size of the uncertainty has also been found by a detailed study of the single track reconstruction efficiency from K_S-decays [58]. There, an error of ${}^{+3}_{-0}\%$ per track has been given.

p_t-range	H1 data	Monte Carlo
$0\ MeV \leq p_t \leq 150\ MeV$	81.8 %	86.4 %
$150\ MeV \leq p_t \leq 400\ MeV$	94.0 %	96.5 %
$400\ MeV \leq p_t \leq 800\ MeV$	98.0 %	98.7 %
$800\ MeV \leq p_t$	97.3 %	98.5 %

Table 3.8: Efficiency of the cut on d_{ca} in data (1996) and MC.

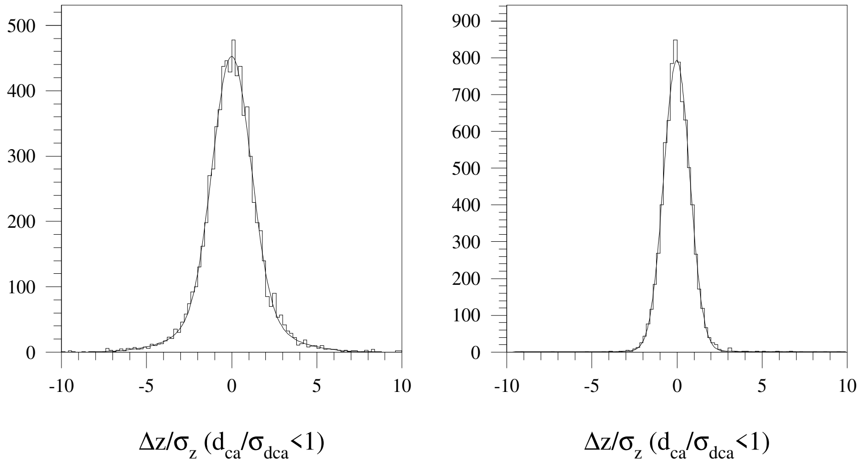

Figure 3.18: Distributions of the residuals $\Delta z/\sigma_z$ for tracks which point in $r\phi$ to the primary vertex. Left: Data (1996), right: MC. Both histograms are fitted with the sum of two gaussians. The width of the central part is 1.1 in data and 0.8 in MC.

3.1.4 Differential Cross Sections

The differential e^+p-cross sections in η can be calculated from the determined number of events and efficiencies as follows:

$$\frac{d\sigma^{vis}(e^+p \to D^*X)}{d\eta} = \frac{dN(D^* \to K\pi\pi)}{d\eta} \frac{1}{Br(D^* \to K\pi\pi) \cdot \epsilon_{trig} \cdot \epsilon_{rec} \cdot \epsilon_{vertex} \cdot L} \tag{3.8}$$

and similarly the differential cross section in p_T. Thanks to the Weizsäcker-Williams approximation, the γp-cross sections are then given by

$$\sigma_{ep} = \int_{y1}^{y2} \sigma_{\gamma p}(y)\ f_{\gamma/e}(y)\ dy \approx \sigma_{\gamma p}(\overline{y}) \int_{y1}^{y2} f_{\gamma/e}(y)\ dy \tag{3.9}$$

where the photon flux is calculated as described in chapter one:

$$f_{\gamma/e}(y) = \frac{\alpha_{em}}{2\pi} \left\{ \frac{1+(1-y)^2}{y} \ln \frac{Q^2_{max}}{Q^2_{min}} - 2\,\frac{1-y}{y} \right\}. \tag{3.10}$$

To be able to compare with QCD calculations, it is necessary to extrapolate to the cross sections for the production of charm quark pairs

$$\frac{d\sigma(\gamma p \to c\bar{c}X)}{d\eta} = \frac{1}{2\ B_{c\to D^{*\pm}}} \cdot \frac{d\sigma(\gamma p \to D^{*\pm}X)}{d\eta} \tag{3.11}$$

to which all the following pictures will refer. In figs. 3.19 and 3.20, these single inclusive cross sections for the two data samples of subtrigger 83 ($W_{\gamma p} = 194\ GeV$) and subtrigger 84 ($W_{\gamma p} = 88\ GeV$) are shown.

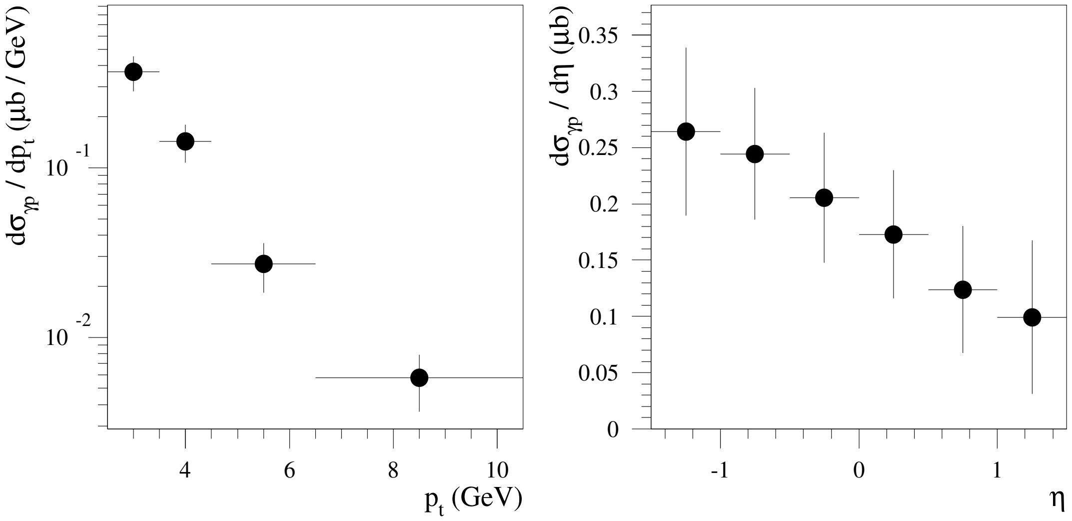

Figure 3.19: Differential cross sections $d\sigma_{\gamma p\to c\bar{c}X}/dp_t$ and $d\sigma_{\gamma p\to c\bar{c}X}/d\eta$ at $\overline{W_{\gamma p}} = 194\ GeV$. The error bars are the statistical error only. An overall systematic error of 15 % is not shown.

3.1.4.1 Systematic Errors

The given cross sections are subject to systematic uncertainties. The following sources of systematic errors are taken into consideration:

- The error on the single track reconstruction efficiency is estimated to be 2.5 % as discussed on page 53. For the three tracks in the reconstructed decay of the D^*-mesons this adds up to $\pm 7.5\%$.
- The simulation of the drift chamber trigger describes the data within 2 % [65], while the z-vertex trigger simulation contributes with 1 % [53].
- The uncertainty in the description of the event properties (which are relevant for the trigger and reconstruction efficiencies) by the event generators AROMA and PYTHIA is estimated to be 5 %.

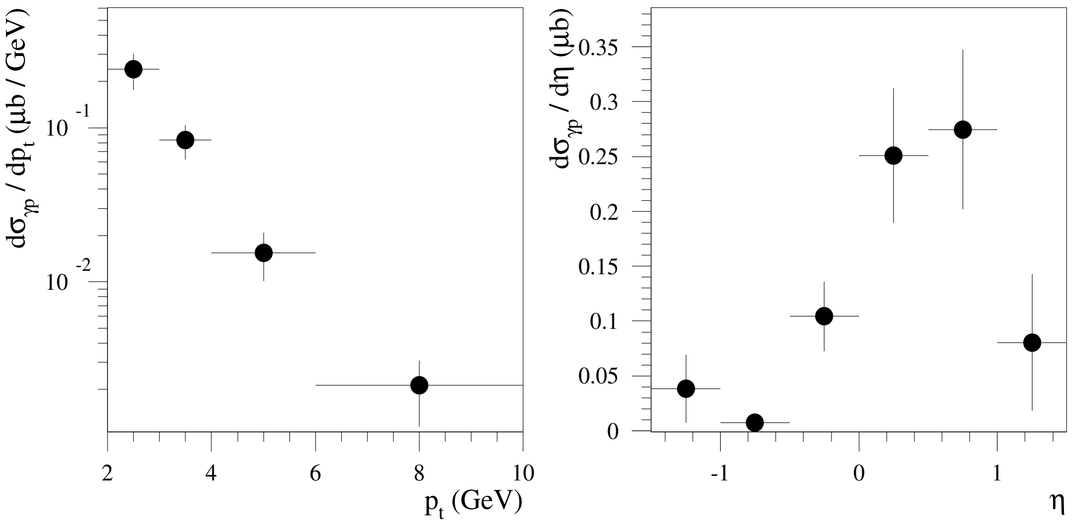

Figure 3.20: Differential cross sections $d\sigma_{\gamma p\rightarrow c\bar{c}X}/dp_t$ and $d\sigma_{\gamma p\rightarrow c\bar{c}X}/d\eta$ at $\overline{W_{\gamma p}} = 88\ GeV$. The error bars are the statistical error only. An overall systematic error of 15 % is not shown.

- The systematic uncertainty of the acceptance of the electron tagger at -33 m has been determined in [63] to be 5%. For the second tagger at -44 m, the slightly higher value of 6% was obtained in [64].
- The luminosity is known with a precision of 1.5% [63].
- Possible contributions of reflections have been investigated on page 35 to be smaller than 2%.
- The background from b-decays has been determined with AROMA 2.2 to be less than one percent.
- Finally the error on the branching fraction fraction $c \rightarrow D^* \rightarrow K\pi\pi$ is given in [33] as 7 %.
- A systematic error from the method to determine the number of events of 7% is also taken into account.

Summing up all systematic errors quadratically yields 15 %.

3.1.4.2 Toy Model

While the p_t distributions at the two different values of $W_{\gamma p}$ have a very similar shape and differ mainly in the absolute normalization, the differential spectra in η look significantly different. To figure out if the differences are due to the kinematics of the dynamics of the production process, the following toy model helps. The basic assumption is that the D^*-mesons are produced in photon-gluon collisions and only two D-mesons are found in the final state which are purely transversely oriented in the photon-gluon center of momentum frame (fig. 3.21). For each possible combina-

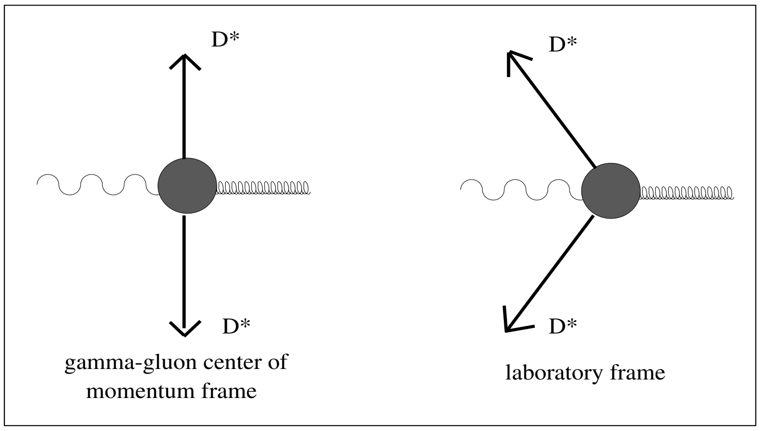

Figure 3.21: The toy model. A photon and a gluon collide and produce a pair of D^*-mesons which are back-to-back in the γg-center of momentum frame.

tion of x_g and y, the accompanying value $\eta = 0.5\ ln(E_g/E_\gamma)$ is calculated and filled into a η-histogram with a weight given by the corresponding Weizsäcker-Williams photon flux [5] at y times the gluon flux (from the MRSG parametrization [67]) at x_g and a scale $\mu_F = 100\ GeV^2$. p_T is obtained from the relation $p_T = x_g y s/4 - m^2_{D^*}$. In figs. 3.22 and 3.23 the results of this toy model are shown. The two-dimensional histograms on the left are the distributions of p_T versus η. Two vertical lines are drawn to mark the ends of the experimental acceptance in η. The horizontal line indicates the p_t cut on the D^* in the analysis (2.5 GeV for the 194 GeV sample and 2.0 GeV for the 88 GeV sample). The projection onto the η axis for all the events within the acceptance is then superimposed on the measured cross section. Clearly, the normalization can not be calculated with this primitive model and the obtained curve is therefore scaled to yield the same integral as the measured cross section. It is remarkable, how well the shape of the η distribution is described (especially at 88 GeV) and it would appear that the form of the measured differential cross sections in η is dominated by the production threshold of a pair of D-mesons above the given p_T cut. Actually, given a constant value of y, the left flank of the distribution is the mass and p_T-threshold, while the right flank is determined by the steeply falling gluon density with increasing value of x_g. The folding with the photon flux only smears the distributions. We see that the mass of the produced particles plays an important role.

[5] For the data sample at $\overline{W_{\gamma p}} = 194\ GeV$, the range in y is 0.29 to 0.62 and for the $\overline{W_{\gamma p}} = 88\ GeV$ sample it is 0.02 to 0.32. The photon flux is folded with the acceptance of the e-tagger at -44 m in the second case.

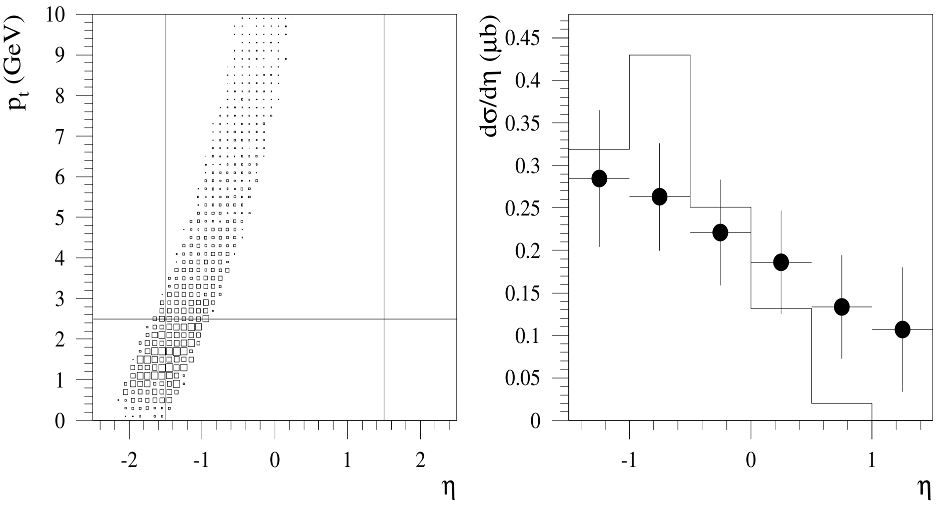

Figure 3.22: Toy model for the data sample at $\overline{W_{\gamma p}} = 194\ GeV$. Left histogram: p_t versus η of all generated D^*. The lines indicate the experimental acceptance. Right histogram: Toy model prediction (scaled) compared with the measured cross section (markers).

While the shape seems to be mainly determined by the simple kinematics of photon gluon collisions, one needs a real theory to understand the dynamics and to be able to calculate the normalization of the measured cross sections. The measurement is therefore confronted with QCD calculations in the next sections.

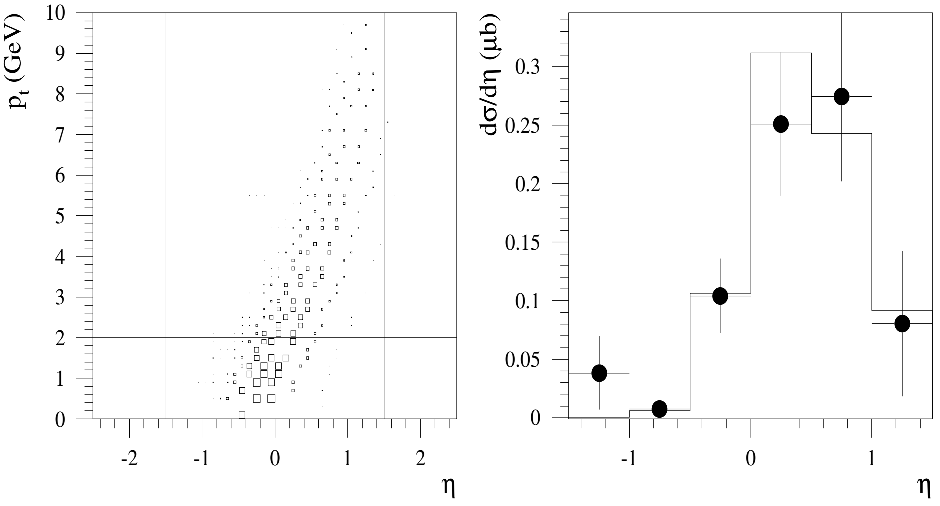

Figure 3.23: Toy model for the data sample at $\overline{W_{\gamma p}} = 88\ GeV$. Left histogram: p_t versus η of all generated D^*. The lines indicate the experimental acceptance. Right histogram: Toy model prediction (scaled) compared with the measured cross section (markers).

3.1.4.3 Comparison with QCD Calculations

The figures 3.24 and 3.25 show the measured differential cross sections together with the predictions of the NLO massive scheme calculation discussed in chapter one [14]. The following standard set of parameters has been used:

- $m_c = 1.5\ GeV$
- $\mu_F = \mu_\gamma = 2\ \mu_R = 2\ \sqrt{m_c^2 + p_T^2}$
- $\epsilon_{Peterson} = 0.035$
- Parametrization of the proton parton density function: MRS(G) [67]
- Parametrization of the photon parton density function: GRV HO [61]

Both calculations have been performed at a fixed $W_{\gamma p}$, namely at $W_{\gamma p} = 194\ GeV$ and $W_{\gamma p} = 88\ GeV$.

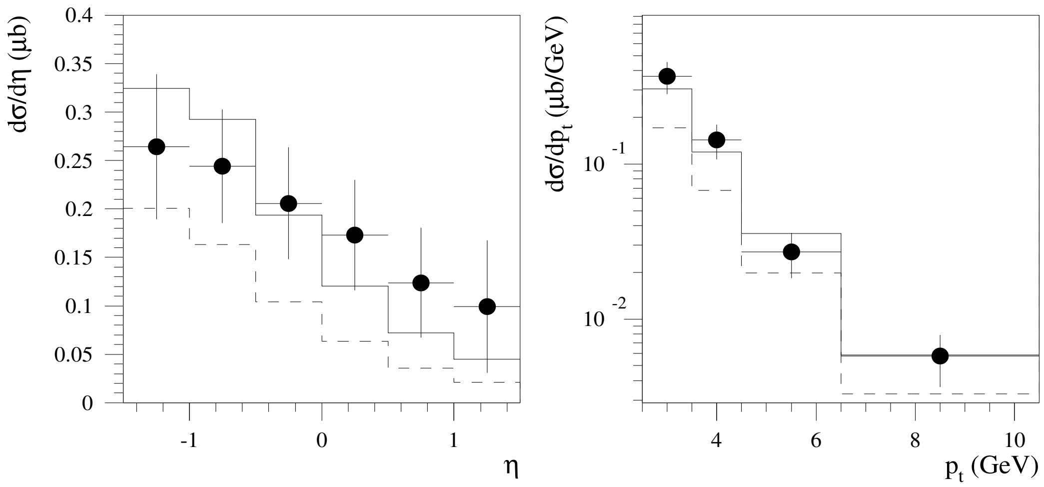

Figure 3.24: Measured differential cross sections $d\sigma_{\gamma p \to c\bar{c}X}/d\eta$ and $d\sigma_{\gamma p \to c\bar{c}X}/dp_T$ (markers) at $\overline{W_{\gamma p}} = 194\ GeV$ and prediction of the NLO massive scheme QCD calculation as described in the text (histograms). The lower (dashed) curve is LO only while the upper curve is the full NLO result.

While the LO calculation can not account for the observed cross section, the full NLO result is in fair agreement with the data. The radiative corrections are large, as expected from the small value of μ_R. An estimate of the importance of even higher order corrections can be gained by varying the involved scales. Since they are strictly correlated, a separate variation of them does not result in new insights and they are therefore changed all together in figures 3.26 and 3.27. The influence of the only phenomenological parameter $\epsilon_{Peterson}$ is studied in figures 3.28 and 3.29.

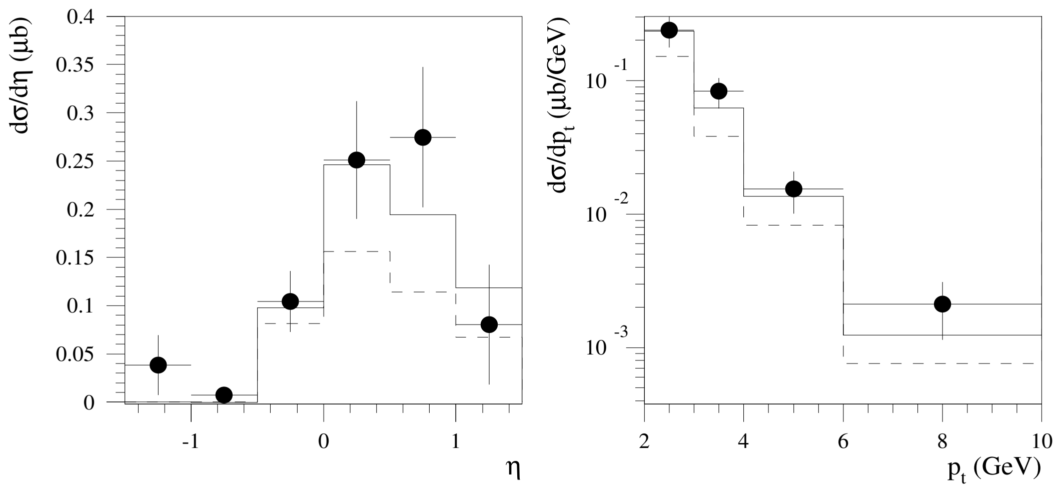

Figure 3.25: Measured differential cross sections $d\sigma_{\gamma p\rightarrow c\bar{c}X}/d\eta$ and $d\sigma_{\gamma p\rightarrow c\bar{c}X}/dp_T$ (markers) at $\overline{W_{\gamma p}} = 88\ GeV$ and prediction of the NLO massive scheme QCD calculation as described in the text (histograms). The lower (dashed) curve is LO only while the upper curve is the full NLO result.

It is varied from 0.025 to 0.045 around the central value 0.035 which has been derived from fits to e^+e^--data (see chapter one). A clear influence can be observed, although it is smaller than the impact of the scales. The scale uncertainty and the dependence on the $\epsilon_{Peterson}$ limit the reliability of the QCD calculation and will be the main sources of systematic errors in the determination of the gluon density in chapter four. Different parametrizations of the parton densities in the proton and the photon have a small influence on the predictions of the QCD calculation, as can be seen in figs. 3.30 and 3.31. There, the two combinations MRSG-GRV HO and MRS(A')[60]-LAC1[68] are compared. Obviously the differences between the parton density parametrizations are much smaller than the scale dependences and it will not be possible to distinguish between them with the present accuracy of the theoretical calculations.

The relative size of the resolved contribution to the full differential cross sections are shown in fig. 3.33 and fig. 3.32. Only in the forward region $\eta \geq 0.5$, a sizeable contribution of more than 10% is visible. The reason for this is that only a very small fraction of the gluons in the photon carry enough energy to produce a charm quark pair in the visible η range. The bulk of the resolved contribution to the cross section would be expected more forward, as can be inferred from fig. 3.34. In the massive scheme calculation, direct and hadronic part are therefore quite clearly separated, a fact which reflects also in an extremely small dependence of cross sections on the factorization scale at the photon side (μ_γ) and justifies to talk about the two contributions separately. To further reduce the already small influence of the hadronic photon in the determination of the gluon density in chapter four,

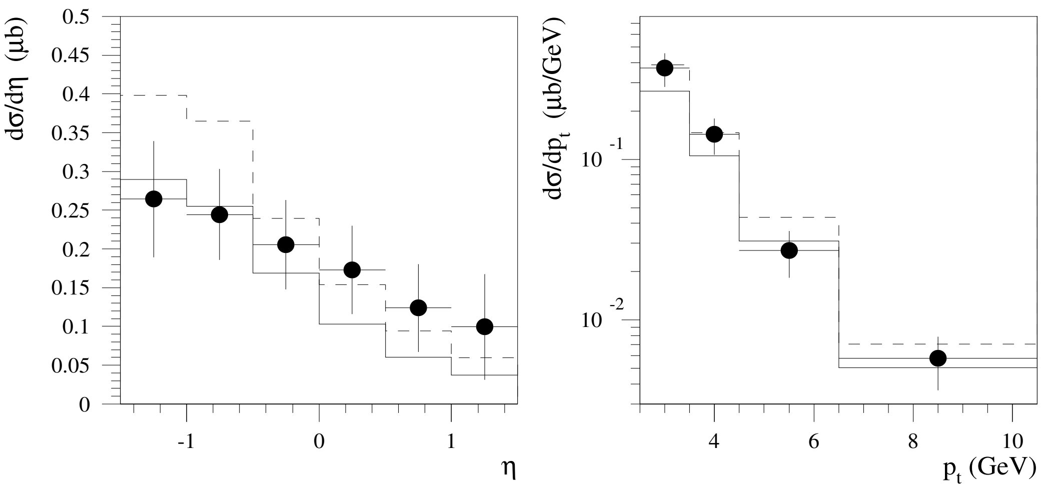

Figure 3.26: Measured differential cross sections $d\sigma_{\gamma p\rightarrow c\bar{c}X}/d\eta$ and $d\sigma_{\gamma p\rightarrow c\bar{c}X}/dp_T$ (markers) at $\overline{W_{\gamma p}} = 194\ GeV$ and the prediction of the NLO massive scheme QCD calculation (histograms). The lower curve corresponds to a choice of twice the standard scales and the upper (dashed) histogram to 0.5 times the standard scales.

only D^* with $\eta \leq 0.5$ will be taken into account.

Massless Calculations In figs. 3.35 and 3.36 the measured single inclusive cross sections are compared with the massless calculation [23] discussed in chapter one.
As expected, the massless calculation gives a poorer description of the data than the massive scheme but does not completely fail. Especially at $\overline{W_{\gamma p}} = 88\ GeV$ the agreement is not too bad. It has been argued that resummation terms may be cancel the effect of missing mass terms [25].

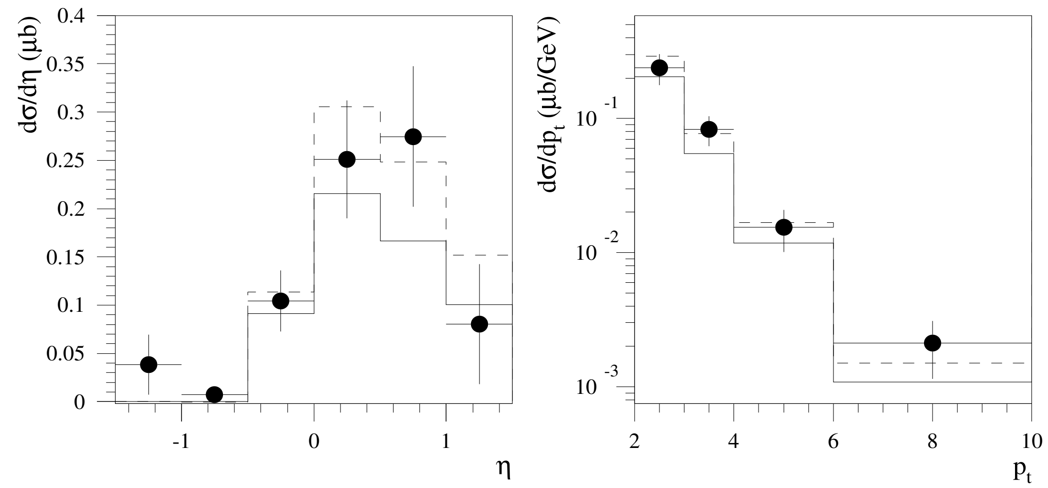

Figure 3.27: Measured differential cross sections $d\sigma_{\gamma p\to c\bar{c}X}/d\eta$ and $d\sigma_{\gamma p\to c\bar{c}X}/dp_T$ (markers) at $\overline{W_{\gamma p}} = 88\ GeV$ and the prediction of the NLO massive scheme QCD calculation (histograms). The lower curve corresponds to a choice of twice the standard scales and the upper histogram to 0.5 times the standard scales.

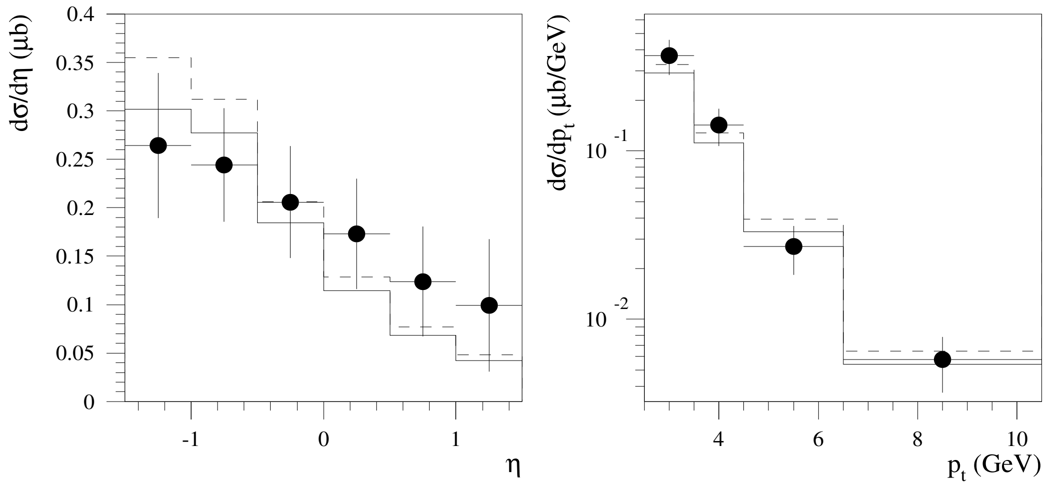

Figure 3.28: Measured differential cross sections $d\sigma_{\gamma p\to c\bar{c}X}/d\eta$ and $d\sigma_{\gamma p\to c\bar{c}X}/dp_T$ (markers) at $\overline{W_{\gamma p}} = 194\ GeV$ and the prediction of the NLO massive scheme QCD calculation (histograms). The lower curve corresponds to $\epsilon_{Peterson} = 0.045$ and the upper histogram to $\epsilon_{Peterson} = 0.025$.

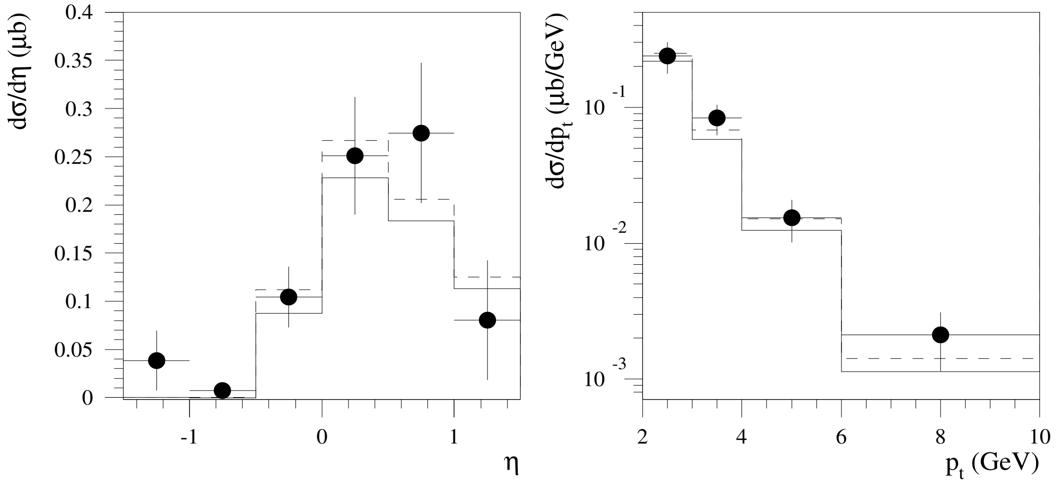

Figure 3.29: Measured differential cross sections $d\sigma_{\gamma p \to c\bar{c}X}/d\eta$ and $d\sigma_{\gamma p \to c\bar{c}X}/dp_T$ (markers) at $\overline{W_{\gamma p}} = 88\ GeV$ and the prediction of the NLO massive scheme QCD calculation (histograms). The lower curve corresponds to $\epsilon_{Peterson} = 0.045$ and the upper histogram to $\epsilon_{Peterson} = 0.025$.

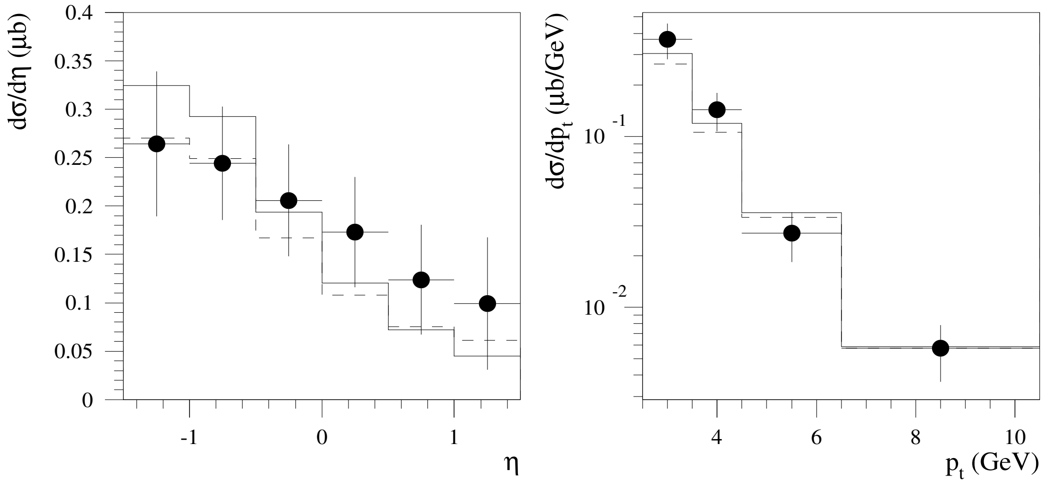

Figure 3.30: Measured differential cross sections $d\sigma_{\gamma p \to c\bar{c}X}/d\eta$ and $d\sigma_{\gamma p \to c\bar{c}X}/dp_T$ (markers) at $\overline{W_{\gamma p}} = 194\ GeV$ and the prediction of the NLO massive scheme QCD calculation (histograms). The lower curve corresponds to MRSG-GRV HO and the upper histogram to MRS(A')-LAC1.

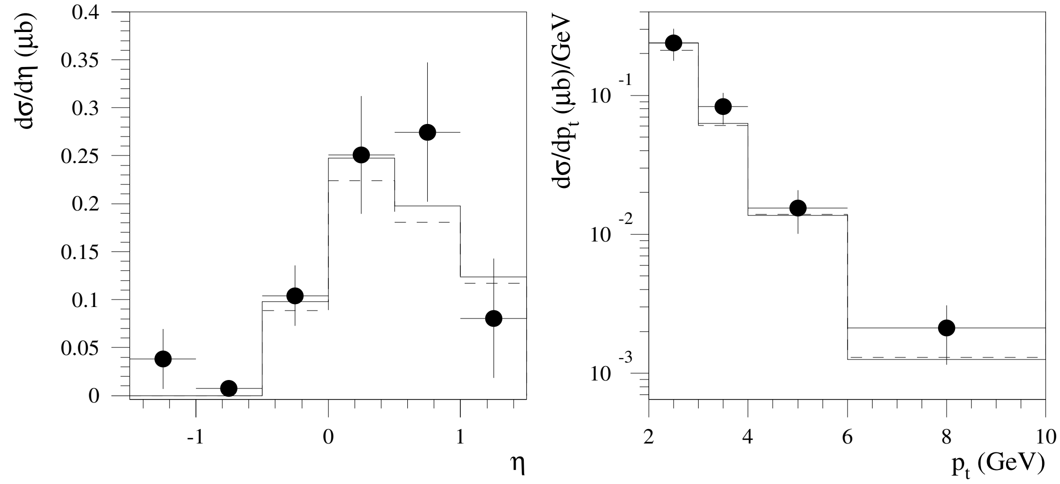

Figure 3.31: Measured differential cross sections $d\sigma_{\gamma p\to c\bar{c}X}/d\eta$ and $d\sigma_{\gamma p\to c\bar{c}X}/dp_T$ (markers) at $\overline{W_{\gamma p}} = 88\ GeV$ and the prediction of the NLO massive scheme QCD calculation (histograms). The lower curve corresponds to MRSG-GRV HO and the upper histogram to MRS(A')-LAC1.

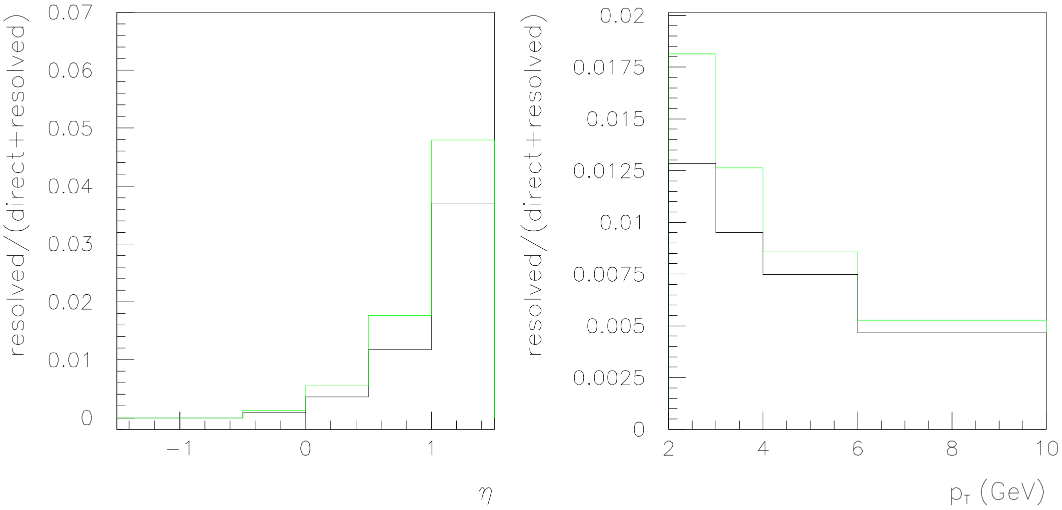

Figure 3.32: Prediction of the NLO massive scheme calculation concerning the contribution of the hadronic photon at $W_{\gamma p} = 88\ GeV$. Upper (light) curve: MRS(A')+LAC1. Lower histogram: MRS(G)+GRV-HO.

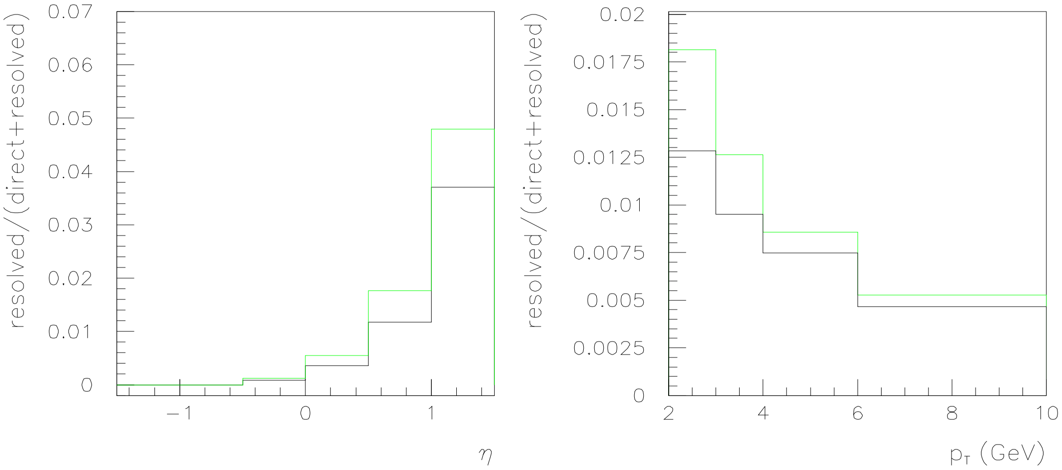

Figure 3.33: Prediction of the NLO massive scheme calculation concerning the contribution of the hadronic photon at $W_{\gamma p} = 194\ GeV$. Upper (light) curve: MRS(A')+LAC1. Lower histogram: MRS(G)+GRV-HO.

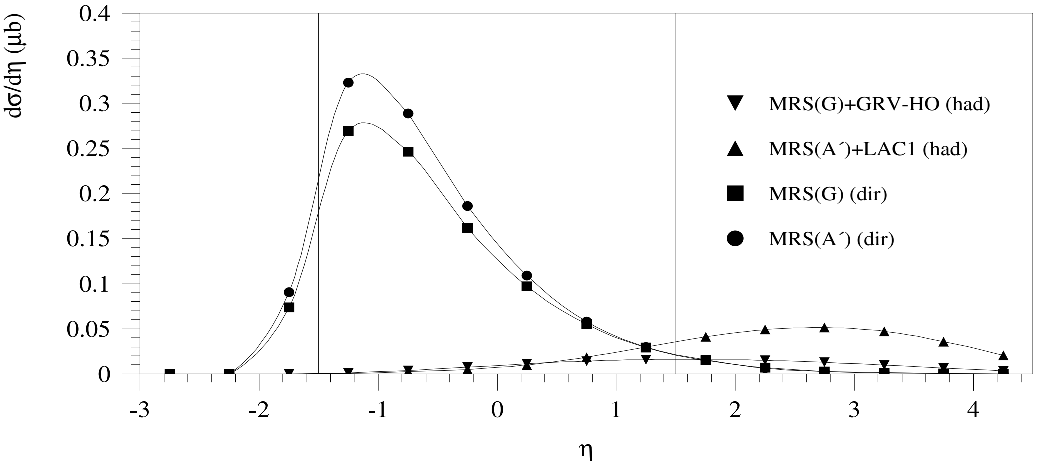

Figure 3.34: Calculated cross sections $d\sigma_{\gamma p \to c\bar{c}X}/d\eta$ at $W_{\gamma p} = 194\ GeV$ (in massive scheme, NLO). The direct (left peaks) and hadronic (right peaks) parts are shown separately for two different sets of parton density parametrizations. The vertical lines mark the visible range.

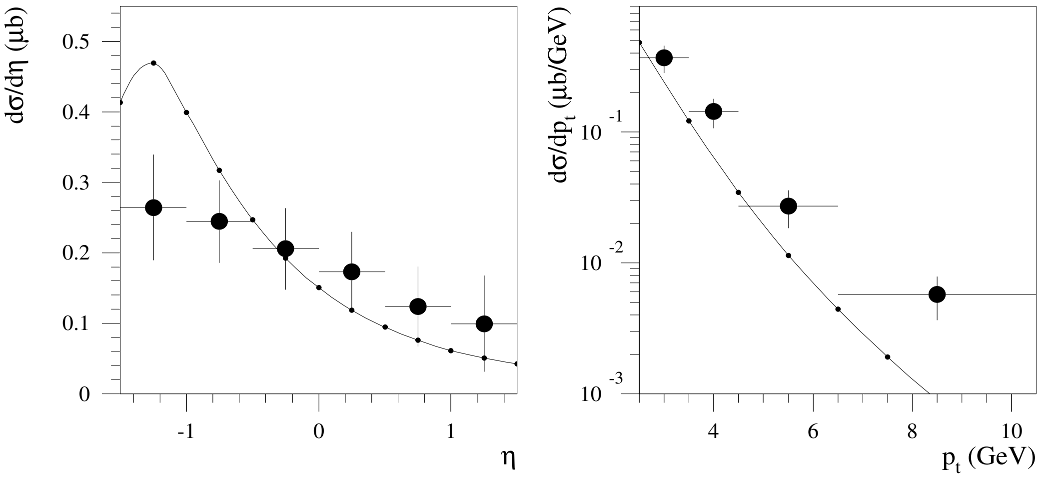

Figure 3.35: Measured differential cross sections at $\overline{W_{\gamma p}} = 194\ GeV$ (markers) and the prediction of the massless NLO QCD calculation described in the text (histogram).

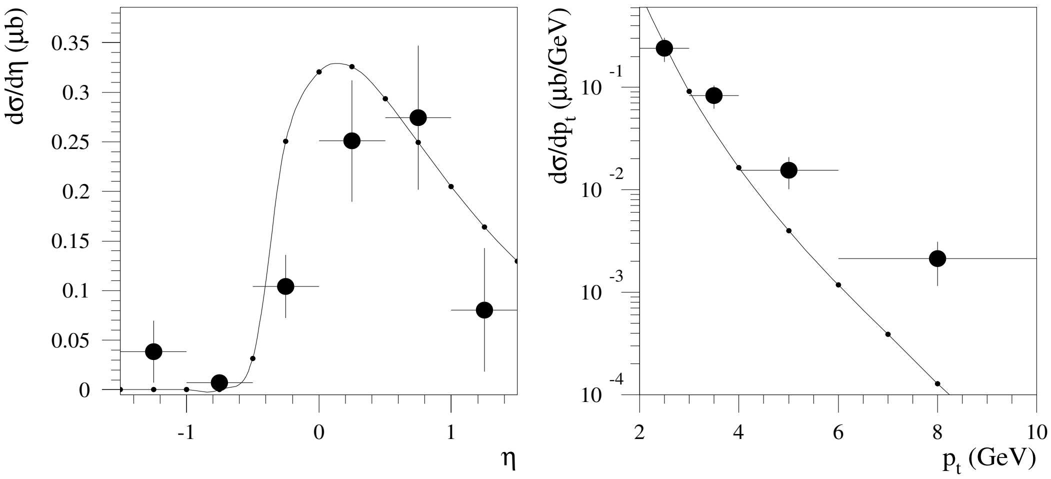

Figure 3.36: Measured differential cross sections at $\overline{W_{\gamma p}} = 88\ GeV$ (markers) and the prediction of the massless NLO QCD calculation described in the text (histogram).

3.2 Energyflow

As we have seen in the last section, the massive scheme QCD model of charm photoproduction is able to describe accurately both shape and normalization of the single inclusive D^*-spectra (at $\overline{W_{\gamma p}} = 88\ GeV$ and $\overline{W_{\gamma p}} = 194\ GeV$). A comparison to the massless calculations has shown that they are not well suited in the probed p_t-range. A significant contribution from the resolved process is not expected for kinematical reasons. So there is no reason to doubt, that charm in the visible range is predominantly produced via photon-gluon fusion and higher order corrections to that process. Nevertheless, there is another prediction specific to the photon-gluon fusion process which can be tested. It is about the energy flow in these event and the basic idea is the following: In the photon-gluon fusion process, the initial state carries color [6]. Since the colour must be neutralized, an interaction between the charm quarks and the proton remnant must occur. Actually the colours carried by the charm quarks find their counterpart in the remainder of the proton and one can think of strings being formed between one charm quark and a spectator quark in the proton and the other charm quark and the remaining diquark (fig. 3.37, left). The fragmenting strings populate the (forward) region between the $c\bar{c}$-system and

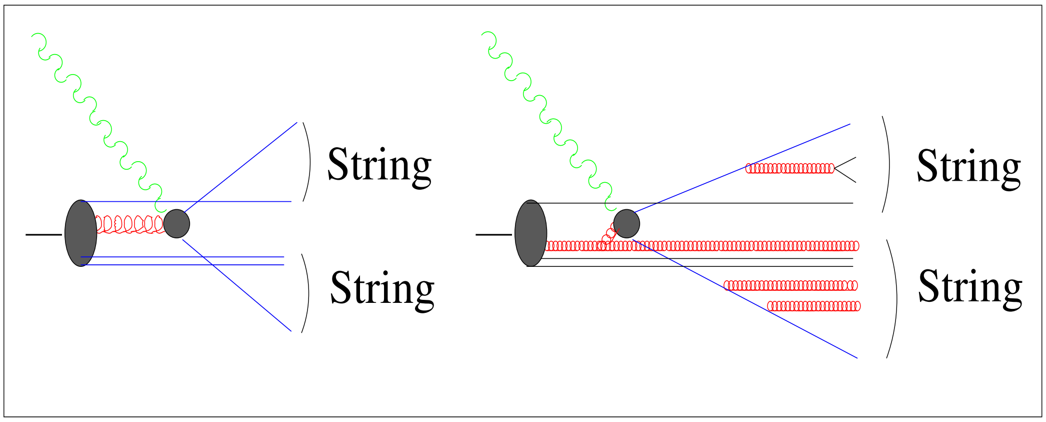

Figure 3.37: Schematic picture of charm production in photon-gluon fusion. Left: Pure LO. Right: LO graph plus parton showers in the initial and final state. Typically AROMA/JETSET forms two strings out of the partons in the final state each containing one charm quark and a quark or diquark from the proton remnant.

the proton remnant with particles, while the backward space between the $c\bar{c}$-system and the outgoing positron is empty. This outlined picture is implemented in the MC generator AROMA [57], which calls JETSET [62] for the fragmentation part. I will first describe shortly how charm photoproduction is simulated in AROMA/JETSET

[6] This situation is completely different from e^+e^-- collisions where the heavy quark pair is produced in γ/Z^0-decays.

and then compare the prediction with data in a measurement of the energy flow in D^*-events.

3.2.1 The MC model

The AROMA/JETSET model consists of three ingredients:

- Charm quarks are produced in the hard scattering of photons and gluons, the partonic cross sections being calculated in leading order QED and QCD.
- Higher order corrections are simulated by initial state and final state parton showers [62].
- The produced charm quarks and the light quarks and gluons from the parton showers are then fragmented into hadrons using the string fragmentation model implemented in JETSET.

To be more specific, a typical event with parton showers looks like fig. 3.37 (right). The photon and a gluon from the proton meet and fusion into a $c\bar{c}$-pair. The gluon can emit other gluons before the hard interaction with the photon, and the produced gluons can split in a perturbative QCD cascade (until a certain cut-off is reached) into quarks and gluons (initial state parton shower). The charm quarks are also allowed to radiate gluons which again can shower into more gluons and quarks. In the end, a whole bunch of particles is produced which form (usually) two strings: One string contains a charm quark and the final state parton shower from it together with a spectator quark from the proton. The other charm quark goes into the second string together with it's final state shower and the remaining diquark from the proton. The initial state shower is attached to one of the two strings. They are fragmented in the following way: The quarks and gluons of the string form a colour field with constant energy density. The potential between the particles is assumed to be linear (inspired by the confinement). By producing a new $q\bar{q}$-pair from the energy stored in the colour field, the string breaks up into two strings or one string and a hadron. This process is repeated as long as the energy of the string is large enough. The distribution of the initial energy between the two new systems when a string breaks up is not inherently given by the model but has to be defined externally. In the string model for massless particles, the assumption that no direction is favored and each breaking of a string is independent leads to the "Lund" fragmentation function [69]. To describe the production of heavy quarks the harder PSSZ-fragmentation function is used in JETSET. All AROMA predictions in this analysis are obtained with the standard set of the JETSET parameters [62].

3.2.2 Energy Flow in η

Event Selection For this measurement, only data from the year 1996, corresponding to an integrated luminosity of 7.3 pb^{-1} is used. Events triggered by subtrigger 83 are selected and the same decay channel $D^* \rightarrow D^0\pi_s \rightarrow K\pi\pi_s$ is reconstructed.

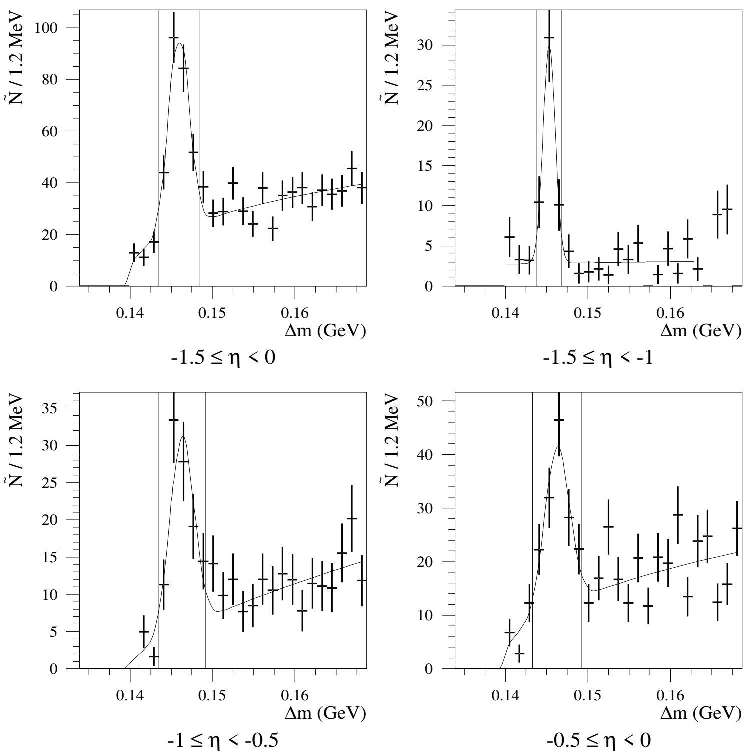

Figure 3.38: D^*-signals after the analysis cuts described in the text. The first histogram shows the total signal in the full range $-1.5 \leq \eta \leq 0$, the remaining three the signals in the three bins of η. Lines are drawn to indicate the signal regions used in the analysis of the energy flow.

Similar analysis cuts as for the single inclusive D^*-spectra (last section) are applied. The only difference is that I only use D^* with negative η to improve the signal to background ratio. The analyzed data sample is therefore characterized as follows:

- $\overline{W_{\gamma p}} = 194\ GeV$
- $p_t(D^*) \geq 2.5\ GeV$
- $p_t(\pi_s) \geq 150\ MeV$, $p_t(\pi, K) \geq 500\ MeV$
- $-1.5 \leq \eta(D^*) \leq 0$
- D^0 mass window: $\pm 50\ MeV\ (= 2\sigma)$

The full signal with these cuts is shown in the first picture of fig. 3.38. A further reduction of the background compared to the total signal (fig. 3.5) is observed which is due to the additional cut on η and the smaller mass window for the D^0 [7]. Very

[7] A smaller range in the D^0-mass can be selected since for this measurement the precise efficiency of this cut is irrelevant.

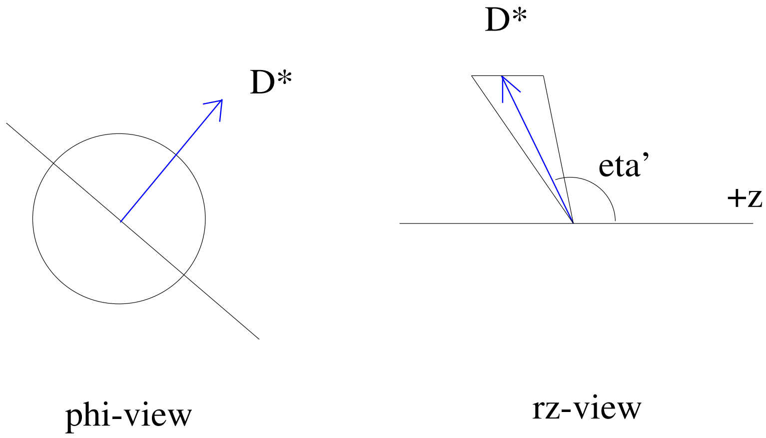

Figure 3.39: Schematic of a D^*-event. The energy flow in the events is measured as a function of the *pseudorapidity* $\tilde{\eta}$ (denoted with eta' in the picture) for events with a D^* in a small range in rapidity η_{D^*} as indicated in the right figure. The two hemispheres in the ϕ-view (left) are analysed separately.

clear signals are also seen when the range in η is divided in three bins (see also fig. 3.38). The same function as in the last section is used to fit the signal and the background, but in this case, the width of the peak is not fixed. All events within $\pm 2\sigma$ around the peak positions are are selected (signal region).

The Energy Flow For these events, the energy flow is analysed as follows (fig. 3.39): The energy flow in the hemisphere of the D^* as a function of the pseudorapidity $\tilde{\eta}$ is averaged over all D^*-events in the signal region of a certain bin in η_{D^*} (fig. 3.40). Background subtraction is done using the right sidebands and scaling the background corresponding to the signal to background ratio determined in the fit.

The same distribution is calculated for the energy flow in the complementary hemisphere (fig. 3.40).

For the determination of the energy, charged tracks and clusters in the calorimeters (liquid argon and SpaCal) are taken into account. Charged tracks are used, if they satisfy the track selection cuts described in section 3.1. Clusters are used, if the reconstructed energy is above 400 MeV and if none of the selected tracks point to their center within 40 cm. This distance has been chosen since for low energetic hadrons more than 95% of the energy deposit in the calorimeter is within this radius [70]. It has also shown in [70], that the response of the liquid argon calorimeter to hadrons below 2 GeV is well described in the detector simulation.

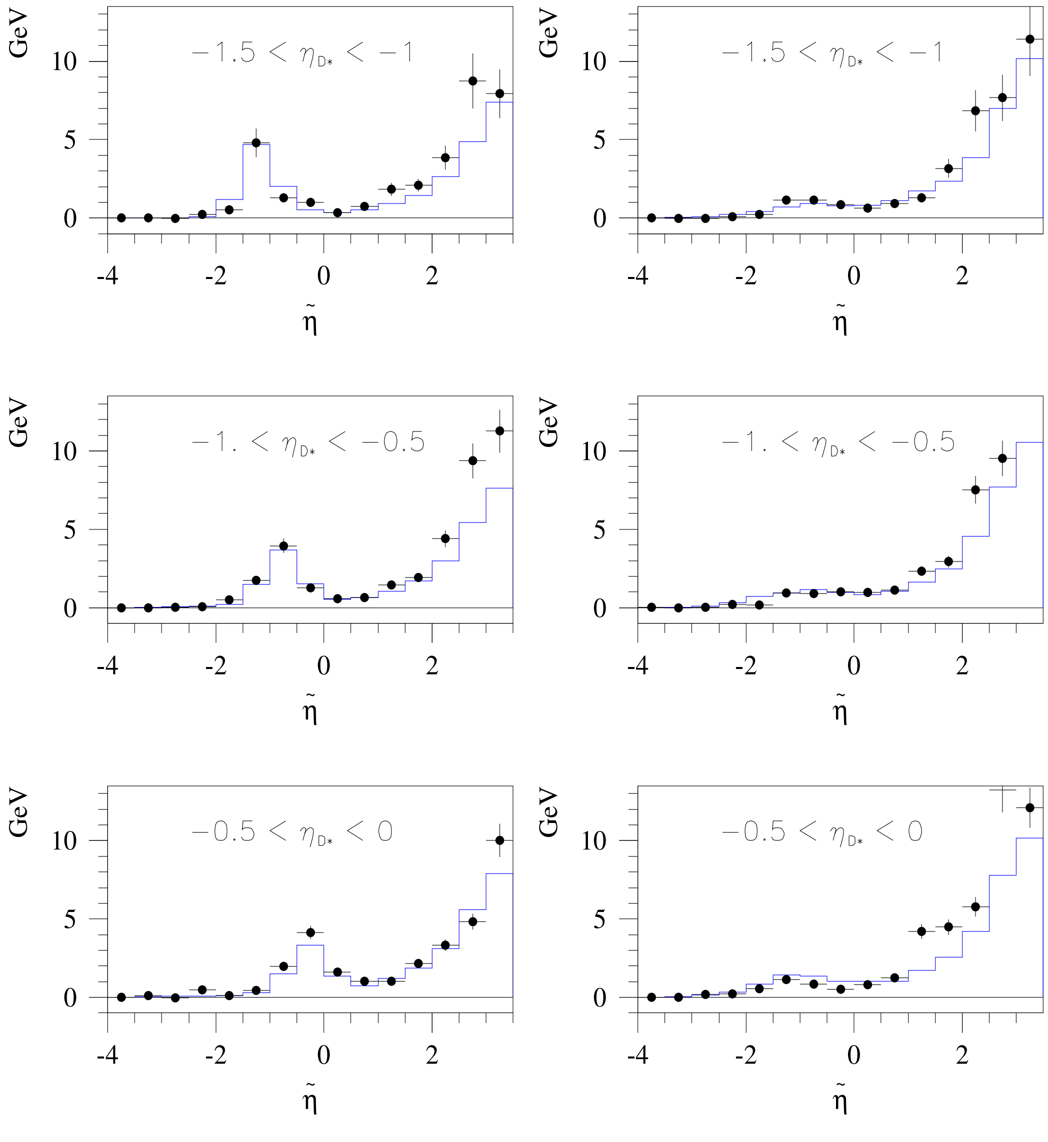

Figure 3.40: Energy flow for D^*-events in the three bins of η_{D^*}. The histograms in the left column show the energy flow in the hemisphere of the D^* and in the right column the same distribution for the second hemisphere is plotted. Markers indicate data and the solid histograms refer to the Monte Carlo (AROMA) prediction.

3.2.3 Energy Flow in ϕ

A similar measurement for the energy flow as in the variable $\tilde{\eta}$ can be carried out in the variable ϕ (fig. 3.41). All D^* candidates in $-1.5 \leq \eta \leq 0$ are selected. The energy flow as a function of ϕ is shown in fig. 3.42, where tracks and clusters with $\tilde{\eta} \leq 1.4$ is not taken into account (to cut out the proton remnant).

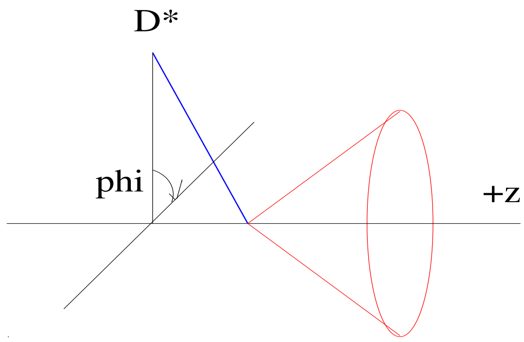

Figure 3.41: Schematic of a D^*-event. The variable ϕ is defined by putting the D^* to $\phi = 0$. Energy in the cone ($\tilde{\eta} \leq 1.4$) is not taken into account.

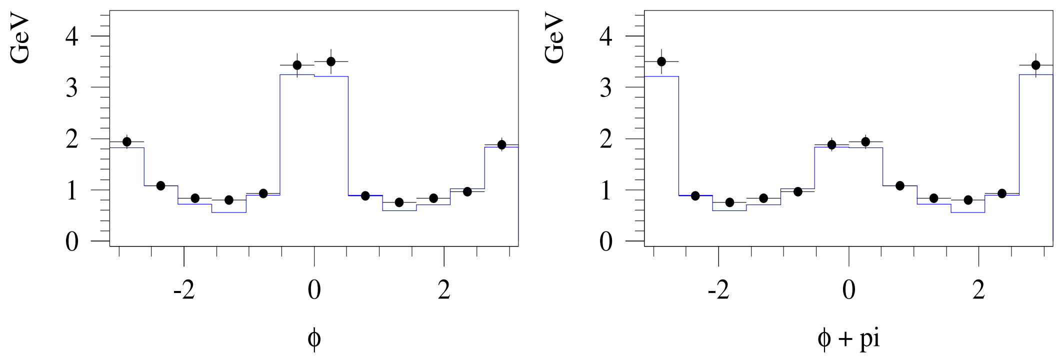

Figure 3.42: Energy flow in ϕ. $\phi = 0$ is defined by the direction of the D^*. The markers are the data and the solid histogram is the Monte Carlo (AROMA) prediction.

3.2.4 Interpretation

Energy Flow in $\tilde{\eta}$: Four regions in $\tilde{\eta}$ can be distinguished:

- The D^*-region (in the histograms referring to the D^*-hemisphere) and its counterpart in the other hemisphere which represents the second charm quark (in 98% of all the MC events).
- The space backward to the D^* or the second charm quark.
- The proton remnant and
- the intermediate region between the D^* (or the second charm) and the proton remnant.

While the most forward part, starting at about $\tilde{\eta} \approx 1 - 1.5$ where the energy flow of the dissociated proton shows up is poorly described by the MC model, the agreement in the other three regions is good, both in the D^*-hemisphere and the other side.

The gap between the D^* and the proton remnant is filled in data with energy flow exactly as predicted by the string fragmentation model. Backward to the D^* (or the other charm quark), no energy is observed at all, the only exception being two events in $-0.5 \leq \eta_{D^*} \leq 0$. *No signs of a prominent photon remnant, which could point to a hadronic behaviour of the photon or even intrinsic charm in the photon, is seen in any of the events*, confirming the expectation.

Energy Flow in ϕ: Good agreement between data and the Monte Carlo simulation is found in this measurement, too. The peak at $\phi = \pi$ originates in the Monte Carlo in 97% of the events from the second charm quark. It's shape and also the overall normalization of the distribution is very well described whereas the bump between the charm and the anti-charm might be slightly overestimated in the simulation.

Conclusion The results from this section imply that one can trust the MC description when designing a method to separate the proton remnant from the $c\bar{c}$-system. In the second section of the next chapter such a method will be presented to reconstruct x_g from the hadronic final state of the charm events by reconstructing the sum

$$x_{JB}^{rec} = \frac{\sum_{c\bar{c}-system}(E + p_L)}{2\ E_p} \qquad (3.12)$$

which relies on the correct separation of the $c\bar{c}$-system and the proton remnant.

Chapter 4

Determination of the Gluon Density in the Proton

In this chapter, a direct, NLO order determination of the gluon density in tagged charm photoproduction is given. In the first section, a measurement relying on the reconstruction of x_g from the measured D^* is presented. With this method, both data samples from the e-taggers at -33 m and at -44 m can be used. The obtained results are compared to previous determinations of the gluon density from scaling violations of F_2 and from the (2+1)-jet rate in DIS at HERA.

As a cross check, a second method to reconstruct x_g which foots on the reconstruction of the Jacquet-Blondel sum is applied in section two. For the reasons discussed in the last chapter, it can only be applied for the part of the data which corresponds to the lowest values of x_g.

4.1 D^*-Method

The method is outlined in chapter one. I start with the measurement of the differential cross sections $d\sigma/dx_g^{rec}$.

4.1.1 Measurement of $d\sigma/dx_g^{rec}$

The same data samples as used in chapter three for the single inclusive D^*-spectra are analysed. As explained on page 12, the measurement of $d\sigma/dx_g^{rec}$ should be performed using only events in a narrow range in y. To meet this requirement, the data sample of subtrigger 83 is split into two subsamples, so that the three analysed data sets can be characterized as follows:

- Data sample at $\overline{W_{\gamma p}} = 88\ GeV$ or $\overline{y} = 0.092$ (e-tagger at -44 m, subtrigger 84) with the analysis cuts
  - $p_T(D^*) \geq 2.0\ GeV$, $p_T(\pi_S) \geq 150\ MeV$, $p_T(K,\pi) \geq 350\ MeV$

  - $0 \leq \eta(D^*) \leq 1$. The cut $0 \leq \eta$ will be explained later and the cut $\eta \leq 1$ is applied to improve the signal to background ratio.

- Data sample at $\overline{W_{\gamma p}} = 223\ GeV$ (e-tagger at -33 m, subtrigger 83) with the following cuts

  - $0.5 \leq y \leq 0.62$
  - $p_T(D^*) \geq 2.5\ GeV$, $p_T(\pi_S) \geq 150\ MeV$, $p_T(K,\pi) \geq 500\ MeV$
  - $-1.5 \leq \eta(D^*) \leq 0.5$. The cut $\eta \leq 0.5$ eliminates most of the resolved photon contribution and improves the signal to background ratio ratio.

- Data sample at $\overline{W_{\gamma p}} = 185\ GeV$ (e-tagger at -33 m, subtrigger 83). All cuts are the same as for the previous data set, but y is required to be within $0.29 \leq y \leq 0.5$.

Figs. 4.1 - 4.4 show the Δm-histograms for these three data sets in bins of the variable x_g^{rec}, which is calculated in the following way, assuming a charm mass of

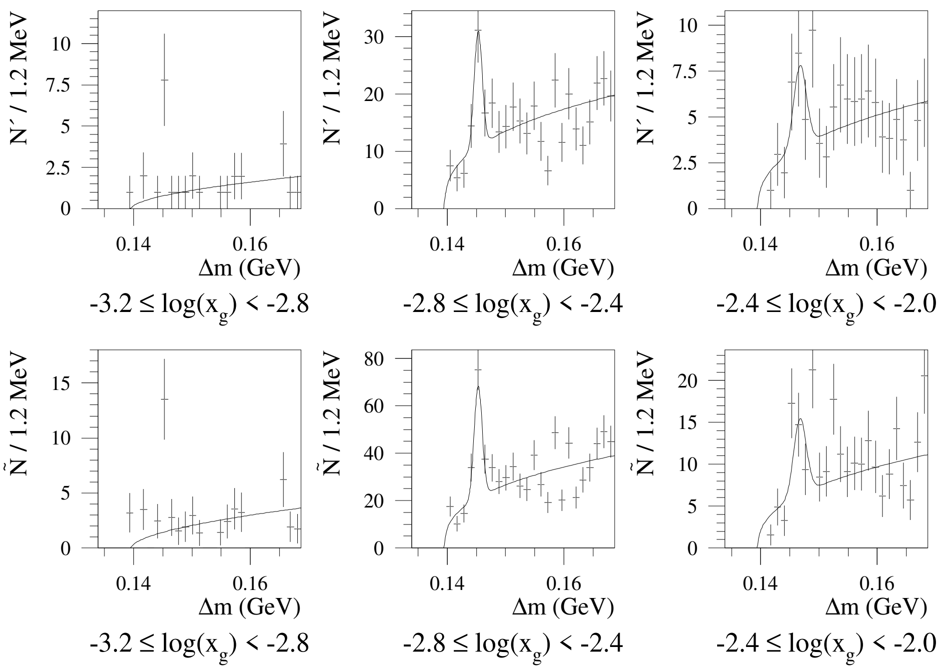

Figure 4.1: Δm-histograms of the data sample at $\overline{W_{\gamma p}} = 223\ GeV$ in bins of x_g^{rec}. Upper row: Equivalent number of events (N'). Lower row: Weighted number of events ($\tilde{N}$).

$m_c = 1.5\ GeV$:

$$p_t(c) = 1.2 \cdot p_t(D^*) \tag{4.1}$$

$$p_L(c) = p_L(D^*) \tag{4.2}$$
$$E(c) = \sqrt{p_t(c)^2 + p_L(c)^2 + m_c^2} \tag{4.3}$$
$$z = \frac{E(c) - p_L(c)}{2 \cdot y \cdot E_e} \tag{4.4}$$
$$\hat{s} = \frac{p_t(c)^2 + m_c^2}{z(1-z)} \tag{4.5}$$
$$x_g^{rec} = \frac{\hat{s}}{y \cdot s} \tag{4.6}$$

The variable y is taken from the measured value for all events tagged in the

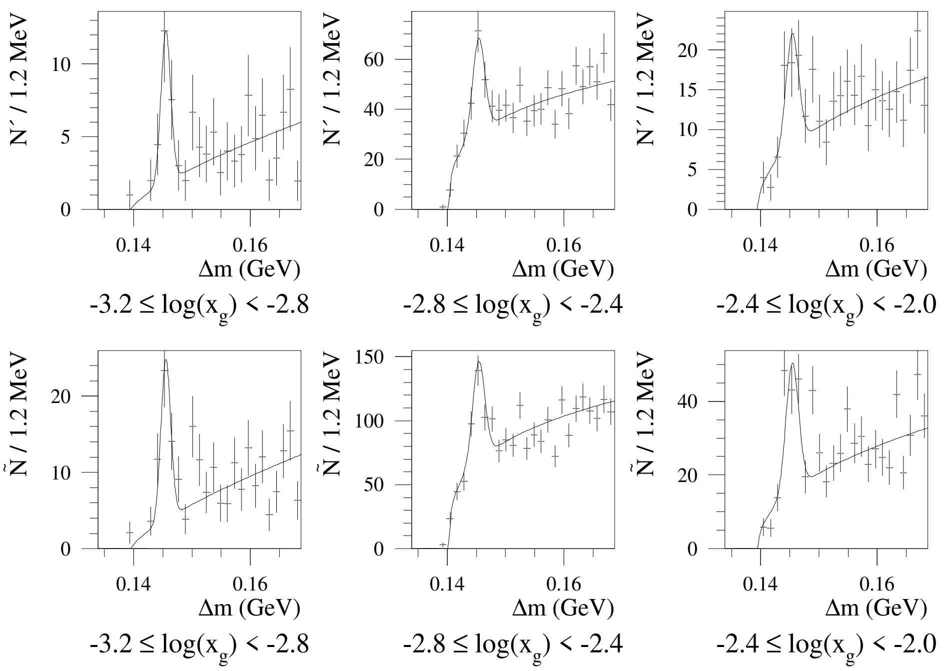

Figure 4.2: Δm-histograms of the data sample at $\overline{W_{\gamma p}} = 185\ GeV$ in bins of x_g^{rec}. Upper row: Equivalent number of events (N'). Lower row: Weighted number of events ($\tilde{N}$).

calorimeter at -33 m whereas for the e-tagger at -44 m the average value 0.092 is used for reasons which are explained in the chapters two and three. The use of an average value for y is the reason for the cut $0 \leq \eta(D^*)$ for the data set at 88 GeV. Events with $\eta(D^*) \leq 0$ stem predominantly from the tail of the tagger acceptance at higher values of y for which the assumption of $y \approx 0.092$ is not justified.

The number of D^* in each bin is determined with the method of the equivalent number of events in exactly the same fashion as for the measurement of the single inclusive spectra in chapter three except for the first bin in x_g^{rec} and the 223 GeV sample. In this special case, the number of D^* is determined by counting the number

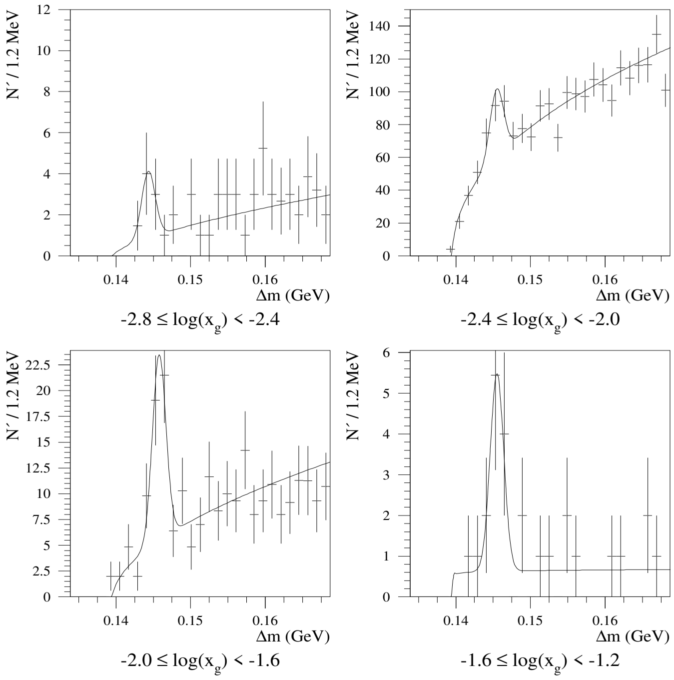

Figure 4.3: Δm-histograms of the equivalent number of events N' of the data sample at $\overline{W_{\gamma p}} = 88\ GeV$ in bins of x_g^{rec}.

of entries in the histogram in the five bins closes to the peak position and subtracting the fitted background. The following number of events are observed: For the data set from the e-tagger at -33 m:

		$-3.2 \leq log(x_g) \leq -2.8$	$-2.8 \leq log(x_g) \leq -2.4$	$-2.4 \leq log(x_g) \leq -2.0$
$\tilde{N}$	$0.5 \leq y \leq 0.62$	12 ± 4.3	67 ± 19	20 ± 9
$\tilde{N}$	$0.29 \leq y \leq 0.5$	36 ± 12	167 ± 53	78 ± 22

and for the data set from the e-tagger at -44 m:

	$-2.8 \leq log(x_g) \leq -2.4$	$-2.4 \leq log(x_g) \leq -2$	$-2 \leq log(x_g) \leq -1.6$	$-1.6 \leq log(x_g) \leq -1.2$
$\tilde{N}$	6.1 ± 2.9	170 ± 51	68 ± 19	10.4 ± 3.8

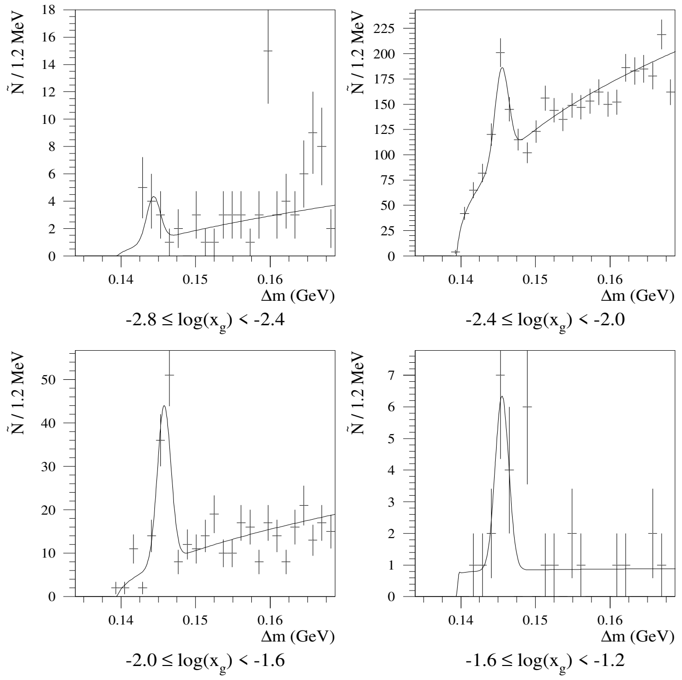

Figure 4.4: Δm-histograms of the weighted number of events $\tilde{N}$ of the data sample at $\overline{W_{\gamma p}} = 88\ GeV$ in bins of x_g^{rec}. The outlyer in the first histogram is due to a few events with high weights as can be inferred by comparing it with the corresponding N'-histogram.

The reconstruction and trigger efficiencies are determined using Monte Carlo. Since the resolved part is at 88 GeV negligible, the efficiencies can be calculated using AROMA (which describes the direct part) only. The applied η-cuts in the data samples at 185 GeV and 223 GeV eliminates the biggest part of the resolved contribution (so that it is less than 5% and therefore the same holds true in these cases. Figs. 4.5 and 4.6 show the measured differential cross sections

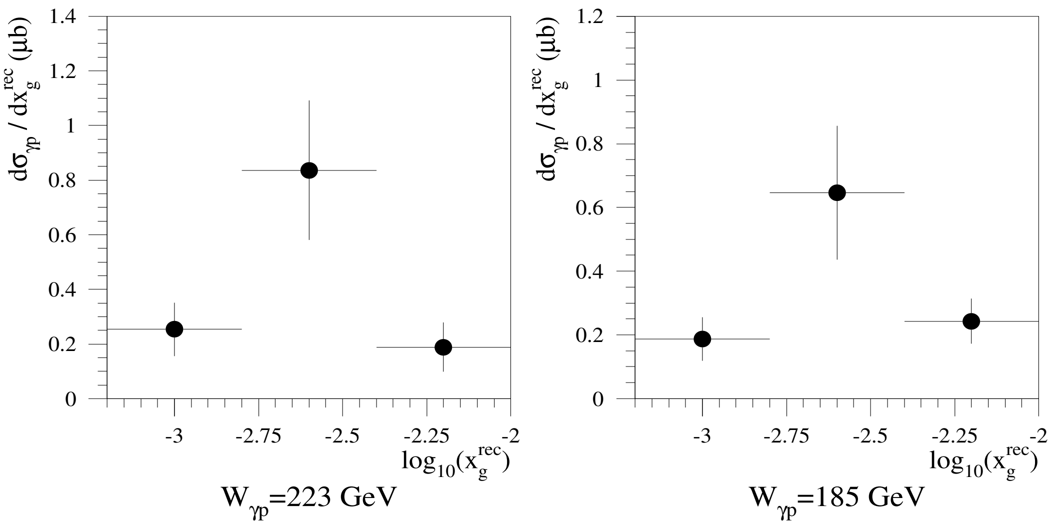

Figure 4.5: Measured differential cross sections $d\sigma^{vis}(\gamma p \to c\bar{c}X)/dx_g^{rec}$ at $\overline{W_{\gamma p}} = 223\ GeV$ (left figure) and $\overline{W_{\gamma p}} = 185\ GeV$ (right figure). The error bars are statistical errors only. A common systematic error of 15% is not shown.

$$\frac{d\sigma^{vis}(\gamma p \to c\bar{c}X)}{dx_g^{rec}} = \frac{1}{2\ Br(c \to D^* \to K\pi\pi)\ \epsilon_{trig}\ \epsilon_{rec}\ F_{\gamma/e}\ L}\frac{dN(D^* \to K\pi\pi)}{dx_g^{rec}} \tag{4.7}$$

where the abbreviations have the following meaning:

- $Br(c \to D^* \to K\pi\pi) = (7.1 \pm 0.5) \cdot 10^{-3}$ [33]
- ϵ_{trig} and ϵ_{rec}: Trigger and reconstruction efficiencies as determined with Monte Carlo simulations. They are listed in the appendix.
- $dN(D^* \to K\pi\pi)/dx_g^{rec}$: Number of reconstructed events in the various bins of x_g^rec (determined by the fit)
- $F_{\gamma/e}$: Photon flux in the Weizsäcker-Williams approximation.
  - In $0.02 \le y \le 0.32$ ($\overline{W_{\gamma p}} = 88\ GeV$): $F_{\gamma/e} = 8.38 \cdot 10^{-2}$
  - In $0.29 \le y \le 0.5$ ($\overline{W_{\gamma p}} = 185\ GeV$): $F_{\gamma/e} = 9.84 \cdot 10^{-3}$

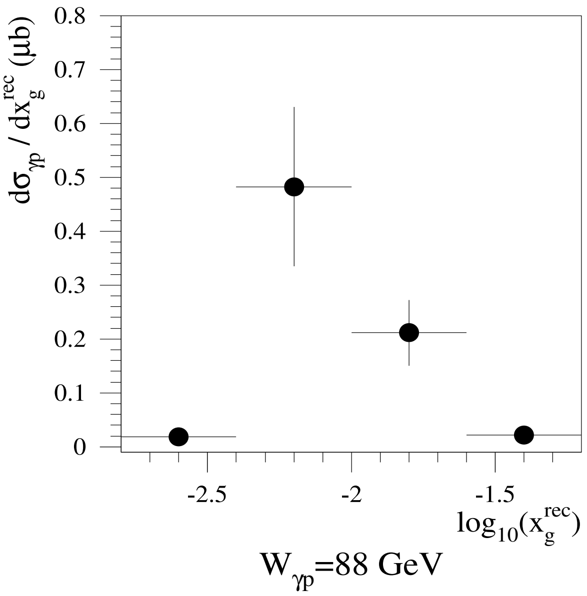

Figure 4.6: Measured differential cross sections $d\sigma^{vis}(\gamma p \rightarrow c\bar{c}X)/dx_g^{rec}$ at $\overline{W_{\gamma p}} = 88\ GeV$. The error bars are statistical errors only. A common systematic error of 15% is not shown.

– In $0.5 \leq y \leq 0.62$ ($\overline{W_{\gamma p}} = 223\ GeV$): $F_{\gamma/e} = 2.99 \cdot 10^{-3}$

The systematic errors are the same as described for the single inclusive spectra on page 55 and add up (quadratically) to 15%.

Resolved Photon Background The analysis cuts in η have been chosen to strongly reduce the influence of the hadronic part of the photon. As explained in detail in chapters one and three, the biggest contribution is found at the highest photon-proton centre of momentum energy since the photon parton density functions are very soft. A calculation of the direct and resolved parts separately reveals, that at $W_{\gamma p} = 88\ GeV$ the hadronic fraction of the cross section is less than 3% in all bins of x_g^{rec}, while at $W_{\gamma p} = 185\ GeV$ and at $W_{\gamma p} = 223\ GeV$ it is less than 5% with the most pessimistic choice of the photon structure function LAC1 combined with MRS(G) for the proton. It will be treated as an asymmetric systematic error of the mentioned size and not considered any more in the following.

4.1.2 Unfolding

The inclusion of radiative corrections is done by unfolding the measured cross section $d\sigma/dx_g^{rec}$ to the "true" values $d\sigma/dx^{gen}$ using the massive scheme QCD calculation. The unfolding matrices together with the calculated scales μ_F are shown in figs. 1.3, 4.8 and 4.9. The calculation used to obtain the shown results is characterized as follows:

- Massive scheme NLO QCD calculation [14] (in the double differential mode). Direct part only.
- Fragmentation of the charm quark into the D^* is simulated with the PSSZ-fragmentation function with $\epsilon = 0.035$.
- Proton parton density parametrization: MRS(A')
- Standard scales for the double differential cross sections: $\mu_R = \sqrt{m_c^2 + (p_t(c)^2 + p_t(\bar{c})^2)/2}$ and $\mu_F = 2\ \mu_R$

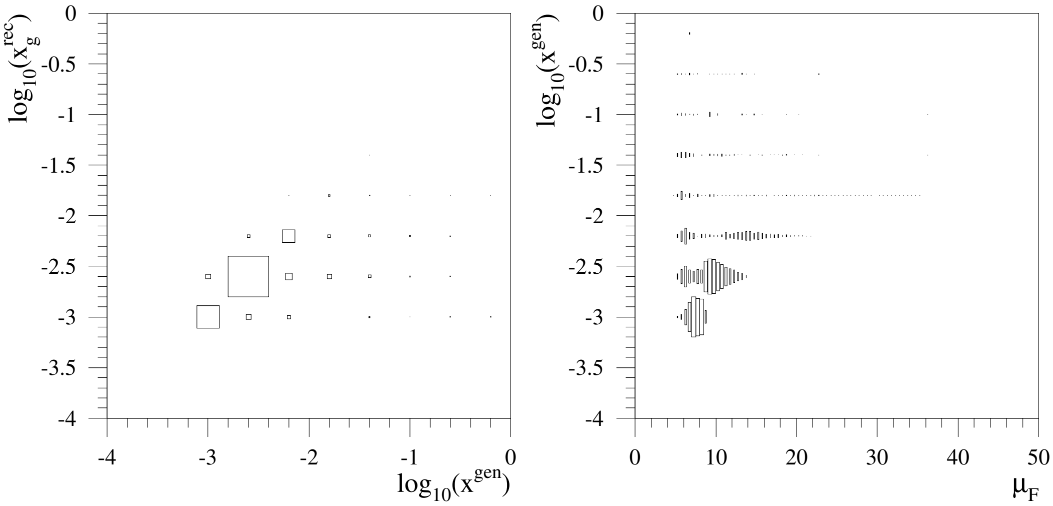

Figure 4.7: Left: Matrix used to unfold from the measured cross section $d\sigma/dx_g^{rec}$ at $W_{\gamma p} = 223\ GeV$ to the cross section in bins of x^{gen}. The calculation is described in the text. Right: Correlation of the factorization scale μ_F and the generated value of x as obtained with the same calculation.

The necessary cuts on η_{D^*} allows only to probe two bins in x_g^{rec} at 88 GeV and the corresponding unfolding matrix is therefore very peaked in these two bins in x_g^{rec}. The unfolding itself is done using an iterative procedure based on Bayes' theorem [71]. Since the unfolding matrix is calculated from the QCD calculation with high numerical precision, the unfolding procedure itself is nearly free of errors. Numerical tests show that "true" distributions which are smeared with the unfolding matrix are recovered within less than 3%. Certainly the whole unfolding procedure depends crucially on the parameters used in the calculation and a variation of the important parameters (μ_R, $\epsilon_{Peterson}$, parton density function) will determine the systematic error discussed later.

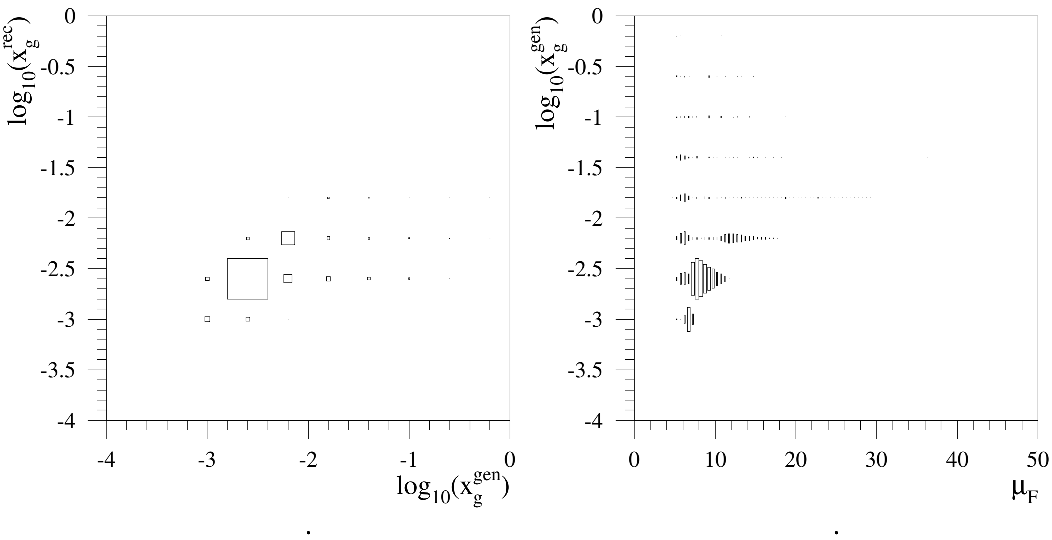

Figure 4.8: Left: Matrix used to unfold from the measured cross section $d\sigma/dx_g^{rec}$ at $W_{\gamma p} = 185\ GeV$ to the cross section in bins of x^{gen}. Right: Correlation of the factorization scale μ_F and the generated value of x.

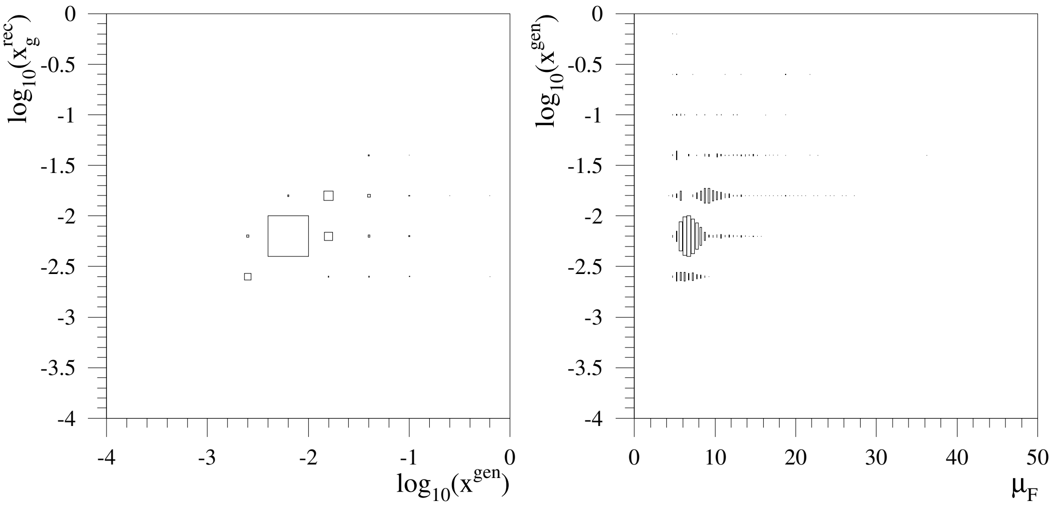

Figure 4.9: Left: Matrix used to unfold from the measured cross section $d\sigma/dx_g^{rec}$ at $W_{\gamma p} = 88\ GeV$ to the cross section in bins of x^{gen}. Right: Correlation of the factorization scale μ_F and the generated value of x.

4.1.3 Subtraction of the Quark Contribution

A certain fraction of the now determined cross sections $d\sigma^{vis}_{\gamma p\to c\bar{c}X}/dx^{true}$ is due to processes with a quark in the initial state which need to be considered as background. The relative contribution of $\gamma q \to c\bar{c}X$ to all subprocesses is shown in fig. 4.10. It

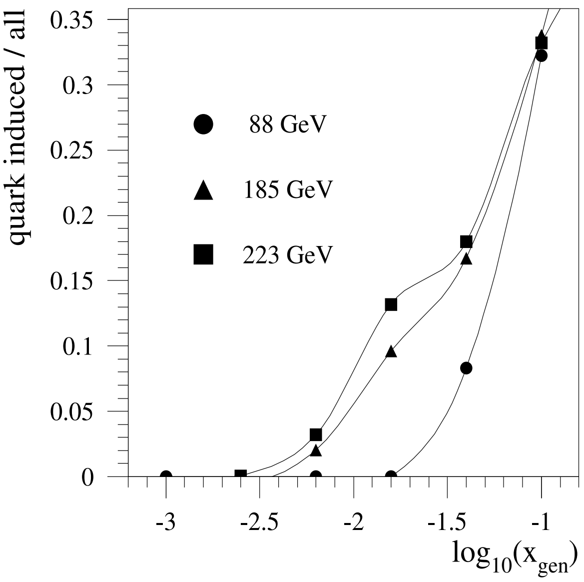

Figure 4.10: Relative size of the quark induced processes $\gamma q \to c\bar{c}X$ to all subprocesses for the visible cross section in bins of x^{gen}.

is larger at higher $W_{\gamma p}$ and steeply growing with x. This fraction is subtracted from the unfolded cross section to yield finally the wanted $d\sigma^{vis}_{\gamma p\to c\bar{c}X}/dx_g^{true}$. The dependence of the calculated fraction on the specific parton density function used will be a part of the systematic error.

4.1.4 Measurement of the Gluon Density

By dividing the measured und unfolded cross section $d\sigma^{vis}_{\gamma p\to c\bar{c}X}/dx_g^{true}$ by the partonic cross sections $d\hat{\sigma}^{vis}_{\gamma g\to c\bar{c}X}(\hat{s},\mu_F)/dx_g$, the gluon density $f_{g/p}(x_g,\mu_F^2)$ is obtained and shown in fig. 4.11 as a function of μ_F^2. Different markers correspond to different values of $\overline{x_g}$. The quoted values are bin center corrected. The inner error bars are the statistical errors originating from the determination of the number of D^*. They are propagated using the unfolding matrix. The middle error bars show the most important systematic theoretical error, the dependence upon the renormalization scale μ_R, which is calculated by varying μ_R by a factor of 2 in all calculations . The outermost error bars are obtained by varying $\epsilon_{Peterson}$ from 0.025 to 0.045. A detailed discussion of all the systematic errors follows below.

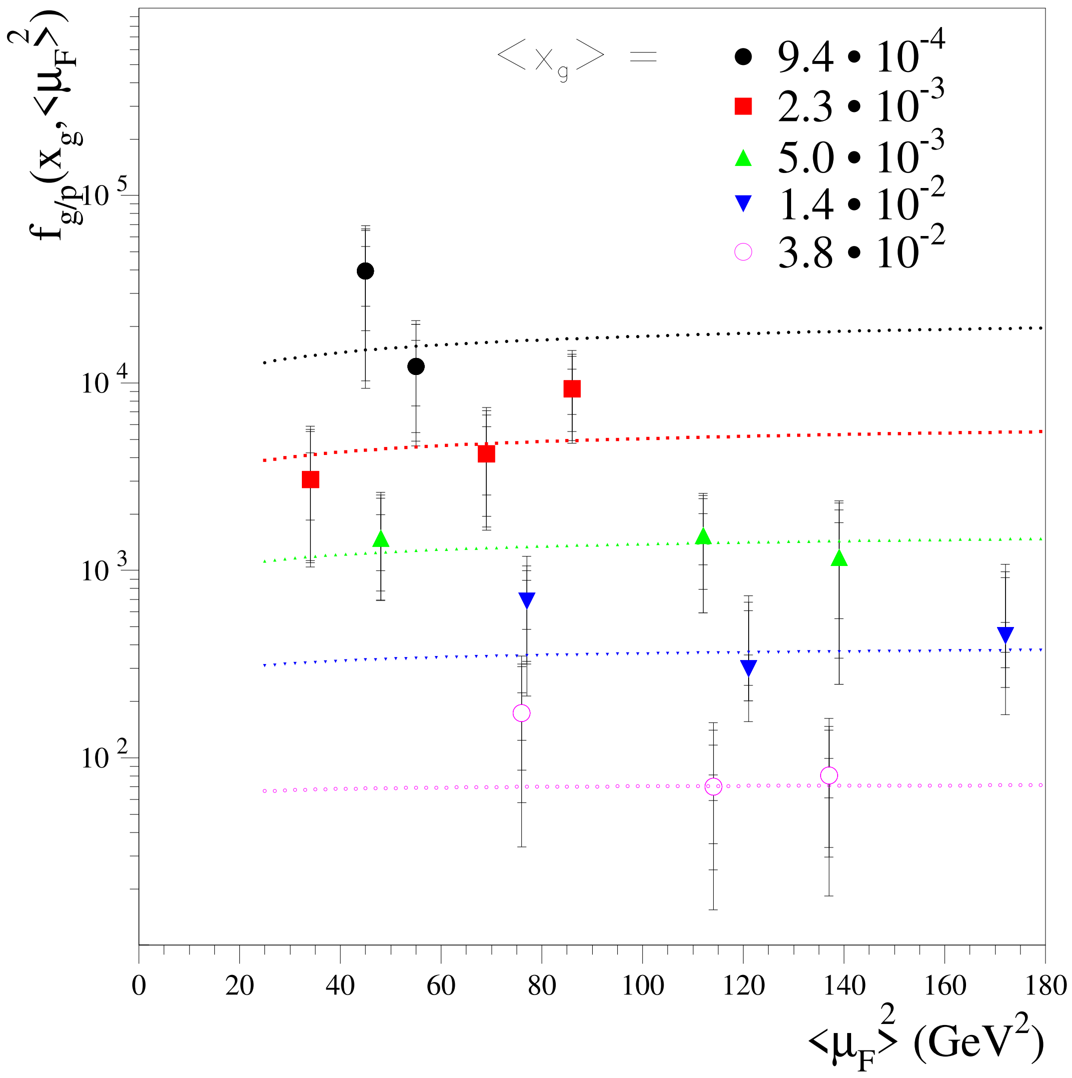

Figure 4.11: Measured gluon density of the proton $f_{g/p}(x_g, \mu_F^2)$ as a function of μ_F^2. The various markers correspond to the values of x_g given in the upper right corner. The innermost error bars are the statistical errors, the second error bars are the systematic error from the scale dependence and the third errors are obtained by the variation of $\epsilon_{Peterson}$ as described in the text and the outermost errors are from the resolved photon and the choice of the structure function. All errors are added linearly. The four measured points in the lower right corner are only indirectly determined. The dotted lines are the prediction of the MRS(A') parametrization.

4.1.5 Measurement of the Gluon Density at an Average Scale

To obtain a measurement of $f_{g/p}(x_g, \mu_F^2)$ as a function of x_g at an average scale, the measured points need to be propagated in μ_F. This is done by assuming that the measured gluon density has the same dependence upon the factorization scale as a certain parametrization, say MRS(A'). Since this dependence is given by the Altarelli-Parisi equation, it is very similar for all the parametrizations and the error introduced by choosing a specific parametrization is small (see next section). Fig.

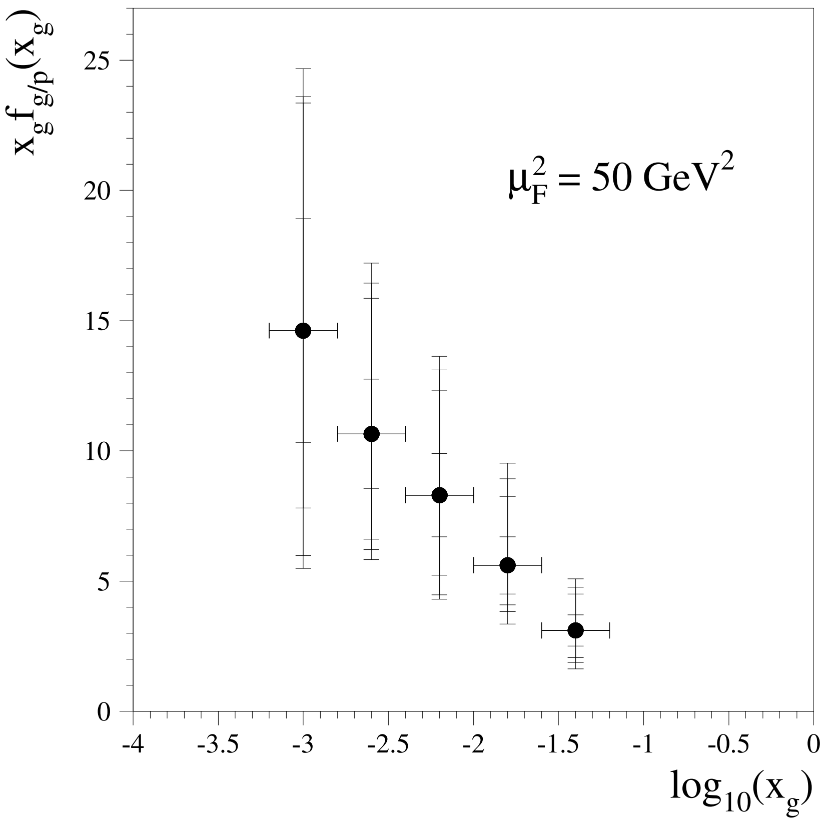

Figure 4.12: Measured gluon density at an average scale $\mu_F^2 = 50\ GeV^2$. The innermost error bars are the statistical errors, the second error bars are the dependence upon the renormalization scale μ_R as obtained by varying μ_R by a factor of two. The third errors describe the uncertainty from $\epsilon_{Peterson}$ and the outermost error bars show the dependence upon the choice of the structure function used for the unfolding and the resolved photon contribution. Not included ist the experimental systematic error of 15%.

4.12 shows the obtained gluon density at an average $\mu_F^2 = 50\ GeV^2$. The several measurements from fig. 4.11 corresponding to the same x_g are combined taking the statistical error into account.

4.1.6 Systematic Errors

All sources of systematic errors are shown in fig. 4.13. The *experimental* systematic (labeled "exp. sys." in the figure) errors are the same for the measurement of the gluon density as for the measurement of the single inclusive D^* cross sections and are explained on page 55. They add up to 15%. The following theoretical errors are considered:

- **Scale uncertainty** ("scale dep."). The dependence of the unfolding matrix and the partonic cross sections upon the renormalization scale μ_R gives the largest systematic uncertainty. It is of the order of $^{+30}_{-20}\%$ for the bins in x_g which are measured directly and larger for the two remaining bins at higher x_g which are only accessed via QCD radiative events. Since the renormalization scale $\mu_R = \sqrt{m_c^2 + p_t^2}$ is directly coupled to the charm quark mass, the quark mass is not varied separately.

- **Contribution of the resolved photon component** ("resolved"). It is of the order of 0.1% to 5% in all bins of x_g and at all three $W_{\gamma p}$, strongly depending on the photon parton density function used, but never exceeding 5%. A systematic error $^{+4}_{0}\%$ is assumed.

- **Fragmentation function** ("ϵ_{Pet}"). The fragmentation of charm quarks into D^*-mesons is parametrized by the PSSZ-fragmentation function and this parametrization describes the ARGUS measurements [72] ($E = 10\ GeV$) very well. The uncertainty in the fitted parameter $\epsilon = 0.035$ [16] is of the order of ± 0.01 and results in a systematic error of 2% to 15%. It is growing with increasing x_g. The error is estimated by redoing the full calculation with $\epsilon = 0.025$ and $\epsilon = 0.045$ respectively.

- **Structure functions** ("evolution" and "struct. fun."). The error introduced by the choice of a specific structure function for the calculation of the unfolding matrix and the evolution of the measured gluon density to the average scale 50 GeV^2 is estimated by comparing the results obtained with MRS(A') and MRS(G). These two parametrizations of the proton structure function have quite different gluon densities. Only for the two bins in x_g which are determined mainly with radiative events, the dependence upon the structure function is relevant and reaches 15%.

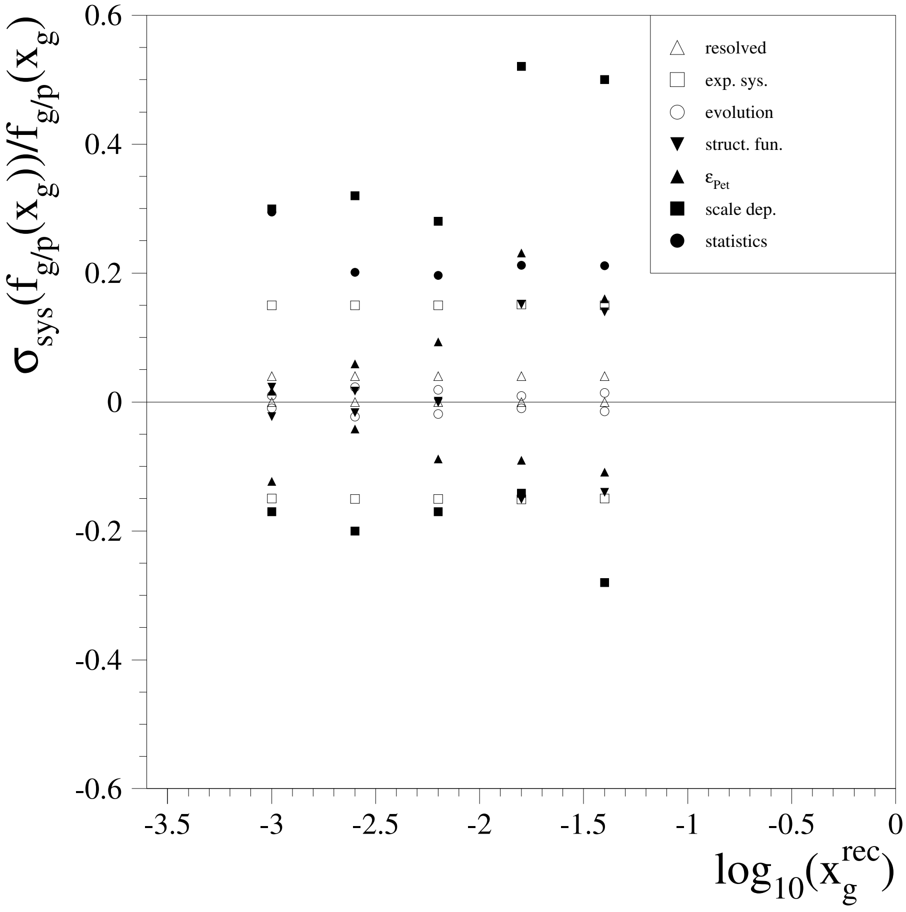

Figure 4.13: Overview over the systematic uncertainties as a function of x_g. The abbreviations are explained in the text.

4.1.7 Comparison to Previous Measurements

The measured gluon density is compared to two previous determinations at HERA: The leading order, direct determination from (2+1)-jet rates in deep inelastic scattering [44], and the NLO, indirect determination from scaling violations of the proton structure function F_2 [35]. The measured values are evolved to the scales 20 GeV^2 and 30 GeV^2 respectively. Excellent agreement is found between the determination from the jet rates and this analysis. The accessible range in x_g has been enlarged with this measurement by half an order of magnitude down to $x_g = 0.001$ (fig. 4.14). The steep rise of the gluon density towards low x which has been expected from the indirect, NLO determination from scaling violations of F_2 (fig. 4.15) can be confirmed.

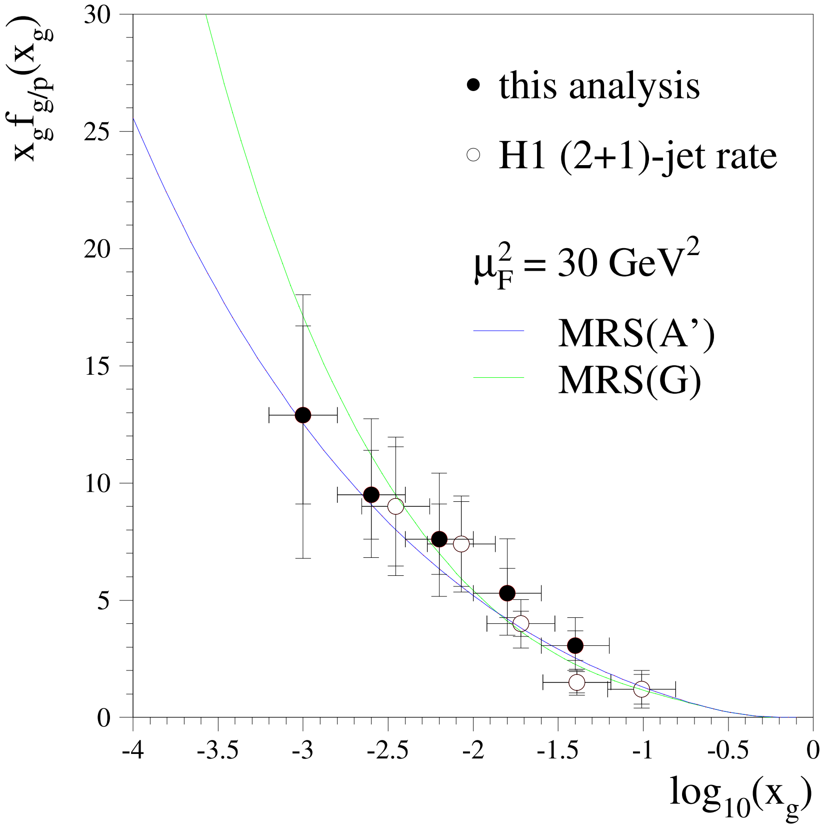

Figure 4.14: Comparison of the measured gluon density to the LO determination from the (2+1)-jet in deep inleastic scattering. In both cases, an overall normalization uncertainty of 12% (jet-rates) and 15.5% (this analysis) is not shown. The inner error bars are the statistical error only and the outer error bars are the systematic errors (added linearly). Scale uncertainties are not given in the jet-rate analysis and can not be compared.

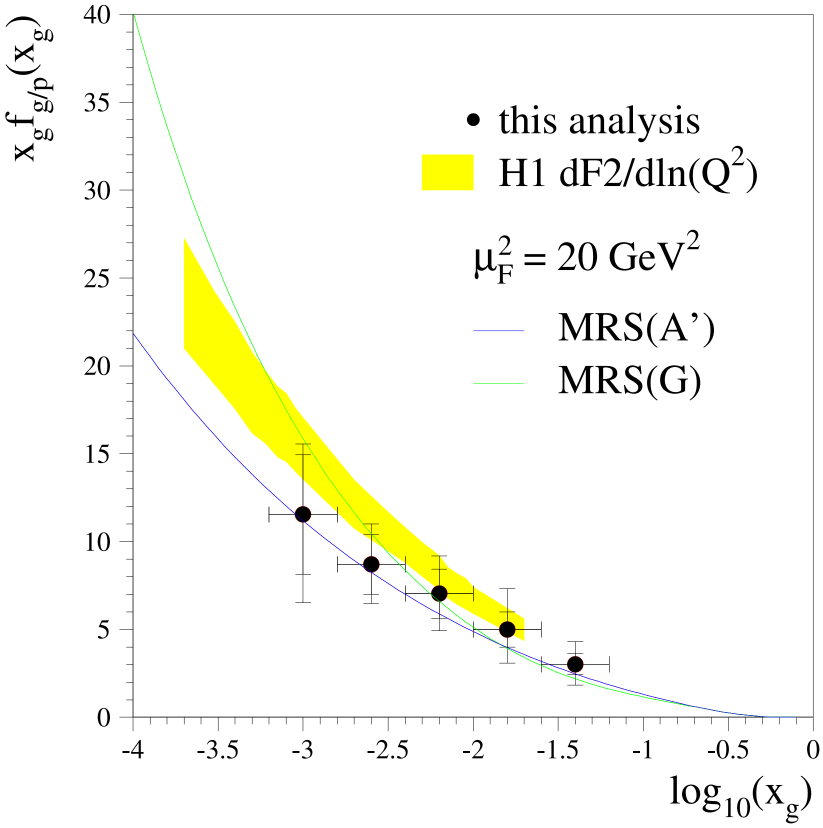

Figure 4.15: Comparison of the measured gluon density with the determination from scaling violations of F_2. The inner error bars are the statistical errors only and the outer errors are the systematic errors (without scale dependence and exp. sys. errors).

4.2 Jacquet-Blondel Method

As a cross check of the obtained results, a second method to reconstruct the momentum fraction x_g is used in this section.

4.2.1 Description of the Method

In the absence of initial state radiation, the conservation of energy and longitudinal momentum implies for the production of a charm quark pair plus any number of other particles (in γp-collisions)

$$x_g E_p + E_\gamma = E_c + E_{\bar{c}} + \sum_i E_i \tag{4.8}$$

$$x_g P_p^l - E_\gamma = P_c^l + P_{\bar{c}}^l + \sum_i P_i^l, \tag{4.9}$$

where E_i and P_i stand for the energy and momentum of the additional particles in the final state. Adding yields (assuming that $E_p = P_p^l$):

$$x_g = \frac{E_c + E_{\bar{c}} + P_c^l + P_{\bar{c}}^l + \sum_i (E_i + P_i)}{2\ E_p}. \tag{4.10}$$

If the particles originating from the hard interaction would fragment independently from the proton remnant, the formula would easily survive the fragmentation process since the sums of energy and momentum are conserved in the fragmentation:

$$x_g = \frac{\sum_{c\bar{c}-system}(E + P^l)}{2\ E_p}. \tag{4.11}$$

By interchanging the role of the gluon and the photon one gets the well known Jacquet-Blondel equation:

$$y = \frac{\sum_{c\bar{c}-system}(E - P^l)}{2\ E_e}. \tag{4.12}$$

The difference between the two cases is that for the reconstruction of y the separation of the $c\bar{c}$-system is not important since particles in the very forward direction have $E \approx P^l$ and do not contribute to the sum (and actually the sum is therefore usually extended to all particles in the final state), while in the case of x_g the opposite holds. The basic question which needs to be addressed is therefore if and how the proton remnant can be separated from the final state particles of the hard interaction. Clearly this is not exactly possible, the region between the charm quarks and the remnant is populated by particles from the fragmentation (as the measurements described in chapter three have shown) and there is a certain exchange of momentum and energy between the remnant and the charm quarks during the fragmentation process. The more transverse momentum the charm quarks have and the larger the pseudorapidity-difference between the charm system and the remnant, the easier the task gets. For the events analysed in the energy flow measurement, the following method works:

Decomposition of the Event As was shown in the last chapter, the energy flow in charm events is reliably described up to $\tilde{\eta} \approx 1 - 1.5$ for the analysed phase space ($p_t(D^*) \geq 2.5\ GeV, -1.5 \leq \eta(D^*) \leq 0$ and $\overline{W_{\gamma p}} = 194\ GeV$). For these events, the second charm quark has in 98% of the cases a pseudorapditity $\tilde{\eta} \leq 1.4$ (according to the MC). So, to get rid of the proton remnant, a simple cut at $\tilde{\eta} = 1.4$ is enough. At the same time, the region where the MC only poorly describes the data

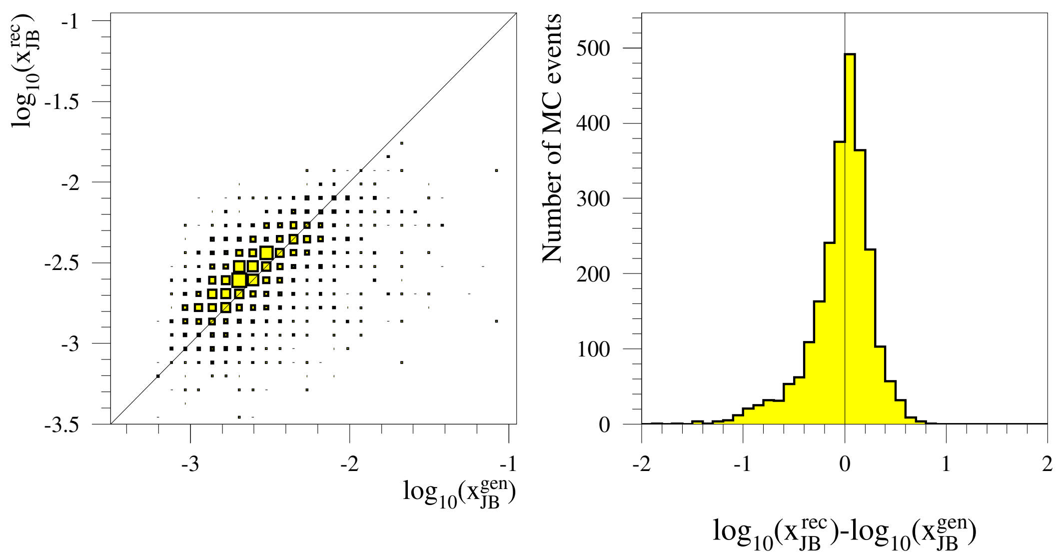

Figure 4.16: Correlation between the reconstructed x_{JB}^{rec} and the generated x_{JB}^{gen} in MC (AROMA) for events with a reconstructed D^* in the kinematical region described in the text and with $0.29 \leq y \leq 0.62$ ($\overline{W_{\gamma p}} = 194\ GeV$). The quantity x_{JB}^{gen} is calculated by applying the same algorithm on parton level as for the reconstructed tracks and clusters. The peak position in the right histogram shows a systematic shift of 6%.

is removed. But this is unfortunatly not enough to get an accurate reconstruction of x_g. The particles with $\tilde{\eta} \leq 1.4$ from the fragmentation of the strings between the charm quarks and the remnant need to be assigned to the $c\bar{c}$-system or the remnant depending on whether they are closer to one or the other. To perform this task, the event was decomposed into three parts using the clustering algorithm LUCLUS [62]. Input to the algorithm are all particles which survived the $\tilde{\eta}$-cut and an artificial pseudo-remnant. Clustering proceeds until only three clusters are left. The two clusters not containing the pseudo-remnant are the $c\bar{c}$-system. It is important to notice that it does not make a difference if a certain particle is assigned to one or the other cluster for the reconstruction of x_{JB}^{rec}, which is defined as the Jacquet-Blondel sum over all particles (tracks and clusters) in the determined $c\bar{c}$-system. The only thing which matters is what is assigned to the remnant. The LUCLUS distance measure is

$$R^2 = 2\,\frac{\vec{p_1}^{\,2}\vec{p_2}^{\,2}}{(|\vec{p_1}| + |\vec{p_2}|)^2}\,(1 - \cos(1,2)). \tag{4.13}$$

The momentum of the pseudoremnant needs to be of the same order as the momentum of the charm quarks and was set to 4 GeV. The procedure is now the following: First, the data sample of the e-tagger at -33 m is splitted into two parts like in the previous method, again to ensure the validity of the approximation discussed on page 12. The number of D^* in the selected phase space are determined in bins of x_{JB}^{rec}. Then the observed number of events is unfolded to the number of events in x_{JB}^{gen} by using the migration matrix given by MC. This takes all detector effects into account. Then the cross sections in bins of x_{JB}^{gen} are derived and the radiative corrections due to initial state radiation and quark induced processes are taken into account similarly to the previous section. And finally the results are compared with the measurement using the D^*-method.

4.2.2 Determination of the Number of D^*

Data Selection The same data from the years 1994 to 1996 as for the single inclusive cross sections is analysed, corresponding to an integrated luminosity of $L = 10.7\ pb^{-1}$. Only events triggered by subtrigger 83 (e-tagger at -33 m) are used and the following cuts on the D^*-candidates are applied:

- $-1.5 \leq \eta(D^*) \leq 0$
- $p_t(D^*) \geq 2.5\ GeV$
- $p_t(\pi, K) \geq 500\ MeV$, $p_t(\pi_s) \geq 150\ MeV$
- D^0 mass window: $\pm 80\ MeV$.

The binning in x_{JB}^{rec} has been chosen to be the same as in the last section. For both samples at 185 GeV and at 223 GeV, in the two lowest bins in x_{JB}^{rec} a significant D^*-signal is visible. The signals are shown in figs. 4.17 and 4.18.

Number of Events The number of events is determined in the usual way with the method of the equivalent number of events, except for the lower bin at 223 GeV, where the number of D^* is determined by fitting the background with a constant and counting the number of entries above the background in the three bins closest to the nominal value of Δm:

	223 GeV	185 GeV
$-3.2 \leq \log(x_{JB}^{rec}) \leq -2.8$	11.9 ± 4.6	26.4 ± 12.6
$-2.8 \leq \log(x_{JB}^{rec}) \leq -2.4$	46.6 ± 14.4	119.5 ± 38

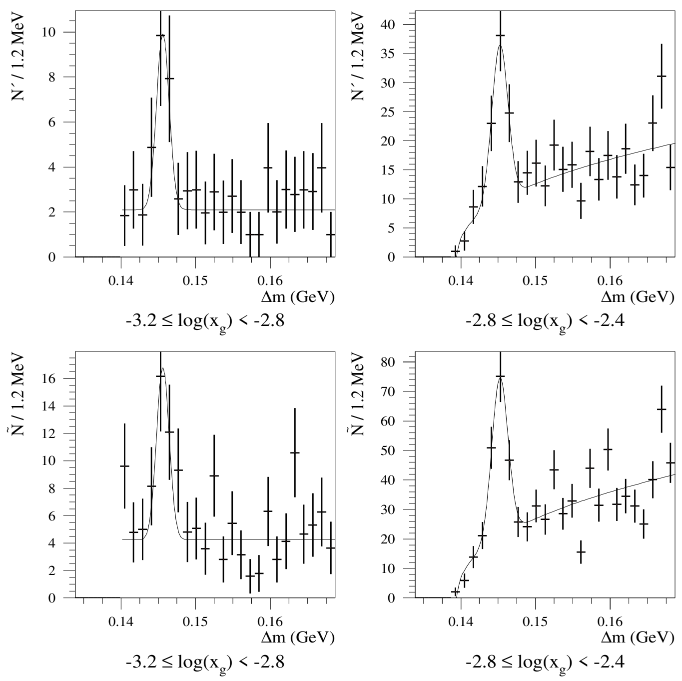

Figure 4.17: Δm-histograms for the data sample at 185 GeV. Upper row: Equivalent number of events (N'). Lower row: Weighted number of entries ($\tilde{N}$).

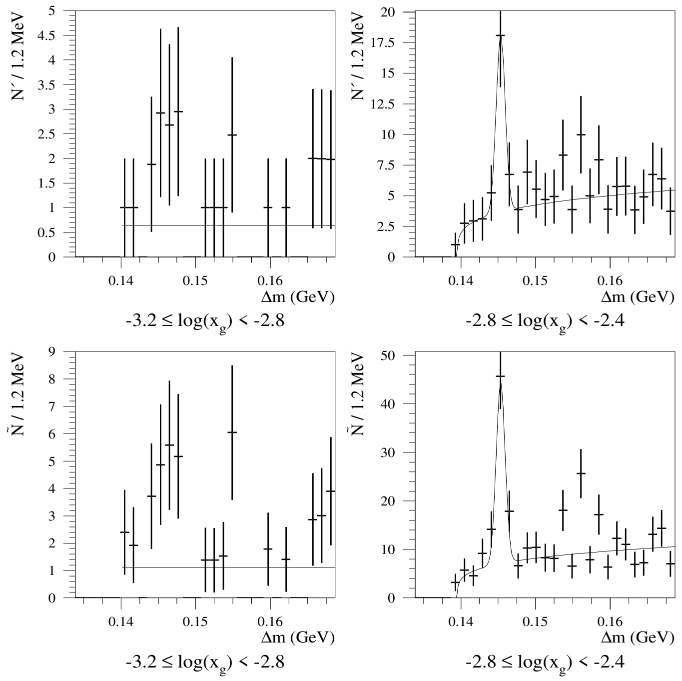

Figure 4.18: Δm-histograms (upper row: N', lower row: $\tilde{N}$) for the data sample at 223 GeV. The number of events in the lower bin in x_g (left) is not determined by fitting but by counting and therefore only the fit of the background is shown.

4.2.3 Unfolding to the Partonic x_{JB}

The unfolding matrices are shown in fig. 4.19. Since the resolution in x_{JB} is quite poor compared to the D^*-method, this unfolding step introduces large errors. The unfolding is done using the same technique as in the previous case [71], taking the MC statistics fully into account. The statistical error on the number of events is propagated using the covariance matrix given by the method. As can be immediately seen by looking at the figure, the higher bin is much less affected by migrations than the lower bin in x_{JB}. Since the result of the unfolding is very sensitive to the relative

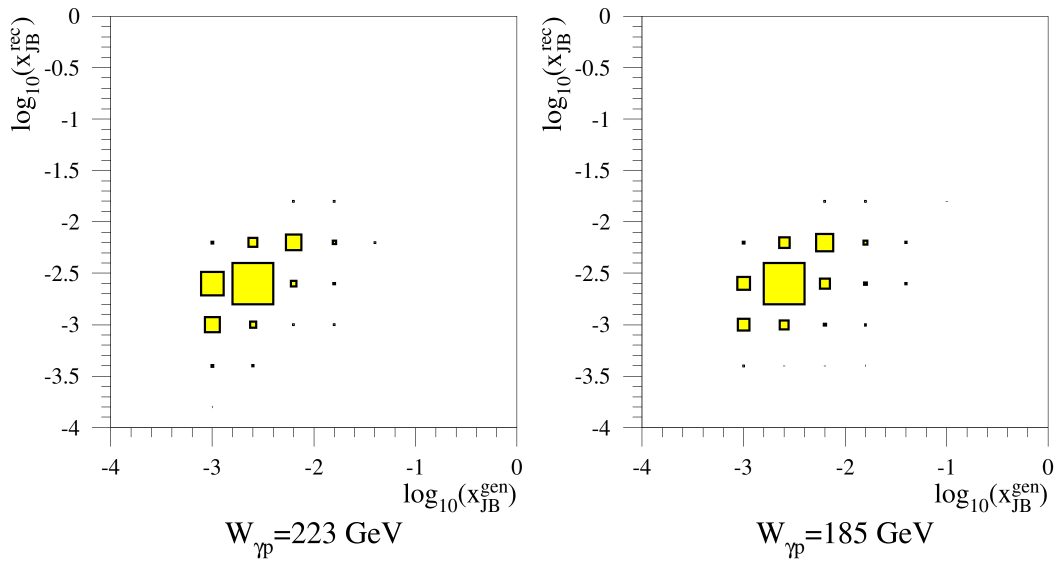

Figure 4.19: Correlation matrices for the unfolding step from x_{JB}^{rec} to x_{JB}^{gen}, as obtained from the MC simulation (AROMA).

size of the two measured numbers of events in the two bins in x_{JB}^{rec} (for both energies), the reconstructed number of events need to be corrected for the trigger efficiency, since this effect is not included in the MC simulation and the efficiencies in the two bins differ by about 8%. The following unfolded number of D^* have been obtained:

	223 GeV	185 GeV
$-3.2 \leq \log(x_{JB}^{gen}) \leq -2.8$	16.9 ± 8.8	24.3 ± 16.6
$-2.8 \leq \log(x_{JB}^{gen}) \leq -2.4$	39.1 ± 16.4	120 ± 48

Using the reconstruction efficiencies listed in the appendix, the differential cross sections in x_{JB}^{gen} are derived:

	223 GeV	185 GeV
$-3.2 \leq \log(x_{JB}^{gen}) \leq -2.8$	$0.347 \pm 0.183\ \mu b$	$0.122 \pm 0.083\ \mu b$
$-2.8 \leq \log(x_{JB}^{gen}) \leq -2.4$	$0.443 \pm 0.19\ \mu b$	$0.456 \pm 0.183\ \mu b$

4.2.4 Inclusion of Radiative Corrections

The inclusion of radiative correction poses no problem. It is also done by unfolding of the measured cross sections in bins of x_{JB}^{gen} to x_{true} with the correlation matrix given by the massive scheme NLO QCD calculation. The quantity x_{JB}^{gen} in the MC is identified with the corresponding variable in the QCD calculation, namely the quantity which is also obtained by applying the event decomposition with the LUCLUS algorithm. In the case of the QCD calculation the result is quite trivial since there are at most three particles in the final state and usually one finds $x_{JB}^{gen} = x_{true}$, except for the events with initial state radiation (fig. 4.20). Again, the bins

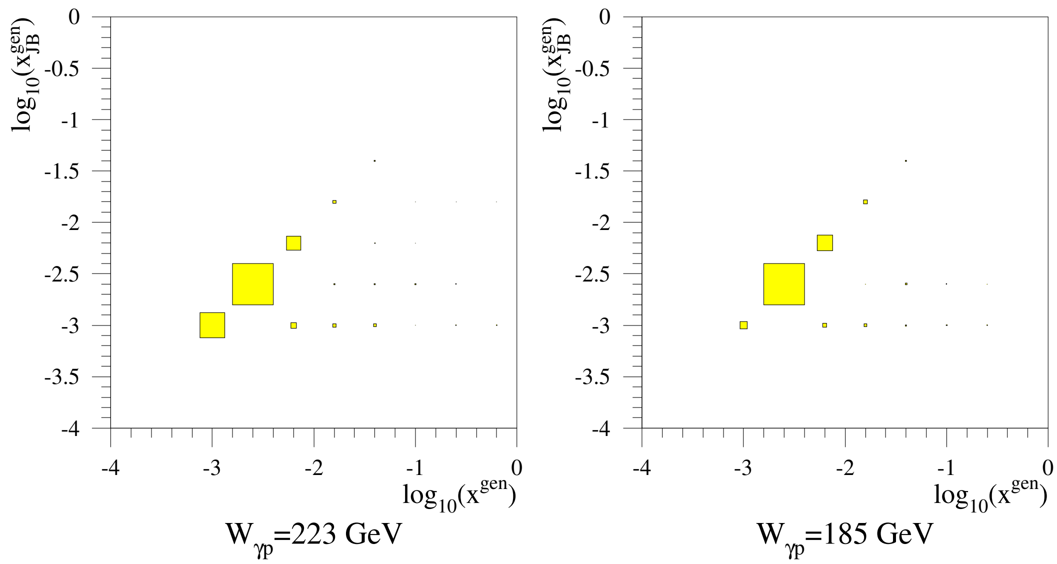

Figure 4.20: Unfolding matrix for the inclusion of the radiative corrections as obtained from the NLO QCD calculation in the massive scheme.

corresponding to the lower values of x_{JB}^{gen} obtain large corrections. The unfolded cross sections after the subtraction of the quark induced processes are

	223 GeV	185 GeV
$-3.2 \leq \log(x_g^{true}) \leq -2.8$	$0.331 \pm 0.175\ \mu b$	$0.052 \pm 0.035\ \mu b$
$-2.8 \leq \log(x_g^{true}) \leq -2.4$	$0.436 \pm 0.187\ \mu b$	$0.434 \pm 0.174\ \mu b$

By dividing these determined cross sections by the (in NLO) calculated partonic cross sections one gets finally the gluon density

	223 GeV	185 GeV
$-3.2 \leq \log(x_g) \leq -2.8$	22370 ± 11841	8879 ± 5976
$-2.8 \leq \log(x_g) \leq -2.4$	5742 ± 2463	4396 ± 1762

4.2.5 Comparison with the D^*-Method

The results of the two methods are shown in fig. 4.21. Fair agreement is found for three of the four measured data points. The point corresponding to the lower x_g and to the lower factorization scale is off.

This point is the most difficult to measure in both methods. Since it is the bin with the lowest values of x_g and μ_F, it corresponds to the events with the lowest p_t and the highest η of the D^*. And for these events the separation of the proton remnant is most difficult in the Jacquet-Blondel method. As can be seen in the figure, this data point also gets by far the largest dependence on $\epsilon_{Peterson}$ in the D^*-method.

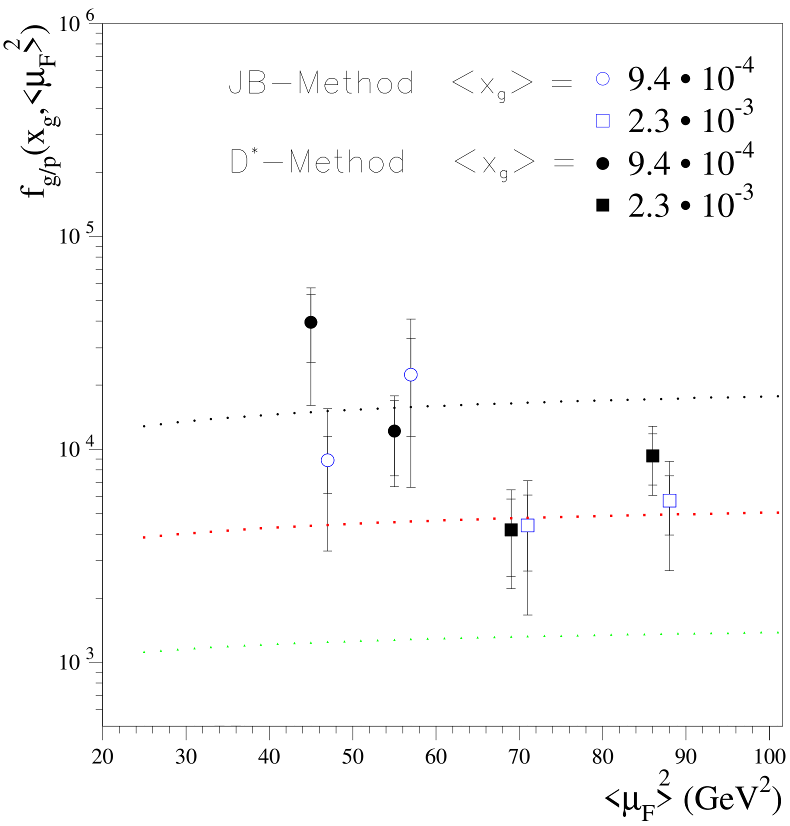

Figure 4.21: Comparison of the results of the D^*-method (full markers) and the Jacquet-Blondel method (open markers). The latter have been shifted in μ_F by 2 GeV^2 to allow a better visual comparison of the error bars. The inner error bars correspond in both cases to the purely statistical error from the number of measured events. For the D^*-method, the outer error bars stand for the linearly added error from the variation of $\epsilon_{Peterson}$ and for the JB-method they represent the errors introduced by the MC-unfolding. Common systematic errors like the experimental systematic error or the scale dependence are not shown.

Summary and Outlook

A measurement of the single inclusive D^*-cross sections in the variables η and p_T in tagged photoproduction at $\overline{W_{\gamma p}} = 88\ GeV$ and $\overline{W_{\gamma p}} = 194\ GeV$ has been presented. It has been shown that both the shape and the normalization are in fair agreement with calculations in perturbative QCD in the massive scheme. The energy flow in events with a reconstructed D^* in $-1.5 \leq \eta \leq 0$ at $\overline{W_{\gamma p}} = 194\ GeV$ has been measured and confirmed the expectation of the Monte Carlo (AROMA) simulation for the energy flow originating from the charm quark pair. The obtained results indicate that (tagged) charm photoproduction is a reliable way to access the gluon content of the proton.

A direct and NLO determination of the gluon density $f_{g/p}(x_g, \mu_F^2)$ in the proton has then been performed in the second part of this analysis. By measuring the differential cross section $d\sigma^{vis}_{\gamma p \to c\bar{c}X}/dx_g$ at three photon-proton center of mass energies ($\overline{W_{\gamma p}} = 88\ GeV$, $\overline{W_{\gamma p}} = 185\ GeV$ and $\overline{W_{\gamma p}} = 223\ GeV$), the range $0.001 \leq x_g \leq 0.04$ and $30\ GeV^2 \leq \mu_F^2 \leq 175\ GeV^2$ was probed.

The reconstruction of x_g was based on the measured D^*-meson. QCD radiative corrections have been fully taken into account by unfolding the measured cross section in x_g^{rec} to the "true" values using a NLO QCD calculation. The systematic errors from the scale dependence of the partonic cross sections and the dependence upon the fragmentation function are of similar size as the statistical errors.

To cross check the measurement, a different method to reconstruct x_g relying on the hadronic final state instead of the D^* has been used. Except for one bin, the results of both methods are the same within the errors.

The obtained results were compared to previous indirect or leading order determinations from scaling violations of F_2 and (2+1)-jet production in deep inelastic scattering. Good agreement was found with the jet-rate analysis confirming the steep rise of the gluon density down to $x_g = 0.001$. The measured $f_{g/p}(x_g, \mu_F^2)$ shows within the still large errors the expected dependence upon the factorization scale μ_F.

An improvement of the present precision in the determination of the gluon density with charm could be achieved by reducing the statistical error (higher integrated luminosity), the scale uncertainty (improvement in the QCD calculation) and the uncertainty from the fragmentation.

Both higher statistics and a smaller dependence on the fragmentation model will be obtained in the future by tagging charm and beauty jets with the new silicon vertex detector. High precision measurements of single and double differential cross sections in p_t and η of charm mesons and charm jets will provide further insights in the production mechanism. It will also be possible to directly measure the fragmentation function of heavy quarks.

To access significantly lower values of x_g, a higher $W_{\gamma p}$ is needed. A lifetime tag would help in this case to reduce the strongly increasing combinatorial background.

Other important topics which can be addressed with the higher luminosity in the future are a precision measurement of the heavy quark inclusive structure function $F_2(x, Q^2)$ for charm and beauty, which is very sensitive to the gluon density at small x, and also differential b cross sections.

Appendix A

In this appendix, a short description of the Weizsäcker-Williams approximation is given which follows closely [2]. I start by writing the electroproduction cross section for a generic process with the positron e(p) and a massless hadron p(k) in the initial state and the scattered positron e(p') and a hadronic system X in the final state in leading order QED (Heaviside-Lorentz rationalized units):

$$d\sigma_{ep} = \frac{1}{8kp}\frac{e^2 W^{\mu\nu} T_{\mu\nu}}{q^4}\frac{d^3p'}{(2\pi)^3 2E'}. \tag{6.14}$$

The first and the last term are the particle flux and the phase space of the scattered positron and q denotes the exchanged momentum $q = p - p'$. The dynamics of the process is contained in the middle part, which is the spin-averaged matrix element squared. It is decomposed as a product of the positron tensor

$$T_{\mu\nu} = 4(\frac{1}{2}q^2 g_{\mu\nu} + p_\mu p'_\nu + p_\nu p'_\mu) \tag{6.15}$$

representing the square of the positron current (summed and averaged over all polarization states), and the hadron tensor $W^{\mu\nu}$ (in the most general form allowed by the conditions of Lorentz invariance, gauge invariance, hermiticity and CP conservation of the hadronic current):

$$W^{\mu\nu} = W_1(q^2, kq)(-g^{\mu\nu} + \frac{q^\mu q^\nu}{q^2}) - \frac{q^2}{(kq)^2}W_2(q^2, k\ q)(k^\mu - \frac{kq}{q^2}q^\mu)(k^\nu - \frac{kq}{q^2}q^\nu). \tag{6.16}$$

$W^{\mu\nu}$ has to be analytic at $q^2 = 0$ and therefore $\lim_{q^2\to 0} q^2 W^{\mu\nu} = 0$. This is the crucial point. The physical meaning is that σ_L vanishes as $q^2 =$ goes to zero, corresponding to the fact that real photons are purely transverse polarized [3]. This leads to

$$W_2(q^2, kq) \approx W_1(0, kq). \tag{6.17}$$

To get the cross section in terms of the variables q^2 and $y = \frac{kq}{kp}$, the contraction of the two tensors and the phase space of the scattered positron must be calculated:

$$d\sigma_{ep} = -\frac{\alpha_{em}}{2\pi}\frac{W_1(0, kq)}{4kp}\left\{\frac{2m_e^2}{q^4} + \frac{1 + (1-y)^2}{y^2 q^2}\right\} dq^2 dy. \tag{6.18}$$

The cross section for collisions of real photons with the same hadrons reads after a similar calculation

$$\sigma_{\gamma p}(q,k) = -\frac{g_{\mu\nu}W^{\mu\nu}}{8kq} = \frac{W_1(0,kq)}{4kq} = \sigma_{\gamma p}(y), \tag{6.19}$$

showing that the electroproduction cross section factorizes into the photoproduction cross section and a photon flux factor

$$d\sigma_{ep}(q^2,y) = \sigma_{\gamma p}(y) f_\gamma^{(e)}(y,q^2) \tag{6.20}$$

$$f_\gamma^{(e)}(y,q^2) = \frac{\alpha_{em}}{2\pi} y [\frac{2m_e^2}{q^4} + \frac{1+(1-y)^2}{y^2 q^2}] dq^2 dy. \tag{6.21}$$

For small scattering angles, y can be approximated as $y = \frac{kq}{kp} \approx \frac{E_\gamma}{E_e} = \frac{E_e - E'_e}{E_e}$ and therefore be determined by measuring the energy of the scattered positron only. H1 has two calorimeters for this purpose, the so-called electron-taggers. They are described in detail in chapter two. The scattering angle is not measured but the beam line restricts it to $\theta \leq \theta_{max} = 3.5\ (5)\ mrad$. We therefore have to integrate equation 6.21 over q^2, the integration bounds being given by y and the acceptance in θ. Expanding $q^2(y,\theta)$ in powers of θ results in

$$Q^2_{max} = E_e^2(1-y)\theta^2_{max} \tag{6.22}$$

$$Q^2_{min} = \frac{(ym_e)^2}{1-y}, \tag{6.23}$$

where $Q^2 = -q^2$ and terms of order $O(\theta^4)$ have been dropped. In the expression for Q^2_{max}, a term of the order of Q^2_{min} has also been neglected, since it is numerically very small in our case. Performing the integration in q^2, we end up with the formula I will use:

$$d\sigma_{ep\to eX}(y) = f_\gamma^{(e)}(y)\sigma_{\gamma p\to X}(y) dy \tag{6.24}$$

$$f_\gamma^{(e)}(y) = \frac{\alpha_{em}}{2\pi} \left\{ \frac{1+(1-y)^2}{y} \ln \frac{Q^2_{max}}{Q^2_{min}} - 2\,\frac{1-y}{y} \right\}. \tag{6.25}$$

Appendix B

In this appendix, the selection of the run ranges and the efficiencies needed for the various measurements are collected. All numbers are obtained from MC simulations using the event generators AROMA 2.2 [57] and IJRAY-PYTHIA [62] (IJRAY only generates the photon flux, PYTHIA is the full generator) in combination with the H1 detector simulation. To account for the changing performance of the detector, the simulation is done separately for the three years.

year	accepted	rejected
1994		89935 - 90101
1995	112883 - 112927	
	112965 - 113365	
	115472 - 116766	
	116859 - 117224	
	117599 - 121503	
	121970 - 129459	
	130409 - 131046	
1996		162081 - 162111
		169186 - 169222
		169865 - 169906
		170550

Table 6.1: Selection of run ranges for subtrigger 83.

year	accepted	rejected
1995	116859 - 117224 117601 - 121503 121970 - 131045	
1996		162081 - 162111 169186 - 169222 169865 - 169906 170550

Table 6.2: Selection of run ranges for subtrigger 84.

	direct			resolved
	1994	1995	1996	96
$-1.5 \leq \eta \leq -1.0$	92.3 ± 10.1	80.6 ± 3.5	81.7 ± 2.7	70.8 ± 6.0
$-1.0 \leq \eta \leq -0.5$	96.2 ± 7.8	86.5 ± 2.9	89.2 ± 2.2	81.6 ± 4.6
$-0.5 \leq \eta \leq 0.0$	95.0 ± 8.9	88.2 ± 3.6	89.6 ± 2.8	83.6 ± 3.4
$0.0 \leq \eta \leq 0.5$	100 ± 12.2	87.8 ± 4.9	89.5 ± 3.7	83.3 ± 3.1
$0.5 \leq \eta \leq 1.0$	90.7 ± 14.5	88.5 ± 6.8	91.5 ± 5.4	83.7 ± 2.9
$1.0 \leq \eta \leq 1.5$	90.9 ± 29	90.8 ± 12	91.9 ± 9.1	77.0 ± 2.8
$2.5 \leq p_t$	95.1 ± 4.4	86.0 ± 1.7	87.9 ± 1.3	81.5 ± 1.4
$2.5 \leq p_t \leq 3.5$	94.1 ± 6.3	84.3 ± 8.3	85.1 ± 1.8	79.6 ± 1.7
$3.5 \leq p_t \leq 4.5$	94.0 ± 8.4	87.2 ± 3.4	89.7 ± 8.6	83.9 ± 3.1
$4.5 \leq p_t \leq 6.5$	97.7 ± 10.4	88.5 ± 4.2	91.9 ± 3.2	86.1 ± 4.6
$6.5 \leq p_t \leq 10.5$	100 ± 18.3	88.1 ± 7.8	93.4 ± 6.1	92.0 ± 6.8

Table 6.3: Trigger efficiency for the measurement of the single inclusive cross sections with subtrigger 83 as determined from Monte Carlo simulations for the different years. "Direct" indicates that the events have been generated with AROMA 2.2, "resolved" stands for IJRAY-PYTHIA. Since the resolved contribution is small, it is enough to determine it for the year with most luminosity only. All numbers are given in %.

	Luminosity weighted efficiency		QCD prediction (massive scheme)		resulting trigger efficiency
	direct	resolved	$\frac{direct}{total}$	$\frac{resolved}{total}$	
$-1.5 \leq \eta \leq -1.0$	83.9 ± 5.3	70.8 ± 6.0	99.5	0.5	83.8 ± 5.3
$-1.0 \leq \eta \leq 0.5$	90.4 ± 4.2	81.6 ± 4.6	98.4	1.6	90.3 ± 4.2
$-0.5 \leq \eta \leq 0.0$	90.6 ± 4.9	83.6 ± 3.4	95.5	4.5	90.3 ± 4.8
$0.0 \leq \eta \leq 0.5$	91.6 ± 6.6	83.3 ± 3.1	89.7	10.3	90.7 ± 6.3
$0.5 \leq \eta \leq 1.0$	91.0 ± 8.4	83.7 ± 2.9	79.4	20.6	89.5 ± 7.6
$1.0 \leq \eta \leq 1.5$	91.6 ± 15.9	77.0 ± 2.8	64.7	35.3	86.4 ± 12.9
$2.5 \leq p_t$	89.3 ± 2.4	81.5 ± 1.4	94.1	5.9	88.8 ± 2.3
$2.5 \leq p_t \leq 3.5$	87.0 ± 3.4	79.6 ± 1.7	92.8	7.2	86.4 ± 3.3
$3.5 \leq p_t \leq 4.5$	90.4 ± 4.6	83.9 ± 3.1	94.9	5.1	90.1 ± 4.5
$4.5 \leq p_t \leq 6.5$	92.8 ± 5.7	86.1 ± 4.6	96.7	3.3	92.6 ± 5.6
$6.5 \leq p_t \leq 10.5$	94.3 ± 10.2	92.0 ± 6.8	97.5	2.5	94.3 ± 10

Table 6.4: Trigger efficiency used for the measurement of the single inclusive cross sections with subtrigger 83. The last column is the overall efficiency. All numbers are given in %. The mixture of direct/resolved was obtained from the QCD calculation.

	1995	1996	Luminosity weighted trigger efficiency
	$L = 1.91\ pb^{-1}$	$L = 8.32\ pb^{-1}$	
$-1.5 \leq \eta \leq -1.0$	82.3 ± 12	66.7 ± 27	69.6 ± 25
$-1.0 \leq \eta \leq 0.5$	84.7 ± 3.7	73.5 ± 5.2	75.6 ± 5.0
$-0.5 \leq \eta \leq 0.0$	88.0 ± 3.0	77.1 ± 3.0	79.1 ± 3.0
$0.0 \leq \eta \leq 0.5$	88.5 ± 3.7	75.7 ± 2.5	78.1 ± 2.8
$0.5 \leq \eta \leq 1.0$	85.4 ± 4.9	74.0 ± 2.4	76.1 ± 3.0
$1.0 \leq \eta \leq 1.5$	85.2 ± 8.1	66.3 ± 3.3	69.8 ± 4.6
$2.5 \leq p_t$	86.8 ± 1.7	74.0 ± 1.3	76.4 ± 1.4
$2.5 \leq p_t \leq 3.5$	86.6 ± 2.3	72.3 ± 1.4	75.0 ± 1.6
$3.5 \leq p_t \leq 4.5$	87.6 ± 3.7	75.4 ± 2.9	77.7 ± 3.0
$4.5 \leq p_t \leq 6.5$	85.1 ± 4.9	78.8 ± 4.2	80.0 ± 4.3
$6.5 \leq p_t \leq 10.5$	89.8 ± 9.9	66.3 ± 3.3	70.7 ± 5.2

Table 6.5: Efficiency of subtrigger 84 for the single inclusive cross sections as calculated from a MC sample generated by AROMA 2.2. The results from the two years are weighted with the luminosity to yield the final trigger efficiency (third column). All numbers are given in %. Because of the additional trigger element DCRPh-Tc, the efficiency in 1996 was lower than in 1995.

	direct			resolved
	1994	1995	1996	96
$-1.5 \leq \eta \leq -1.0$	35.5 ± 3.6	35.5 ± 1.4	35.5 ± 1.1	37.9 ± 4.9
$-1.0 \leq \eta \leq -0.5$	57.3 ± 4.6	55.3 ± 1.7	55.6 ± 1.3	61.5 ± 5.3
$-0.5 \leq \eta \leq 0.0$	66.8 ± 6.1	59.8 ± 2.3	59.2 ± 1.8	71.5 ± 5.3
$0.0 \leq \eta \leq 0.5$	64.8 ± 7.8	61.9 ± 3.2	61.1 ± 2.4	66.8 ± 5.3
$0.5 \leq \eta \leq 1.0$	60.8 ± 9.7	63.1 ± 4.5	61.0 ± 3.4	61.1 ± 5.4
$1.0 \leq \eta \leq 1.5$	48.7 ± 16	40.1 ± 5.2	38.6 ± 3.5	45.7 ± 4.6
$2.5 \leq p_t$	53.4 ± 2.5	50.9 ± 0.9	50.7 ± 0.7	58.2 ± 2.0
$2.5 \leq p_t \leq 3.5$	43.3 ± 2.9	42.4 ± 1.1	42.6 ± 0.9	50.8 ± 2.2
$3.5 \leq p_t \leq 4.5$	63.8 ± 5.5	58.8 ± 2.1	57.8 ± 1.6	69.6 ± 4.8
$4.5 \leq p_t \leq 6.5$	72.7 ± 8.0	68.6 ± 4.3	68.7 ± 3.1	71.1 ± 6.5
$6.5 \leq p_t \leq 10.5$	78.2 ± 15	74.3 ± 5.8	69.8 ± 4.2	60.1 ± 13

Table 6.6: D^*-reconstruction efficiencies used for the measurement of the single inclusive cross sections with subtrigger 83 as calculated from MC samples generated by AROMA 2.2 (direct) and IJRAY-PYTHIA (resolved).

	Luminosity weighted efficiency		QCD prediction (massive scheme)		resulting efficiency
	direct	resolved	$\frac{direct}{total}\%$	$\frac{resolved}{total}\%$	
$-1.5 \leq \eta \leq -1.0$	35.5 ± 1.9	37.9 ± 4.9	99.5	0.5	35.5 ± 2.0
$-1.0 \leq \eta \leq 0.5$	55.9 ± 2.5	61.5 ± 5.3	98.4	1.6	56.0 ± 2.6
$-0.5 \leq \eta \leq 0.0$	60.9 ± 3.3	71.5 ± 5.3	95.5	4.5	61.4 ± 3.4
$0.0 \leq \eta \leq 0.5$	62.0 ± 4.2	65.8 ± 5.3	89.7	10.3	62.4 ± 4.4
$0.5 \leq \eta \leq 1.0$	61.2 ± 5.5	61.1 ± 5.4	79.4	20.6	61.2 ± 5.5
$1.0 \leq \eta \leq 1.5$	40.9 ± 8.2	45.7 ± 4.6	64.7	35.3	42.6 ± 7.1
$2.5 \leq p_t$	51.3 ± 1.3	58.2 ± 2.0	94.1	5.9	51.7 ± 1.3
$2.5 \leq p_t \leq 3.5$	42.7 ± 1.6	50.8 ± 2.0	92.8	7.2	43.3 ± 1.6
$3.5 \leq p_t \leq 4.5$	59.2 ± 3.0	69.6 ± 4.8	94.9	5.1	59.7 ± 3.1
$4.5 \leq p_t \leq 6.5$	69.6 ± 4.7	71.1 ± 6.5	96.7	3.3	69.6 ± 4.8
$6.5 \leq p_t \leq 10.5$	72.0 ± 8.3	60.1 ± 13	97.5	2.5	71.7 ± 8.4

Table 6.7: D^*-reconstruction efficiencies used for the single inclusive cross sections with subtrigger 83. The numbers obtained for the different years and direct/resolved are combined according to their weights given by the luminosity and the NLO QCD calculation.

	reconstruction efficiency	trigger efficiency	vertex fit efficiency	total efficiency
$-1.5 \leq \eta \leq -1.0$	35.5 ± 2.0	83.8 ± 5.3	95.6 ± 1.5	28.4 ± 2.4
$-1.0 \leq \eta \leq -0.5$	56.0 ± 2.6	90.3 ± 4.2	95.6 ± 1.5	48.4 ± 3.2
$-0.5 \leq \eta \leq 0.0$	61.4 ± 3.4	90.3 ± 4.2	95.6 ± 1.5	53.0 ± 4.2
$0.0 \leq \eta \leq 0.5$	62.4 ± 4.4	90.7 ± 6.3	95.6 ± 1.5	54.1 ± 5.4
$0.5 \leq \eta \leq 1.0$	61.2 ± 5.5	89.5 ± 7.6	95.6 ± 1.5	52.3 ± 6.5
$1.0 \leq \eta \leq 1.5$	$42.6 \pm 71.$	86.4 ± 13	95.6 ± 1.5	35.2 ± 7.9
$2.5 \leq p_t$	51.7 ± 1.4	88.8 ± 2.3	95.6 ± 1.5	43.9 ± 1.8
$2.5 \leq p_t \leq 3.5$	43.3 ± 1.6	86.4 ± 3.3	95.6 ± 1.5	35.8 ± 2.0
$3.5 \leq p_t \leq 4.5$	59.7 ± 3.1	90.1 ± 4.5	95.6 ± 1.5	51.4 ± 3.8
$4.5 \leq p_t \leq 6.5$	69.6 ± 4.8	92.6 ± 5.6	95.6 ± 1.5	61.6 ± 5.7
$6.5 \leq p_t \leq 10.5$	71.7 ± 8.4	94.3 ± 10	95.6 ± 1.5	64.7 ± 10

Table 6.8: Overview of the different contributions to the total efficiency for the measurement of the single inclusive cross sections with subtrigger 83. The vertex fit efficiency is obtained from data as explained in chapter three.

	1995	1996	Luminosity weighted efficiency
	$L = 1.91\ pb^{-1}$	$L = 8.32\ pb^{-1}$	
$-1.5 \leq \eta \leq -1.0$	26.3 ± 2.4	16.6 ± 4.2	19.8 ± 3.7
$-1.0 \leq \eta \leq -0.5$	44.6 ± 0.9	42.4 ± 2.1	43.1 ± 1.8
$-0.5 \leq \eta \leq 0.0$	51.1 ± 2.1	53.4 ± 1.5	52.7 ± 1.7
$0.0 \leq \eta \leq 0.5$	53.7 ± 1.1	54.9 ± 1.5	54.5 ± 1.4
$0.5 \leq \eta \leq 1.0$	48.3 ± 1.1	49.2 ± 1.4	48.9 ± 1.3
$1.0 \leq \eta \leq 1.5$	30.7 ± 1.5	34.3 ± 1.6	33.2 ± 1.6
$2.0 \leq p_t$	50.2 ± 0.6	50.8 ± 0.7	50.6 ± 0.7
$2.0 \leq p_t \leq 3.0$	38.7 ± 0.4	38.3 ± 1.0	38.4 ± 0.8
$3.0 \leq p_t \leq 4.0$	63.4 ± 0.9	63.9 ± 1.6	63.7 ± 1.4
$4.0 \leq p_t \leq 6.0$	74.5 ± 1.6	75.3 ± 2.1	75.0 ± 2.0
$6.0 \leq p_t \leq 10.0$	72.1 ± 3.0	80.0 ± 5.0	77.5 ± 4.5

Table 6.9: D^*-reconstruction efficiencies used for the measurement of the single inclusive cross sections with subtrigger 84 and the two years 1995 and 1996, as obtained from a MC sample generated by AROMA 2.2.

bin	track reconstruction	trigger	vertex fit	total efficiency
$-1.5 \leq \eta \leq -1.0$	19.8 ± 3.7	69.6 ± 25	95.6 ± 1.5	13.2 ± 5.4
$-1.0 \leq \eta \leq -0.5$	43.1 ± 1.8	75.6 ± 5.0	95.6 ± 1.5	31.1 ± 2.5
$-0.5 \leq \eta \leq 0.0$	52.7 ± 1.7	79.1 ± 3.0	95.6 ± 1.5	39.8 ± 2.1
$0.0 \leq \eta \leq 0.5$	54.5 ± 1.4	78.1 ± 2.8	95.6 ± 1.5	40.7 ± 1.9
$0.5 \leq \eta \leq 1.0$	48.9 ± 1.3	76.1 ± 3.0	95.6 ± 1.5	35.6 ± 1.8
$1.0 \leq \eta \leq 1.5$	33.2 ± 1.6	69.8 ± 4.6	95.6 ± 1.5	22.1 ± 1.8
$2.0 \leq p_t$	50.6 ± 0.7	76.4 ± 3.0	95.6 ± 1.5	37.0 ± 1.0
$2.0 \leq p_t \leq 3.0$	38.4 ± 0.8	75.0 ± 1.4	95.6 ± 1.5	27.6 ± 0.9
$3.0 \leq p_t \leq 4.0$	63.7 ± 1.4	77.7 ± 3.0	95.6 ± 1.5	47.3 ± 2.2
$4.0 \leq p_t \leq 6.0$	75.0 ± 2.0	80.0 ± 4.3	95.6 ± 1.5	57.4 ± 3.5
$6.0 \leq p_t \leq 10.0$	77.5 ± 4.5	70.7 ± 5.2	95.6 ± 1.5	52.4 ± 5.0

Table 6.10: Overview of the different contributions to the total efficiency used for the measurement of the single inclusive cross sections with the subtrigger 84.

		1994	1995	1996	weighted
		$2.308\ pb^{-1}$	$1.043\ pb^{-1}$	$7.317\ pb^{-1}$	efficiency
$0.29 \leq y \leq 0.5$	$-3.2 \leq log(x_g) \leq -2.8$	96.6 ± 19	80.9 ± 8.7	83.2 ± 6.4	85.9 ± 9.8
$0.29 \leq y \leq 0.5$	$-2.8 \leq log(x_g) \leq -2.4$	95.0 ± 7.2	85.5 ± 2.9	87.5 ± 2.2	88.9 ± 3.6
$0.29 \leq y \leq 0.5$	$-2.4 \leq log(x_g) \leq -2.0$	96.7 ± 11	87.2 ± 5.0	90.1 ± 3.7	93.6 ± 5.6
$0.5 \leq y \leq 0.62$	$-3.2 \leq log(x_g) \leq -2.8$	79.5 ± 18	82.0 ± 9.4	82.8 ± 6.6	82.0 ± 9.0
$0.5 \leq y \leq 0.62$	$-2.8 \leq log(x_g) \leq -2.4$	94.4 ± 13	87.5 ± 5.6	87.4 ± 4.3	88.9 ± 6.7
$0.5 \leq y \leq 0.62$	$-2.4 \leq log(x_g) \leq -2.0$	100 ± 21	86.9 ± 10	91.5 ± 8.2	93.6 ± 11.9

Table 6.11: Trigger efficiency used for the measurement of the gluon density with the D^*-method with subtrigger 83 in bins of x_g, determined by using AROMA 2.2.

		1994/1995	1996	Luminosity
		$L = 3.351\ pb^{-1}$	$L = 7.317\ pb^{-1}$	weighted efficiency
$0.29 \leq y \leq 0.5$	$-3.2 \leq log(x_g) \leq -2.8$	38.7 ± 2.3	40.3 ± 2.0	39.8 ± 2.1
$0.29 \leq y \leq 0.5$	$-2.8 \leq log(x_g) \leq -2.4$	50.9 ± 1.8	51.3 ± 1.5	51.2 ± 1.6
$0.29 \leq y \leq 0.5$	$-2.4 \leq log(x_g) \leq -2.0$	60.7 ± 2.8	60.3 ± 2.4	60.4 ± 2.5
$0.5 \leq y \leq 0.62$	$-3.2 \leq log(x_g) \leq -2.8$	41.5 ± 3.4	38.9 ± 2.8	39.7 ± 3.0
$0.5 \leq y \leq 0.62$	$-2.8 \leq log(x_g) \leq -2.4$	52.1 ± 3.2	52.9 ± 3.0	52.6 ± 3.1
$0.5 \leq y \leq 0.62$	$-2.4 \leq log(x_g) \leq -2.0$	68.6 ± 5.8	66.4 ± 5.2	67.0 ± 5.4

Table 6.12: D^*-reconstruction efficiency used for the measurement of the gluon density with the D^*-method with subtrigger 83 in bins of x_g.

		reconstr. efficiency	trigger efficiency	vertex fit efficiency	total efficiency
$0.29 \leq y \leq 0.5$	$-3.2 \leq log(x_g) \leq -2.8$	39.8 ± 2.1	85.9 ± 9.8	95.6 ± 1.5	32.7 ± 4.1
$0.29 \leq y \leq 0.5$	$-2.8 \leq log(x_g) \leq -2.4$	51.2 ± 1.6	88.9 ± 3.5	95.6 ± 1.5	43.5 ± 2.3
$0.29 \leq y \leq 0.5$	$-2.4 \leq log(x_g) \leq -2.0$	60.4 ± 2.5	93.6 ± 5.6	95.6 ± 1.5	54.0 ± 4.0
$0.5 \leq y \leq 0.62$	$-3.2 \leq log(x_g) \leq -2.8$	33.3 ± 3.0	82.0 ± 9.0	95.6 ± 1.5	26.1 ± 4.2
$0.5 \leq y \leq 0.62$	$-2.8 \leq log(x_g) \leq -2.4$	52.6 ± 3.1	88.9 ± 6.7	95.6 ± 1.5	44.7 ± 4.3
$0.5 \leq y \leq 0.62$	$-2.4 \leq log(x_g) \leq -2.0$	67.0 ± 5.4	93.6 ± 12	95.6 ± 1.5	59.9 ± 9.1

Table 6.13: Total efficiency used for the measurement of the gluon density with the D^*-method with subtrigger 83 in bins of x_g (from AROMA 2.2).

	year 1995	year 1996	weighted efficiency
$-2.8 \leq log(x_g) \leq -2.4$	86.0 ± 3.4	82.1 ± 3.6	83.3 ± 3.6
$-2.4 \leq log(x_g) \leq -2.0$	84.1 ± 3.4	75.5 ± 1.8	78.2 ± 2.4
$-2.0 \leq log(x_g) \leq -1.6$	87.4 ± 4.4	65.8 ± 2.6	72.6 ± 3.3
$-1.6 \leq log(x_g) \leq -1.2$	65 ± 13	80 ± 16	75.3 ± 15

Table 6.14: Trigger efficiency used for the measurement of the gluon density with the D^*-method with subtrigger 84 in bins of x_g.

	year 1995	year 1996	weighted efficiency
$-2.8 \leq log(x_g) \leq -2.4$	47.2 ± 2.2	48.7 ± 1.9	48.2 ± 2.0
$-2.4 \leq log(x_g) \leq -2.0$	52.6 ± 2.7	55.1 ± 3.0	54.3 ± 2.9
$-2.0 \leq log(x_g) \leq -1.6$	59.1 ± 5.9	54.1 ± 6.5	55.7 ± 6.3
$-1.6 \leq log(x_g) \leq -1.2$	61 ± 12.2	76 ± 15.2	71.3 ± 14.3

Table 6.15: D^*-reconstruction efficiency used for the measurement of the gluon density with the D^*-method with subtrigger 84 in bins of x_g.

	reconstr. efficiency	trigger efficiency	vertex fit efficiency	total efficiency
$-2.8 \leq log(x_g) \leq -2.4$	48.2 ± 2.0	83.3 ± 3.6	95.6 ± 1.5	38.4 ± 2.4
$-2.4 \leq log(x_g) \leq -2.0$	54.3 ± 2.9	78.2 ± 2.4	95.6 ± 1.5	40.6 ± 2.6
$-2.0 \leq log(x_g) \leq -1.6$	55.7 ± 6.3	72.6 ± 3.3	95.6 ± 1.5	38.7 ± 4.8
$-1.6 \leq log(x_g) \leq -1.2$	61.0 ± 12	75.3 ± 15	95.6 ± 1.5	51.3 ± 15

Table 6.16: Total efficiency used for the measurement of the gluon density with the D^*-method with subtrigger 84 in bins of x_g.

Bibliography

[1] C.F. von Weizsäcker, Z. Phys. **88** (1934) 612; E.J. Williams, Phys. Rev. **45** (1934) 729

[2] S Frixione, M.L. Mangano, P. Nason, G. Ridolfi, Phys. Lett. **B319** (1993) 339

[3] F. Halzen, A. D. Martin, Quarks and Leptons, Wiley 1984

[4] S. Frixione, M.L. Mangano, P. Nason, G. Ridolfi, hep-ph/9702283

[5] D. Amati, R. Petronzio, and G. Veneziano, Nucl. Phys. **B140** (1978) 54;
S. Libby and G. Sterman, Phys. Rev. **D18** (1987) 3252;
A.H. Mueller, Phys. Rev. **D18** (1978) 3705;
R.K. Ellis, H. Georgi, M. Machacek, H.D. Politzer and G.G. Ross, Nucl. Phys. **B152** (1979) 285;
A.V. Efremov and A.V. Radyushkin, Theor. Math. Phys. **44** (1981) 664

[6] J. Collins, D. Soper, G. Sterman, Nucl. Phys. **B263** (1986) 37

[7] R.A. Eichler, Z. Kunszt, Nucl.Phys. **B308** (1988) 791

[8] R.K. Ellis, Z. Kunszt, Nucl. Phys. **B303** (1988) 653

[9] R.K. Ellis, P. Nason, Nucl. Phys. **B312** (1989) 551

[10] J. Smith, W.L. van Neerven, Nucl. Phys. **B374** (1992) 36

[11] Y.L. Dokshitzer, Sov. Phys. JETP **46** (1977) 641

[12] V.N. Gribov, L.N. Lipatov, Sov. J. Nucl. Phys. **15** (1972) 78

[13] G. Altarelli, G. Parisi, Nucl. Phys. **B126** (1977) 641

[14] S. Frixione, M.L. Mangano, P. Nason, G. Ridolfi, Nucl. Phys. **B412** (1994) 225

[15] C. Peterson, D. Schlatter, I. Schmitt, P.M. Zerwas, Phys. Rev. **D27** (1983) 105

[16] Carlo Oleari, private communication

[17] J. Chrin, Z. Phys. **C36** (1987) 163

[18] H1 Collaboration, Nucl. Phys. **B472** (1996) 32

[19] ZEUS Collaboration, Phys. Lett. B. **B401** (1997) 192

[20] M. Cacciari, M. Greco, Nucl. Phys. **B421** (1994) 530

[21] B.A. Kniehl, M. Krämer, G. Kramer, M. Spira, Phys. Lett. **B356** (1995) 539

[22] J. Binnewies, B.A. Kniehl, G. Kramer, Z. Phys. **C76** (1997) 677

[23] M. Cacciari, M. Greco, Phys. Rev. **D55** (1997) 7143

[24] M. Cacciari, M. Greco, Z. Phys. **C69** (1996) 459

[25] M. Cacciari, private communicatio

[26] B. Mele, P. Nason, Nucl. Phys. **B361** (1991) 626

[27] R. Vogt, S.J. Brodsky, P. Hoyer, Nucl. Phys. **B360** (1991) 76

[28] R. Vogt, S.J. Brodsky, Phys. Lett. **B349** (1995) 569

[29] S.J. Brodsky, P. Hoyer, C. Peterson, N. Sakai, Phys. Lett. **93** (1980) 451

[30] R. Vogt, S.J. Brodsky, Nucl. Phys. **B438** (1995) 261

[31] R. Vogt, S.J. Brodsky, Nucl. Phys. **B478** (1996) 311

[32] H1 Collaboration, Z. Phys. **C72** (1996) 593

[33] ALEPH Collaboration, DELPHI Collaboration, L3 Collaboration and OPAL Collaboration, Nucl. Instr. Meth. **A378** (1996) 101

[34] Review of Particle Properties, R.M. Barnett et al., Phys. Rev. **D54** (1996)

[35] H1 Collaboration, Phys. Lett. **B351** (1995) 494

[36] ZEUS Collaboration, Phys. Lett. **B345** (1995) 576

[37] P. Aurenche et al., Phys. Rev. **D39** (1989) 3275;
M. Bonesini et al., WA 70 Collaboration, Z. Phys. **C38** (1988) 371;
G. Alverson et al., E706 Collaboration, Phys. Rev. Lett. **68** (1992) 2584

[38] T. Akesson et al., AFS Collaboration, Soviet J. Nucl. Phys. **51** (1990) 836;
J. Alitti et al, UA2 Collaboration, Phys. Lett. **B299** (1993) 174

[39] CDF collaboration, Phys. Rev. Lett. **73** (1994) 2662

[40] G. Arnison et al., UA1 Collaboration, Phys. Lett. **136B** (1984) 294

[41] CDF collaboration, FERMILAB-CONF-93-203-E, Proc. 16th International Symposium on Lepton and Photon Interactions, Ithaca, NY, 10-15 Aug 1993

[42] A. M. Cooper-Sarkar et al., Z. Phys. **C39** (1988) 281

[43] H. Jung, G.A. Schuler and J. Terron, in "Physics at HERA", Proceedings of the Workshop, DESY, Hamburg, eds. W. Buchmhüller and G. Ingleman, Vol. II, (1991) p. 793
E. Brugnera, ibid., Vol. I, p. 557

[44] H1 Collaboration, Nucl. Phys. **B449** (1995) 3

[45] R. v. Woudenberg et. al., Gluon Density Determination from Open Charm Events at HERA, Proceedings of the DESY Workshop "Physics at HERA", Hamburg, 1991

[46] Daniel D. Pitzl, Abschirmung der HERA-Detektoren gegen Synchrotronstrahlung, Diploma Thesis, II. Institute for Experimental Physics, University of Hamburg, 1987

[47] Rainer Wallny, Untersuchung des strahlinduzierten Untergrundes bei der Datennahme von Ereignissen der tief-inelastischen Streuung durch den H1-Detektor bei HERA, Diploma Thesis, University of Heidelberg, 1996

[48] H1 Collaboration, Nucl. Instr. Meth. **A386** (1997) 310, 348

[49] H1 Collaboration, Luminosity Measurement in the H1 Experiment at HERA, Proceedings o the 28th International Conference on High Energy Physics ICHEP'96, Warsaw, Poland, July 1996

[50] H1 Collaboration, Z. Phys. C66 (1995) 529

[51] H. Drumm et al., Nucl. Instr. and Meth. 176 (1980) 333

[52] Th. Wolff et al., Nucl. Instr. and Meth. A323 (1992) 537-541

[53] H. Beck, Principles and Operation of the z-Vertex Trigger, H1 note 06/96-479

[54] M. Biddulph, Scale Dependence of the Charm Production Cross Section in Photoproduction and Performance of the Central Silicon Tracker at the H1 Experiment, Ph. D. Thesis, ETH Zurich (1997), No. 12331

[55] G. Feldmann et al., Phys. Rev. Lett. **38** (1977) 1313

[56] H1 Collaboration, Z. Phys. **C69** (1995) 27

[57] G. Ingelman, J. Rathsman, G. A. Schuler, Comput. Phys. Commun. **101** (1997) 135

[58] W. Erdmann, Untersuchung der Photoproduktion von D^*-Mesonen am *ep*-Speicherring HERA, Ph. D. Thesis, ETH Zürich (1996), No. 11441

[59] G. Zech, DESY 95-113

[60] A.D. Martin, R.G. Roberts, W.J. Stirling, Phys. Rev. **D51** (1995) 4756

[61] M. Glück, E. Reya, A. Vogt, Phys. Rev. **D45** (1992) 3986

[62] T. Sjöstrand, Comput. Phys. Commun. **82** (1994) 74

[63] H1 Collaboration, Z. Phys. **C69** (1995) 27

[64] V. Andreev, Acceptance Determination of the Electron Tagger (ET44) in 1995, H1 note 10/96-493

[65] Urs Langenegger, private communication

[66] A. Gellrich, Nachweis von Mesonen mit Charm in der Elektron-Proton-Streuung mit dem H1 Detektor, Ph. D. Thesis, University of Hamburg (1994)

[67] A.D. Martin, R. G. Roberts, W. J. Stirling, Phys. Lett. **B354** (1995) 155

[68] A. Levy, H. Abramowicz, K. Charchula, Phys. Lett. **B269** (1991) 458

[69] B. Anderson, G. Gustafson, B. Söderberg, Z. Phys. **C20** 317 (1983)

[70] N. Tobien, Das Ansprechverhalten des H1-Flüssigargon-Kalorimeters auf niederenergetische Hadronen, Diploma Thesis, University of Hamburg (1996)

[71] G. D'Agostini, Nucl. Instr. and Meth. **A362** (1995) 487

[72] ARGUS Collaboration, H. Albrecht et. al., Z. Phys. **C52** (1991) 353

Acknowledgements

I would like to express my gratitude to Ralph A. Eichler who was a true "Doktorvater" to me. Being teacher and friend, he was a constant source of valuable advice beyond the daily odds and ends and guided me with wisdom through my graduate studies.

Prof. Zoltan Kunszt deserves thanks for many helpful lunch-time discussions and for readily accepting to be co-examiner.

I would like to sincerely thank the members of the CST group: Roland Horisberger, who not only introduced me to the field of silicon detectors and it's miracles and foot-traps, but also was a amicable special adviser for the most difficult problems - in physics and far beyond. Daniel Pitzl, who was my teacher for whatever one can think of - from electronics and jet physics to the german cuisine. His optimism kept me going on whenever a friday 13th came along. And finally Kurt Gabathuler, Silvan Streuli, Wolfram Erdmann, Monika Biddulph, Johannes Gassner and Moritz Lechner. It was a great pleasure to work with you.

A sincere "thank you" goes to Christoph Grab, who put up with me as a room mate in the last year of my postgraduate education. His friendly support in software and computing and his excellent knowledge of physics have been an invaluable help in doing this work. Also Stefano Passaggio deserves thanks for many very interesting discussions, sometimes til late in the night.

Special thanks goes to Urs Langenegger, Yorgos Tsipolitis, Martin zur Nedden and David Müller for giving me advice on track triggers and more. For instructive discussions on QCD I would like to thank Gudrun Heinrich and especially Stefano Frixione. Besides that, I thank Urs and Gudrun for the great time we had "on the rocks".

Apart from those engaged in H1 and physics in general I would like to sincerely thank my beloved wife Brigitte and my parents for their patience and moral support.

Curriculum Vitae

Name	Hubert Niggli
Born	June 30th 1968, in Luzern
Citizenship	Horw (LU), Switzerland

Education

1981-1988	High school, Kantonsschule Alpenquai, Luzern
1988	Matura, type C
1988	Military services
1989-1994	Study of physics at the Swiss Federal Insitute of Technology (ETH) in Zurich
1994	Diploma in physics at the ETH-Zurich. Title of thesis: "Charge Collection in Double Sided Silicon Detectors for H1"
nov 1994- mar 1998	Graduate education in experimental particle physics at ETH